Development of Photocatalysts and Dual Cocatalysts for Selective Carbon Dioxide Conversion Using Water as the Reductant

Shuying Wang

2021

Preface

The industrial revolution prompted the rapid development of technology and medicine, growth of global population, and increase in energy consumption worldwide. The amount of CO_2, which is the primary greenhouse gas (GHG), has increased significantly over the past decades, which negatively impacted global climate change and led to an increase in number of natural disasters worldwide. The atmospheric concentration of CO_2 increased from an estimated level of 280 ppm before the industrial revolution to 380 ppm. The Intergovernmental Panel on Climate Change reported that the global temperature increased by 0.6 °C during the last century and predicted that it would increase by 1.4-5.8 °C before the end of this century. The world needs to establish sustainable development goals; therefore, it is critical that the human race explores ways to rapidly lower carbon energy demands to meet the goals of the Paris Agreement. Sunlight energy is eco-friendly, continuous, and abundant. Several approaches, such as thermocatalysis, electrocatalysis, photoelectrocatalysis, and photocatalysis, have been explored for reducing CO_2 to chemicals such as CO, CH_3OH, CH_4, and other low molecular-weight alkanes and olefins. The conversion of CO_2 into chemicals would form a closed loop between released CO_2 and fossil fuel. Sunlight-driven photocatalytic conversion of CO_2 into chemicals is a revolutionary approach for decreasing GHG concentration and decrease fossil energy consumption to achieve a zero net growth.

This thesis focuses on the design and development of efficient and highly selective heterogeneous catalysts for photocatalytic conversion of CO_2 into CO using H_2O under sunlight irradiation, with a particular emphasis on the effects of surface modification, metal cation doping, and dual cocatalysts on the photocatalytic CO_2 reduction reaction. It was determined that upon Ag modification, Al-doped perovskite strontium titanite (Al-$SrTiO_3$) with numerous surface stepwise edges exhibited an excellent photocatalytic performance for CO_2 conversion using H_2O as the electron donor under photoirradiation at wavelengths higher than 300 nm. Moreover, it was demonstrated that upon loading a Ag-Co dual cocatalyst on the surface of Al-$SrTiO_3$, CO formation rate was markedly improved and CO evolution selectivity reached 99.7%. Ag was present on the {100} facets of the Ag-Co dual cocatalyst-loaded Al-$SrTiO_3$ and facilitated CO_2 reduction, whereas Co species were located on the {110} facets and facilitated H_2O oxidation. Al-$SrTiO_3$ anisotropy was much stronger than that of pristine $SrTiO_3$. In addition, it was demonstrated that the Zn species-modified Ag-loaded $ZnTa_2O_6$ exhibited higher selectivity of CO evolution than the Ag-loaded $ZnTa_2O_6$ photocatalyst.

The experiments described in this thesis were performed at the Department of Molecular Engineering, Graduate School of Engineering, Kyoto University, Japan, between 2018 and 2021 under the supervision of Professor Tsunehiro Tanaka and Associate Professor Kentaro Teramura. The author would like to express her sincere thanks to Professor Tsunehiro Tanaka for his constructive suggestions, fruitful discussions, valuable guidance, and care throughout the whole study. The author would also like to extend her deepest thanks to Associate Professor Kentaro Teramura for the informative discussions, his insightful comments, and patient instruction. The author expresses her gratitude goes to Associate Professor Saburo Hosokawa for his useful advice, accurate comments, and kind guidance. The author is deeply indebted to Dr. Hiroyuki Asakura for his astute suggestions, kind guidance, and helpful discussion. Sincere appreciation to Professor Kazunari Domen and Associate Professor Takashi Hisatomi at the Shinshu University for their valuable suggestions and kind guidance regarding cocatalyst-loaded Al-$SrTiO_3$ topic. Cordial thanks are extended to Professor Hisao Yoshida at the Kyoto University for his useful advice and kind help with some of the experiments described herein. Her deepest appreciation goes to Associate Professor Zeai Huang at the Southwest Petroleum University, Assistant Professor Kosuke Beppu at the Ryukoku University, Postdoctoral Researcher Rui Pang at the National Institute of Advanced Industrial Science and Technology (AIST), Assistant Professor Soichi Kikkawa at the Tokyo Meteropolitan University, and Dr. Kazuki Tamai for their considerate help, instructive suggestions, and effective discussions during our time together at Professor Tsunehiro Tanaka’s laboratory. Many thanks to Mr. Xu Xuanwen for his help and discussions regarding this study. The author would also like to acknowledge the following Master’s students: Ms. Sumika Yoshizawa, Mr. Shotaro Kidera, Mr. Yuto Nakatani, Mr. Yudai Oshino, Mr. Masaatsu Ishida, Mr. Kenya Onishi, Mr. Hiroyuki Tanaka, Ms. Maho Kirihara, Mr. Chikara Watanabe, Mr. Masashige Morishita, Mr. Rinsuke Suzuki, Mr. Takahiro Endo, Ms. Kyoto Fujita, Mr. Ryosuke Yamada, and Mr. Xueshi Liu, who helped her with various measurements and experiments and guided her steps after her relocation to Kyoto. Special thanks go to Secretary Ms. Yoko Yoshitake and Secretary Ms. Mami Nisho for their kind help with official affairs. The author is also extremely grateful to the staff and researchers at Professor Tsunehiro Tanaka’s laboratory for their friendship.

Lastly, the author would like to express her most sincere gratefulness to her family, particularly her parents and husband, for their understanding, support, and encouragement and to the State Scholarship of China Scholarship Council for the funding provided during her doctoral studies.

Shuying Wang

Kyoto
February 2021

CONTENTS

General introduction

Fundamentals of CO_2 photoreduction over heterogenous photocatalysts

Converting solar energy into chemical energy is an important method for achieving and promoting global sustainable development goals. Artificial photosynthesis, which is inspired by plants, can easily convert sunlight energy, CO_2, and H_2O into chemical energy, such as CO, hydrocarbons, and O_2 over semiconductor photocatalysts. Sunlight-driven photocatalytic reduction of CO_2 and H_2O to chemicals and O_2 over heterogenous photocatalyst has become a research hotspot since the pioneering studies of Fujishima and Honda, [1] Hamann, [2] and Inoue et al. [3] in the 1970s. Photocatalytic conversion of CO_2 into chemicals over heterogenous photocatalysts under light irradiation typically consists of four steps: (1) photon harvesting, (2) photoexcited electron–hole generation, (3) charge transfer to the heterogenous photocatalyst surface, and (4) surface catalytic reaction. [4-7] When photon energy (hv) is greater than or equal to the photocatalyst bandgap (Eg), upon photocatalyst excitation, electrons move from the valence band (VB) to the conduction band (CB) of the photocatalyst and holes form in the VB. Moreover, photoexcited electrons ($\boldsymbol{e}^-$) and holes ($\boldsymbol{h}^+$) are generated in single photocatalyst particles. When a semiconductor photocatalyst is continuously irradiated, the generated photoexcited electrons are transferred to the photocatalyst surface where they reduce CO_2 to hydrocarbons, whereas the holes promote H_2O oxidation at the photocatalyst surface. [8-9]

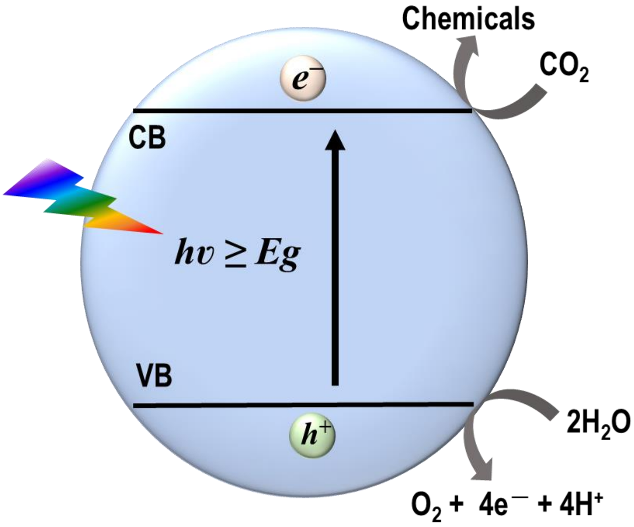

Figure 1. Schematic diagram of photocatalysis over semiconductor photocatalysts. Here, ***e***$^{-}$, ***h***$^{+}$, VB, CB, *hv* and *Eg* denote photogenerated electron, photogenerated hole, valence band, conduction band, photon energy, and photocatalyst bandgap, respectively.

In addition, CO_2, which is a linear molecule, is one of the most thermodynamically stable carbon compounds. During photocatalytic CO_2 reduction, a high energy input is required to break the C=O bonds and form C–H bonds. The possible reactions on the surface of heterogenous photocatalysts during the photoirradiation-driven photocatalytic conversion of CO_2 into chemicals in aqueous solution and their potentials are summarized in Table 1.

Table 1. Possible reactions during photocatalytic CO_2 reduction and potentials (E^o) vs. the normal hydrogen electrode (NHE) at pH 7 required to produce CO, HCOOH, CO, HCHO, CH_3OH, CH_4, CH_3COOH, and CH_3CHO. [10-13]

Reaction	**$E^{o\prime}$ (V vs. NHE) at pH 7.0**	**Equation**
Photocatalyst + hν → e^{-} + h^{+}		(1)
$H_2O + h^{+} \rightarrow OH\cdot + H^{+}$	2.32	(2)
$H_2O + 4h^{+} \rightarrow 4H^{+} + O_2$	0.82	(3)
$CO_2 + e^{-} \rightarrow CO_2^{-}$	−1.90	(4)
$CO_2 + 2H^{+} + 2e^{-} \rightarrow CO + H_2O$	−0.51	(5)
$CO_2 + 2H^{+} + 2e^{-} \rightarrow HCOOH$	−0.61	(6)

$CO_2 + 4H^+ + 4e^- \rightarrow HCHO + H_2O$	−0.48	(7)
$CO_2 + 6H^+ + 6e^- \rightarrow CH_3OH + H_2O$	−0.38	(8)
$CO_2 + 8H^+ + 8e^- \rightarrow CH_4 + 2H_2O$	−0.24	(9)
$CO_2 + 8H^+ + 8e^- \rightarrow CH_3COOH + 2H_2O$	−0.31	(10)
$CO_2 + 10H^+ + 10e^- \rightarrow CH_3CHO + 3H_2O$	−0.36	(11)
$2H^+ + 2e^- \rightarrow H_2$	−0.41	(12)

The potential of the H_2 evolution reaction (Eq. (12)) was higher than those of the two-electron HCOOH and CO formation reactions (Eqs. (5) and (6)), which indicated that the H^+/H_2 reduction reaction was favored over the CO_2 reduction reaction in the presence of H_2O. Therefore, to increase CO_2 evolution selectivity, H_2 evolution should be suppressed. Chemical formation selectivity ($\boldsymbol{S}$ (%)) and the number of consumed electrons and holes ($\boldsymbol{e^-/h^+}$) for the photocatalytic conversion of CO_2 into chemicals using H_2O as the electron donor in aqueous solution can be calculated as follows: [14]

$$\boldsymbol{S}\,(\%) = (2\boldsymbol{R}_{CO} + 2\boldsymbol{R}_{HCOOH} + 4\boldsymbol{R}_{HCHO} + 6\boldsymbol{R}_{CH3OH} + 8\boldsymbol{R}_{CH4} + 8\boldsymbol{R}_{CH3COOH} + 2\boldsymbol{R}_{CH3CHO})/(2\boldsymbol{R}_{CO} + 2\boldsymbol{R}_{HCOOH} + 4\boldsymbol{R}_{HCHO} + 6\boldsymbol{R}_{CH3OH} + 8\boldsymbol{R}_{CH4} + 8\boldsymbol{R}_{CH3COOH} + 2\boldsymbol{R}_{CH3CHO} + 2\boldsymbol{R}_{H2}) \times 100 \qquad (13)$$

and

$$\boldsymbol{e^-/h^+} = (2\boldsymbol{R}_{CO} + 2\boldsymbol{R}_{HCOOH} + 4\boldsymbol{R}_{HCHO} + 6\boldsymbol{R}_{CH3OH} + 8\boldsymbol{R}_{CH4} + 8\boldsymbol{R}_{CH3COOH} + 2\boldsymbol{R}_{CH3CHO} + 2\boldsymbol{R}_{H2})/4\boldsymbol{R}_{O2}, \qquad (14)$$

where $\boldsymbol{R_x}$ is the formation rate of photocatalytic product $\boldsymbol{x}$. When H_2O serves as the electron donor, $\boldsymbol{e^-/h^+}$ should equal 1.

Heterogenous photocatalyst design

In 1970s, Inoue et. al [3] reported the photocatalytic reduction of CO_2 to chemical compounds, such as CO, CH_4, CH_3OH, and HCOOH, over several semiconductor photocatalysts suspended in CO_2 saturated aqueous solutions illuminated by a Xe lamp for the first time. Thereafter, many semiconductors were used as CO_2 reduction photocatalysts. [15-36] Kudo et al. [15] reported that Ag-cocatalyst-modified perovskite-structured $BaLa_4Ti_4O_{15}$ presented good activity for the photoreduction of CO_2 to CO in aqueous solution in the absence of sacrificial reagents. Subsequently, several Ag-cocatalyst-modified semiconductors, such as $La_2Ti_2O_7$,[16] SrO/Ta_2O_5,[17] $KCaSrTa_5O_{15}$,[18] $ZnGa_2O_4$,[19] $ZnTa_2O_6$,[20] $Sr_2KTa_5O_{15}$,[21] $ZnGa_2O_4$/G_2O_3,[22-23] $CaTiO_3$,[24] $SrNb_2O_6$,[25] $Sr_{1.6}K_{0.37}Na_{1.43}Ta_5O_{15}$,[26] Yb–Zn/$Ga_2O_3$,[27] Mg–Al/$Ga_2O_3$,[28] Pr/$Ga_2O_3$,[29] $NaTaO_3$:Ba,[30] $K_2YTa_5O_{15}$,[31] and $Na_2Ti_6O_{13}$,[33] have been reported as active heterogenous photocatalysts for photocatalytic CO_2 reduction using H_2O as the electron donor. The CO formation rates and CO evolution selectivities over various heterogenous photocatalyst in $NaHCO_3$ aqueous solution under ultraviolet (UV) light irradiation provided by a 400 W high-pressure Hg lamp using H_2O as the electron donor reported during the past decade are illustrated in Figure 2. The CO formation rates in Figure 2 indicate that the photocatalytic activity for CO_2 reduction and CO evolution selectivity were significantly improved over the last decade.

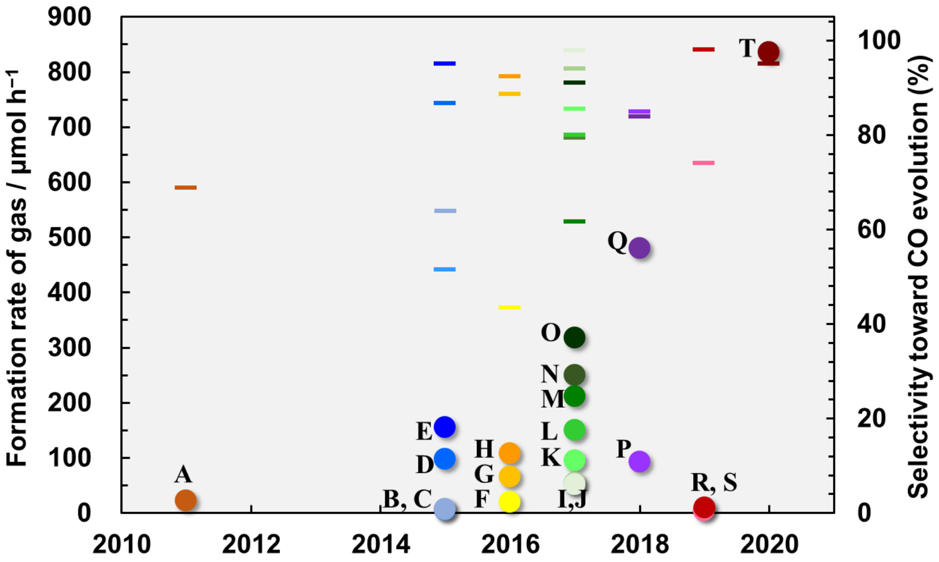

Figure 2. CO formation rates and CO evolution selectivities over several heterogenous photocatalysts in a $NaHCO_3$ aqueous solution under UV light irradiation provided by a 400 W high-pressure Hg lamp ($\lambda > 254$ nm) using H_2O as the electron donor over the last decade. **A.** Ag/$BaLa_4Ti_4O_{15}$,[15] **B.** Ag/$La_2Ti_2O_7$,[16] **C.** Ag/SrO/Ta_2O_5,[17] **D.** Ag/$KCaSrTa_5O_{15}$,[18] **E.** Ag/$ZnGa_2O_4$,[19] **F.** Ag/$ZnTa_2O_6$,[20] **G.** Ag/$Sr_2KTa_5O_{15}$,[21] **H.** Ag/$ZnGa_2O_4$/G_2O_3,[22-23] **I.** Ag/$CaTiO_3$,[24] **J.** Ag/$SrNb_2O_6$,[25] **K.** Ag/$Sr_{1.6}K_{0.37}Na_{1.43}Ta_5O_{15}$,[26] **L.** Ag/Yb–Zn/$Ga_2O_3$,[27] **M.** Ag/Mg–Al/$Ga_2O_3$,[28] **N.** Ag/Pr/$Ga_2O_3$,[29] **O.** Ag/$NaTaO_3$:Ba,[30] **P.** A/ $K_2YTa_5O_{15}$,[31] **Q.** Ag–Cr/Ga_2O_3,[32] **R.** Ag/$Na_2Ti_6O_{13}$,[33] **S.** Ag–Mn/$K_2Ti_6O_{13}$,[34] and **T.** Ag–Cr/CaO/$CaGa_4O_7$/Ga_2O_3.[35]

Strategies for improving photocatalytic CO_2 reduction performance

The photocatalytic CO_2 reduction reaction occurs on the surface of photocatalysts in CO_2-saturated aqueous solutions; therefore, photocatalysis is a surface/interface process. [7] The physical and chemical properties of semiconductors are extremely important for their photocatalytic CO_2 reduction performance. It was considered that the surface of heterogeneous photocatalysts provided catalytic sites for CO_2 adsorption and facilitated the transfer of photoexcited electron–hole pairs from the surface of single photocatalyst particles to CO_2 species for reaction. Therefore, engineering the band structure, morphology, and microstructure, crystal facet exposure, and cocatalyst utilization accelerated the development of efficient CO_2 reduction photocatalysts. Several factors, such as surface modification, crystal facet exposure, and cocatalyst loading, are discussed in this thesis.

Band structure

Photocatalyst Eg is a critical factor that determines the wavelength of light adsorbed by photocatalysts (λ). Holes and electrons are photogenerated in semiconductors when photon energy (hv) is higher than or equal to the Eg of the semiconductor, that is:

$$Eg \leq hv = hc/\lambda, \tag{15}$$

where h is the Planck constant, and c is the speed of the light. In addition, Eg, which is the energy between the VB and CB of photocatalysts, affects the activation energy required for electrons to transition to the available delocalized unoccupied orbitals. The ability of a semiconductor to serve as a CO_2 reduction catalyst depends on the positions of its VB and CB. Specifically, the CB potential should be more negative than the CO_2 reduction potential and the VB potential should be higher than the H_2O oxidation potential (Table 1). In addition, the solar spectrum consists of 95% visible light (400-700 nm) and near-infrared (700-2500 nm) and only 5% UV light (300-400 nm). [37] Therefore, the Eg values of sunlight-driven photocatalysts should be lower than 3.1 eV.

Doping is commonly used to modify the band structure of photocatalysts. Dopants can reduce the Eg of photocatalysts, improve their light absorption, and facilitate free electrons generation. [38-41] For example, CO_2 temperature programmed desorption (TPD) and electrochemical experiments revealed that upon Co doping, the electron density around the O^{2-} anions of $BiVO_4$ increased, which enhanced CO_2 activation and electron transfer to CO_2 molecules. [38] Density functional theory (DFT) calculations suggested that the doped Co 3d orbitals were located at the top of the VB and served as active centers for H_2O oxidation. [38] Because of the high energy of the 4d and 5d orbitals, transition element dopants can enhance electron mobility without altering the minimum CB of host semiconductors. [39, 42-44] Iwashima and Kudo [45] and Ma et al. [44] reported that the energy levels of cation dopants, such as Rh^{3+}, were located between the VB and CB of $SrTiO_3$ photocatalyst. In addition, Kikkawa et al. [39] utilized Rh-doped Ga_2O_3 (Rh/Ga_2O_3) prepared via coprecipitation as CO_2 photoreduction catalyst using H_2O as the electron donor. The absorption edge of Ga_2O_3 shifted from 270 to 370 nm after Rh doping, and the Ga_2O_3:Rh photocatalyst presented a new broad absorption band in the range of 400-500 nm. Ag−Cr-loaded Rh/Ga_2O_3 facilitated the photoreduction of CO_2 to CO under photoirradiation at $\lambda \geq 300$ nm. [39]

Surface modification

Surface basic sites

The condition of the photocatalyst surface affects CO_2 and H_2O adsorption during photocatalytic reactions. Solid basic materials, such as alkali and alkaline-earth metals, play important roles in the surface capture of CO_2 molecules because CO_2 is a Lewis acid that can easily form bonds with Lewis basic sites. In addition, adsorbed CO_2 species, such as carbonates and bicarbonates, contain bent bonds unlike the linear CO_2 molecule. [46] Photocatalysts modified with basic species, such as alkali and alkaline-earth metals, presented good photocatalytic activity for CO_2 reduction using H_2O as the reductant. [17, 47] In addition, Iguchi et al. [28] reported that Mg–Al layered double hydroxide (LDH)-modified Ag/Ga_2O_3 outperformed Ag/Ga_2O_3 in terms of CO_2 reduction photoactivity and CO evolution selectivity. Mg–Al LDH can be used as a CO_2 adsorbent because it presents solid basic sites and a large specific surface area. [28, 48] Bernal et al. [49] reported that rare earth (RE) sesquioxides can react with CO_2 and H_2O to form carbonate species. Sakata et al. [50] used Ga_2O_3 for photocatalytic H_2O splitting under light irradiation; however, the CO_2 reduction selectivity of Ga_2O_3 was lower than its H_2O splitting selectivity. [23, 29] Huang et al. [27] and Tatsumi et al. [29] designed highly effective and selective photocatalysts for the photocatalytic conversion of CO_2 into CO using

H_2O as the electron donor via RE material modification. The prepared RE-modified Ga_2O_3 catalysts, namely Pr/Ga_2O_3 [29] and Yb–Zn/Ga_2O_3, [27] presented higher efficiency for the photocatalytic conversion of CO_2 into CO using H_2O as the electron donor and higher CO evolution sensitivity than Ga_2O_3.

Additionally, Zn modification of Ag-loaded Ga_2O_3 enhanced the photocatalytic conversion of CO_2 to CO using H_2O as the reductant and increased CO evolution selectivity from 26.4% to 87.4%. [23] Moreover, generating a $ZnGa_2O_4$ layer on the surface of Ga_2O_3 photocatalyst successfully suppressed H_2 gas formation. [19, 22]

Surface defects

Surface defects, such as oxygen vacancies (V_Os) and step edges, are the most reactive sites on the surface of metal oxides and play an important role in modifying the physical and chemical properties of semiconductors. [6, 51-53] Such defects could be created on the surface of semiconductors via anion or cation ions doping or using thermal treatments. V_Os can adsorb and activate CO_2 molecules on the surface of photocatalysts. [54-55] Lee et al. [54] studied the adsorption of CO_2 molecules at the V_Os on the TiO_2 (110) surface using scanning tunneling microscopy (STM) and reported that most V_O sites were occupied by CO_2 molecules. The surface V_O and O atoms of CO_2 molecules lowered the activation barrier and enhanced CO_2 trapping and activation. [54] In addition, Ye et al. [56] analyzed a self-doped $SrTiO_{3-\delta}$ catalyst prepared using heat treatments in an Ar atmosphere in the temperature range of 1200-1400 °C. Pulsed CO_2 adsorption and TPD experiments revealed that the chemical adsorption of CO_2 on $SrTiO_{3-\delta}$ was enhanced by increasing the number of V_Os on the $SrTiO_{3-\delta}$ surface. [56] Moreover, the optimum Vo concentration in $SrTiO_3$ was reported to enhance the photocatalytic performance of $SrTiO_3$ by improving the charge separation of photogenerated charge carriers. [57] Wang et al. [55] introduced Cu into CeO_{2-x} to generate and stabilize V_Os and promote the photocatalytic activity of CeO_{2-x}. In situ Fourier-transform infrared (FT-IR) spectroscopy revealed the presence of different CO_2^- species on the surface of Cu/CeO_{2-x}, and the intensities of the signals of adsorbed CO_2 species, such as CO_2^-, HCO_3^-, b-CO_3^{2-}, and m-CO_3^{2-}, in the FT-IR spectrum of Cu/CeO_{2-x} were stronger than those in the FT-IR spectrum of CeO_{2-x}. This was attributed to the presence of Cu and V_Os in Cu/CeO_{2-x}, which provided many active sites for CO_2 adsorption/activation and altered the adsorption/activation modes of CO_2. [55]

Geometrical facet modification

The electronic band structure, surface energy, surface active sites, reactant adsorption, and product desorption depend on the crystal facets of the catalyst. Crystal facet modification significantly affects the physical and chemical properties of crystals. [13, 58-65] For example, {101} facet exposure enhanced the adsorption capacity of TiO_2 photocatalysts for CO_2. [13] Typically, the {101} rather than the {001} facet of anatase TiO_2 is exposed because the thermodynamic stability of the {101} facet is higher than that of the {001} facet, [59] which boosts the adsorption capacity of TiO_2 for CO_2. DFT calculations regarding CO_2 adsorption on TiO_2 clusters indicated the formation of different adsorbed species depending on crystal facet structure. [66] The interactions of CO_2 on the {010} facets of TiO_2 clusters was predicted to be stronger than those on the {101} and {001} facets. [66] In addition, Ye et al. [62] reported that the photocatalytic reduction of CO_2 to CH_4 using H_2O vapor was favored on the {010} facet of TiO_2, which presented better CO_2^-, m-CO_3^{2-}, and HCO_3^- adsorption properties than the {101} and {001} facets of anatase TiO_2. Moreover, Yu et al. [58] proposed that the {101} and {001} facets of anatase TiO_2 presented different band structures and band edge positions, which resulted in the formation of a facet-based homojunction inside TiO_2 and facilitated the transfer of photogenerated electrons and holes to different facets. The ratio of exposed {101} and {001} facets greatly affected the photocatalytic activity of anatase TiO_2 for the reduction of CO_2 to CH_4, and the highest CH_4 yield was obtained at the exposed {101}-to-exposed {001} facet ratio of 45:55. Additionally, Liu et al. [60] analyzed 1D ternary nanostructured Zn_2GeO_4 and reported that the ultralong (hundreds of micrometers) and ultrathin (~7 nm) geometry of Zn_2GeO_4 nanoribbons greatly promoted photocatalytic activity toward CO_2 reduction to renewable hydrocarbon fuel (CH_4) using H_2O vapor. The geometric and electronic structures of Zn_2GeO_4, namely (1) the high specific surface area, (2) excellent crystal quality for charge separation, (3) ultralong longitudinal dimension for charge transport channels, and (4) ultrathin nanoribbons, which facilitated the quick transfer of charges to the surface, led to the good photocatalytic activity of Zn_2GeO_4 for CO_2 reduction. [60, 67-68] Furthermore, Liu et al. [61] reported that the photocatalytic conversion of CO_2 to CH_4 over ultrathin $ZnGa_2O_4$ nanosheets with 99.6% of {110} facets exposed was ~35% higher than that over meso-$ZnGa_2O_4$ because of the high specific surface area and strong CO_2 adsorption ability of ultrathin $ZnGa_2O_4$.

Cocatalyst modification methods

Most semiconductor photocatalysts cannot achieve a good photocatalytic activity and CO_2 reduction selectivity in aqueous solutions in the absence of cocatalysts because of the high recombination rate of photogenerated electrons and holes and low surface reaction efficiency. Therefore, several types of metal cocatalysts have been added to the surface of semiconductor photocatalysts to enhance their photocatalytic performance for CO_2 reduction. The cocatalysts promoted charge separation and transfer, and provided effective reaction sites on the surface of semiconductor photocatalysts.

Single cocatalyst loading

Many types of materials, such as noble metals (e.g., Au, [15] Pt, [47, 69] and Pd [70]), non-noble metals (e.g., Cu [69, 71]), and metal oxides (e.g., Cu_2O, [10] MgO, [47] and NiO [72]), have been studied as cocatalysts for the photocatalytic conversion of CO_2 into chemicals, such as CO and CH_4. Ag nanoparticles have been added to photocatalyst surfaces since 2011 and have improved the formation rate of photocatalytic products, such as CO, from CO_2 under photoirradiation. [15] Loading Ag cocatalyst on the surface of $BaLa_4Ti_4O_{15}$ [15] and $NaTaO_3$-based photocatalysts [30] increased efficiency and CO_2 reduction selectivity more than other cocatalysts, such as NiO_x, Ru, Cu, Au, Rh, and Pd, in aqueous solution using H_2O as the reductant under photoirradiation. Moreover, the photocatalytic conversion of CO_2 into CO using H_2O as the electron donor over photocatalysts such as $ZnGa_2O_6$, [19] La_2TiO_7, [16] $Sr_2KTa_5O_{15}$, [21] $ZnTa_2O_6$, [20] $Sr_2ReKTa_5O_{15}$, [31] $ZnGa_2O_6/Ga_2O_3$, [22] Mg–Al/Ga_2O_3, [28] $SrNb_2O_6$,[24, 73] and Rh–Ga_2O_3 [39] was improved via Ag cocatalyst modification.

Dual cocatalysts loading

Single cocatalysts loaded on the surface of semiconductor photocatalysts play an important role during the photocatalytic conversion of CO_2 into chemicals. To further enhance the performance of photocatalysts, loading dual cocatalysts, such as Pt–Cu, [69] Pt–MgO, [47] Au–Cu, [74-75] Ni@NiO, [76] Pt@Cu_2O, [77] Ag–Cr, [32] and CuO_x–CoO_x [78] on the surface of photocatalysts was used to address the shortcomings of single cocatalyst-loaded photocatalysts, including improving CO_2 chemisorption, [47] suppressing the backward reaction, [32] and enhancing photoinduced hole consumption. [34, 79] Wang et al. [47] reported that the presence of an amorphous layer of MgO cocatalyst on the surface of Pt–TiO_2 photocatalyst led to suppressing the H_2 formation rate and increasing selectivity toward CH_4 for the CO_2 reduction reaction because of increasing CO_2 chemisorption and electron density. Pang et al. [32, 80-81] reported that core–shell Ag–Cr dual cocatalyst-loaded Ga_2O_3 photocatalyst (Ag@Cr/Ga_2O_3) presented higher CO formation rate and CO evolution selectivity than Ga_2O_3 (Figure 3). It was proposed that the $Cr(OH)_3 \cdot xH_2O$ shell on the surface of the Ag cocatalyst could greatly suppress the backward CO_2 photocatalytic reduction reaction; [32] moreover, the thickness of the $Cr(OH)_3 \cdot xH_2O$ shell effectively boosted the activity of Ag@Cr/Ga_2O_3 for CO_2 reduction. [80]

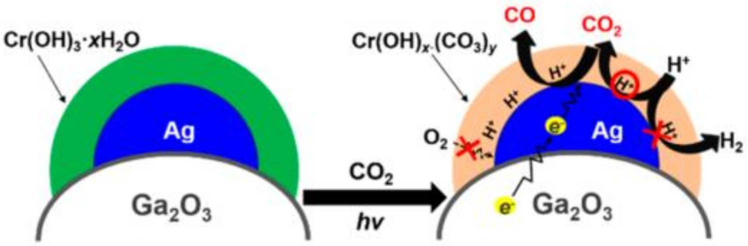

Figure 3. Core–shell structure of Ag@Cr dual cocatalyst loaded on the surface of Ga_2O_3 and mechanism of photocatalytic conversion of CO_2 into CO over Ag@Cr/Ga_2O_3. [80]

In addition, the photocatalytic activity for CO_2 reduction was significantly improved when dual (reduction and oxidation) cocatalysts were simultaneously loaded onto different photocatalyst facets. [34, 60, 79, 82-84] Xie et al. [79] reported that photogenerated electrons from TiO_2 were transferred to Pd during the reduction of CO_2 to formate, whereas photogenerated holes injected into RuO_2 oxidized SO_3^{2-} to SO_4^{2-}. Yoshida et al. [83] reported that Ag and MnO_x species were loaded onto the long and short facets, respectively, of rod-like $K_2Ti_6O_{13}$ crystals and proposed that the Ag and MnO_x species served as CO_2 reduction and O_2 generation promoters, respectively. [34, 83] Li et al. [85] and Zhu et al. [86] reported that loading Pt and MnO_x on the {010} and {100} facets, respectively, of single crystal $BiVO_4$, can strongly improve interfacial charge transfer and increase the intensity of built-in electric fields. They visualized the photogenerated charge distribution on single Pt-and-MnO_x-loaded $BiVO_4$ photocatalyst particles using surface photovoltage (SPV) data, which were obtained using spatially resolved surface photovoltage spectroscopy (SRSPS).[86] The dual cocatalysts loaded on different photocatalyst facets served as reduction and oxidation sites, and promoted the photogenerated electrons and holes to different active sites on the photocatalyst surface. [86-87] Therefore, the recombination rate of photoinduced electron–hole pairs would be significantly lower inside single photocatalyst particles owing to the quick consumption of photogenerated electron–hole pairs at the surface of semiconductors. The synergistic effect of dual cocatalysts plays an important role in enhancing the photocatalytic performance of semiconductor photocatalysts for CO_2 reduction.

Thesis outline

This thesis focuses on enhancing the CO_2 reduction performance of heterogenous photocatalysts. Modification methods, such as metal cation doping, surface modification, and dual cocatalyst engineering, were investigated.

Chapter 1 describes the successful fabrication of Al-$SrTiO_3$ using a facile flux method. Ag/Al-$SrTiO_3$ presented a good photocatalytic activity for CO_2 reduction in aqueous media under light irradiation ($\lambda \geq 300$ nm). Several fabrication condition, cocatalysts, and cocatalyst loading amounts were analyzed. The amount of electrons consumed for H_2 and CO evolution was equal to the amount of holes required for O_2 generation, indicating that H_2O served as the electron donor. Additionally, the particle size and dispersion and chemical state of Ag cocatalyst affected the photocatalytic activity of Ag/Al-$SrTiO_3$ for CO_2 conversion.

Chapter 2 reveals that 4 mol % Al-$SrTiO_3$ exhibited the highest CO formation rate and excellent CO evolution selectivity. The effect of Al^{3+} cation doping amount of Al-$SrTiO_3$ was described in this chapter. Numerous nano-steps formed on the Al-$SrTiO_3$ surface. In addition, Al was doped into the crystal structure of $SrTiO_3$ and replaced a fraction of Ti^{4+} sites; however, a small quantity of alumina was present on the catalyst surface. The amount of Al in single Al-$SrTiO_3$ nanoparticles decreased from the surface to the center of the nanoparticles. Isotope-labeling experiments using $^{13}CO_2$ suggested that CO was derived from the CO_2 bubbled into an aqueous solution of $NaHCO_3$ and not from the residual carbon species on the catalyst surface.

Chapter 3 reports that an extremely high CO_2 reduction efficiency and a CO evolution selectivity of up to 99.7% were achieved over the dual AgCo cocatalyst-loaded Al-$SrTiO_3$

($AgCo/Al-SrTiO_3$) using H_2O as the electron donor. The formation rate of CO over $AgCo/Al-SrTiO_3$ was 10 times higher than over $Ag/Al-SrTiO_3$. The Ag and Co sites on the {100} and {110} facets of $SrTiO_3$, respectively, of $AgCo/Al-SrTiO_3$ facilitated the reduction of CO_2 to CO, and oxidation of H_2O, respectively, under light irradiation ($\lambda \geq 300$ nm) in aqueous solution.

Chapter 4 describes the modification of $Al-SrTiO_3$ with several Ag–M (M = Fe, Co, Ni, and Pt) dual cocatalyst prepared via photodeposition (PD). The $Ag–Fe/Al-SrTiO_3$ catalyst fabricated via PD method, for which Ag and Fe were loaded onto the {100} and {110} facets of $SrTiO_3$, respectively, exhibited good photocatalytic performance for the reduction of CO_2 to CO.

Chapter 5 presents the Zn modification technique used to fabricate a $Ag/Zn/ZnTa_2O_6$ catalyst for the photocatalytic reduction of CO_2 using H_2O as the reducing agent. The CO evolution selectivity of $Ag/Zn/ZnTa_2O_6$ was significantly higher than that of $Ag/ZnTa_2O_6$. It was proposed that the Ag cocatalyst and Zn species could suppress H_2 evolution on the photocatalyst surface. In addition, the photocatalytic performance of the Ag-free, Zn-modified photocatalyst was relatively good; however, the combination of a Ag cocatalyst and Zn modifier was required to ensure high CO selectivity and evolution rate. Moreover, three types of active sites were identified, and they were used for (1) the reduction of CO_2 to CO, (2) the reduction of H^+ to H_2, and (3) the oxidation of H_2O to O_2.

Reference

1. A. Fujishima; K. Honda, *nature* **1972**, 238 (5358), 37.
2. M. Halmann, *Nature* **1978**, 275 (5676), 115-116.
3. T. Inoue; A. Fujishima; S. Konishi; K. Honda, *Nature* **1979**, 277 (5698), 637-638.
4. J. Yang; D. Wang; H. Han; C. Li, *Acc. Chem. Res.* **2013**, 46 (8), 1900-1909.
5. J. Ran; M. Jaroniec; S. Z. Qiao, *Adv. Mater.* **2018**, 30 (7), 1704649.
6. X. Chang; T. Wang; J. Gong, *Energy Environ. Sci.* **2016**, 9 (7), 2177-2196.
7. W. Tu; Y. Zhou; Z. Zou, *Adv. Mater.* **2014**, 26 (27), 4607-4626.
8. A. L. Linsebigler; G. Lu; J. T. Yates Jr, *Chemical reviews* **1995**, 95 (3), 735-758.
9. D. G. Nocera, *Accounts of chemical research* **2012**, 45 (5), 767-776.
10. I.-H. Tseng; W.-C. Chang; J. C. Wu, *Appl. Catal. B* **2002**, 37 (1), 37-48.

11. G. R. Dey; A. Belapurkar; K. Kishore, *J. Photochem. Photobiol. A* **2004**, 163 (3), 503-508.

12. J. L. White; M. F. Baruch; J. E. Pander III; Y. Hu; I. C. Fortmeyer; J. E. Park; T. Zhang; K. Liao; J. Gu; Y. Yan, *Chem. Rev.* **2015**, 115, 12888-12935.

13. X. Li; J. Wen; J. Low; Y. Fang; J. Yu, *Science China Materials* **2014**, 57 (1), 70-100.

14. K. Teramura; T. Tanaka, *Phys. Chem. Chem. Phys.* **2018**, 20 (13), 8423-8431.

15. K. Iizuka; T. Wato; Y. Miseki; K. Saito; A. Kudo, *J. Am. Chem. Soc.* **2011**, 133 (51), 20863-20868.

16. Z. Wang; K. Teramura; S. Hosokawa; T. Tanaka, *Appl. Catal. B* **2015**, 163, 241-247.

17. K. Teramura; H. Tatsumi; Z. Wang; S. Hosokawa; T. Tanaka, *Bull. Chem. Soc. Jpn.* **2015**, 88, 431-437.

18. T. Takayama; A. Iwase; A. Kudo, *Bull. Chem. Soc. Jpn.* **2015**, 88 (4), 538-543.

19. Z. Wang; K. Teramura; S. Hosokawa; T. Tanaka, *J. Mater. Chem. A* **2015**, 3, 11313-11319.

20. S. Iguchi; K. Teramura; S. Hosokawa; T. Tanaka, *Catal. Sci. Technol.* **2016**, 6 (13), 4978-4985.

21. Z. Huang; K. Teramura; S. Hosokawa; T. Tanaka, *Appl. Catal. B* **2016**, 199, 272-281.

22. Z. Wang; K. Teramura; Z. Huang; S. Hosokawa; Y. Sakata; T. Tanaka, *Catal. Sci. & Technol* **2016**, 6, 1025-1032.

23. K. Teramura; Z. Wang; S. Hosokawa; Y. Sakata; T. Tanaka, *Chem. Eur. J.* **2014**, 20 (32), 9906-9909.

24. R. Pang; K. Teramura; H. Asakura; S. Hosokawa; T. Tanaka, *Appl. Catal. B* **2017**, 218, 770-778.

25. A. Anzai; N. Fukuo; A. Yamamoto; H. Yoshida, *Catal. Commun.* **2017**, 100, 134-138.

26. Z. Huang; S. Yoshizawa; K. Teramura; H. Asakura; S. Hosokawa; T. Tanaka, *ACS Omega* **2017**, 2, 8187-8197.

27. H. Tatsumi; K. Teramura; Z. Huang; Z. Wang; H. Asakura; S. Hosokawa; T. Tanaka, *Langmuir* **2017**, 33 (49), 13929-13935.

28. S. Iguchi; Y. Hasegawa; K. Teramura; S. Kidera; S. Kikkawa; S. Hosokawa; H. Asakura; T. Tanaka, *Sustain. Energy Fuels* **2017**, 1 (8), 1740-1747.

29. Z. Huang; K. Teramura; H. Asakura; S. Hosokawa; T. Tanaka, *J. Mater. Chem. A* **2017**, 5

(36), 19351-19357.

30. H. Nakanishi; K. Iizuka; T. Takayama; A. Iwase; A. Kudo, *ChemSusChem* **2017**, 10 (1), 112-118.

31. Z. Huang; K. Teramura; H. Asakura; S. Hosokawa; T. Tanaka, *Catal. Today* **2018**, 300, 173-182.

32. R. Pang; K. Teramura; H. Tatsumi; H. Asakura; S. Hosokawa; T. Tanaka, *Chem. Commun.* **2018**, 54 (9), 1053-1056.

33. X. Zhu; A. Anzai; A. Yamamoto; H. Yoshida, *Appl. Catal. B* **2019**, 243, 47-56.

34. X. Zhu; A. Yamamoto; S. Imai; A. Tanaka; H. Kominami; H. Yoshida, *Chem. Commun.* **2019**, 13514-13517.

35. R. Pang; K. Teramura; M. Morishita; H. Asakura; S. Hosokawa; T. Tanaka, *Commun. Chem.* **2020**, 3 (1), 1-8.

36. W.-J. Ong; L. K. Putri; A. R. Mohamed, *Chem. Eur. J.* **2020**.

37. C. A. Gueymard, *Solar energy* **2004**, 76 (4), 423-453.

38. K. Wang; L. Zhang; Y. Su; S. Sun; Q. Wang; H. Wang; W. Wang, *Catal. Sci. Technol.* **2018**, 8 (12), 3115-3122.

39. S. Kikkawa; K. Teramura; H. Asakura; S. Hosokawa; T. Tanaka, *J. Phys. Chem. C* **2018**, 122, 21132-21139.

40. H. Huang; X. Li; J. Wang; F. Dong; P. K. Chu; T. Zhang; Y. Zhang, *ACS Catal.* **2015**, 5, 4094-4103.

41. D. Pérez-del-Rey; D. Forgács; E. M. Hutter; T. J. Savenije; D. Nordlund; P. Schulz; J. J. Berry; M. Sessolo; H. J. Bolink, *Adv. Mater.* **2016**, 28 (44), 9839-9845.

42. H.-C. Chen; C.-W. Huang; J. C. Wu; S.-T. Lin, *J. Phys. Chem. C* **2012**, 116, 7897-7903.

43. K. Iwashina; A. Kudo, *J. Am. Chem. Soc.* **2011**, 133 (34), 13272-13275.

44. X. Ma; X. Cui; Z. Zhao; M. A. Melo; E. J. Roberts; F. E. Osterloh, *J. Mater. Chem. A* **2018**, 6 (14), 5774-5781.

45. K. Iwashina; A. Kudo, *J. Am. Chem. Soc.* **2011**, 133, 13272-13275.

46. A. Wagner; C. D. Sahm; E. Reisner, *Nature Catal.* **2020**, 1-12.

47. S. Xie; Y. Wang; Q. Zhang; W. Deng; Y. Wang, *ACS Catal.* **2014**, 4 (10), 3644-3653.

48. M. Ram Reddy; Z. Xu; G. Lu; J. Diniz da Costa, *Ind. Eng. Chem. Res.* **2006**, 45 (22), 7504-7509.

49. S. Bernal; F. Botana; R. Garcia; J. Rodriguez-Izquierdo, *Reactivity of solids* **1987**, 4 (1-2), 23-40.

50. Y. Sakata; Y. Matsuda; T. Nakagawa; R. Yasunaga; H. Imamura; K. Teramura, *ChemSusChem* **2011**, 4 (2), 181-184.

51. C. T. Campbell; C. H. Peden, *Science* **2005**, 309 (5735), 713-714.

52. T. Motohashi; T. Takahashi; M. Kimura; Y. Masubuchi; S. Kikkawa; Y. Kubota; Y. Kobayashi; H. Kageyama; M. Takata; S. Kitagawa, *J. Phys. Chem. C* **2015**, 119 (5), 2356-2363.

53. A. Iwase; H. Kato; A. Kudo, *ChemSusChem* **2009**, 2, 873-877.

54. J. Lee; D. C. Sorescu; X. Deng, *J. Am. Chem. Soc.* **2011**, 133 (26), 10066-10069.

55. M. Wang; M. Shen; X. Jin; J. Tian; M. Li; Y. Zhou; L. Zhang; Y. Li; J. Shi, *ACS Catal.* **2019**, 9 (5), 4573-4581.

56. K. Xie; N. Umezawa; N. Zhang; P. Reunchan; Y. Zhang; J. Ye, *Energy Environ. Sci.* **2011**, 4 (10), 4211-4219.

57. H. Tan; Z. Zhao; W. B. Zhu; E. N. Coker; B. Li; M. Zheng; W. Yu; H. Fan; Z. Sun, *ACS Appl. Mater. Interfaces* **2014**, 6 (21), 19184-19190.

58. J. Yu; J. Low; W. Xiao; P. Zhou; M. Jaroniec, *J. Am. Chem. Soc.* **2014**, 136, 8839-8842.

59. S. Liu; J. Yu; M. Jaroniec, *J. Am. Chem. Soc.* **2010**, 132 (34), 11914-11916.

60. Q. Liu; Y. Zhou; J. Kou; X. Chen; Z. Tian; J. Gao; S. Yan; Z. Zou, *J. Am. Chem. Soc.* **2010**, 132 (41), 14385-14387.

61. Q. Liu; D. Wu; Y. Zhou; H. Su; R. Wang; C. Zhang; S. Yan; M. Xiao; Z. Zou, *ACS Appl. Mater. Interfaces* **2014**, 6 (4), 2356-2361.

62. L. Ye; J. Mao; T. Peng; L. Zan; Y. Zhang, *Phys. Chem. Chem. Phys.* **2014**, 16 (29), 15675-15680.

63. H. Abdullah; M. M. R. Khan; H. R. Ong; Z. Yaakob, *J. CO_2 Util.* **2017**, 22, 15-32.

64. H. Park; Y. Park; W. Kim; W. Choi, *J. Photoch. Photobio. C* **2013**, 15, 1-20.

65. R. Daghrir; P. Drogui; D. Robert, *Ind. Eng. Chem. Res.* **2013**, 52 (10), 3581-3599.

66. V. P. Indrakanti; J. D. Kubicki; H. H. Schobert, *Energy & fuels* **2008**, 22 (4), 2611-2618.

67. J. Sato; H. Kobayashi; K. Ikarashi; N. Saito; H. Nishiyama; Y. Inoue, *J. Phys. Chem. B* **2004**, 108 (14), 4369-4375.

68. J. Huang; K. Ding; Y. Hou; X. Wang; X. Fu, *ChemSusChem* **2008**, 1 (12), 1011-1019.

69. O. K. Varghese; M. Paulose; T. J. LaTempa; C. A. Grimes, *Nano Lett.* **2009**, 9 (2), 731-737.

70. T. Yui; A. Kan; C. Saitoh; K. Koike; T. Ibusuki; O. Ishitani, *ACS Appl. Mater. Interfaces* **2011**, 3 (7), 2594-2600.

71. K. Sayama; H. Arakawa, *J. Phys. Chem.* **1993**, 97 (3), 531-533.

72. P.-W. Pan; Y.-W. Chen, *Catal. Commun.* **2007**, 8 (10), 1546-1549.

73. R. Pang; K. Teramura; H. Asakura; S. Hosokawa; T. Tanaka, *ACS Appl. Energy Mater.* **2019**, 2 (8), 5397-5405.

74. S. t. Neaţu; J. A. Maciá-Agulló; P. Concepción; H. Garcia, *J. Am. Chem. Soc.* **2014**, 136 (45), 15969-15976.

75. Q. Kang; T. Wang; P. Li; L. Liu; K. Chang; M. Li; J. Ye, *Angew. Chem. Int. Ed.* **2015**, 54 (3), 841-845.

76. C.-W. Tsai; H. M. Chen; R.-S. Liu; K. Asakura; T.-S. Chan, *J. Phys. Chem. C* **2011**, 115 (20), 10180-10186.

77. Q. Zhai; S. Xie; W. Fan; Q. Zhang; Y. Wang; W. Deng; Y. Wang, *Angew. Chem. Int. Ed.* **2013**, 52 (22), 5776-5779.

78. X. Yu; V. V. Ordomsky; A. Y. Khodakov, *ChemCatChem* **2020**, 12 (3), 740-749.

79. T.-f. Xie; D.-j. Wang; L.-j. Zhu; T.-j. Li; Y.-j. Xu, *Mater. chem. phys.* **2001**, 70 (1), 103-106.

80. R. Pang; K. Teramura; H. Asakura; S. Hosokawa; T. Tanaka, *ACS Sustainable Chem. Eng.* **2018**, 7 (2), 2083-2090.

81. R. Pang; K. Teramura; H. Asakura; S. Hosokawa; T. Tanaka, *J. Phys. Chem. C* **2019**, 123 (5), 2894-2899.

82. Y. Bai; L. Ye; L. Wang; X. Shi; P. Wang; W. Bai, *Environ. Sci.: Nano* **2016**, 3 (4), 902-909.

83. X. Zhu; A. Yamamoto; S. Imai; A. Tanaka; H. Kominami; H. Yoshida, *Appl. Catal. B* **2020**, 119085.

84. Y. Wang; T. He, *J. Mater. Chem. A* **2020**, 9, 87-110.

85. R. Li; F. Zhang; D. Wang; J. Yang; M. Li; J. Zhu; X. Zhou; H. Han; C. Li, *Nat. Commun.*

2013, 4, 1432.

86. J. Zhu; S. Pang; T. Dittrich; Y. Gao; W. Nie; J. Cui; R. Chen; H. An; F. Fan; C. Li, *Nano Lett.* **2017**, 17 (11), 6735-6741.

87. T. Takata; J. Jiang; Y. Sakata; M. Nakabayashi; N. Shibata; V. Nandal; K. Seki; T. Hisatomi; K. Domen, *Nature* **2020**, 581 (7809), 411-414.

Chapter 1

Optimized Synthesis of Ag-Modified Al-Doped $SrTiO_3$ Photocatalyst for the Conversion of CO_2 Using H_2O as an Electron Donor

Abstract

Ag-modified Al-doped $SrTiO_3$ (Ag/Al-$SrTiO_3$) was fabricated via a flux method and was found to exhibit high efficiency and selectivity toward CO evolution using H_2O as an electron donor under photoirradiation at wavelengths greater than 300 nm. The fabrication conditions, such as calcination temperature and time, were optimized in this study because these factors had obvious effects on the crystallinity, microstructure, and degree of Al doping of the Al-$SrTiO_3$ photocatalysts. The 1.0-wt.% Ag/Al-$SrTiO_3$ photocatalyst fabricated by chemical reduction showed a good rate (5.5 μmol h^{-1}) of CO formation. Moreover, excellent selectivity (98.8%) was achieved. Importantly, the O_2 formation rate was 2.7 μmol h^{-1}, which indicates that the number of estimated holes was equivalent to the number of electrons estimated from the CO formation rate. Thus, H_2O is the electron donor in this case. In addition, the charge separation in $SrTiO_3$ was significantly promoted after Ag modification and Al doping, and the Ag cocatalyst particle size and dispersion, as well as the chemical state of Ag, affected the photocatalytic activity.

Introduction

The conversion of carbon dioxide (CO_2) into chemicals such as carbon monoxide (CO), formic acid (HCOOH), methanol (CH_3OH), methane (CH_4), and other organic chemicals using solar energy over heterogeneous photocatalysts, so-called artificial photosynthesis,[1-2] is a promising method to enable renewable resource generation and has become a highly topical issue[3-7] since Halmann[8] and Inoue[9] et al. first proposed the photocatalytic conversion of CO_2 in the 1970s. To date, many types of photocatalyst have been applied to the photoreduction of CO_2 into useful chemicals in aqueous solution using H_2O as the electron donor.[5, 10-14] In this photocatalytic reaction system, a stoichiometric amount of O_2 (an oxidative product) must be continuously evolved when using H_2O as the electron donor to achieve the equivalent consumption of electrons and holes during the reaction.[5, 15-16] In addition to CO evolution, H_2 is evolved as a reductive product, and this is a competitive reaction with CO evolution in aqueous solution.

Titanate-based materials are widely used photocatalysts for water splitting,[17-18] the degradation of organic compounds, [19-20] and the reduction of CO_2.[9, 21-26] However, only a few titanate-based materials, such as Ag-loaded $ALa_4Ti_4O_{15}$ (where A = Ca, Sr, and Ba),[21] Ag-loaded $La_2Ti_2O_7$,[22] AgMn-loaded $K_2Ti_6O_{13}$,[23] and Ag/$CaTiO_3$,[26] show good photocatalytic performance for the reduction of CO_2 in aqueous solution and continuously produce stoichiometric amounts of O_2 during the reaction. Nevertheless, most of the photocatalysts only function under UV irradiation ($250 < \lambda < 350$ nm) because of the high reduction potential required for the photocatalytic reduction of CO_2. Solar energy is a clean and sustainable energy source, and the solar flux reaching the top of the atmosphere is 1366 W m^{-2}. However, only a small fraction of the solar energy is distributed in the UV region ($\lambda <$ 400 nm).[27] Thus, to exploit photocatalytic CO_2 reduction using solar energy, the band gap of the photocatalyst should be narrowed. Consequently, the design and development of photocatalysts that can achieve the reduction of CO_2 via photoirradiation over a broad range of wavelengths are required.

It has been reported that Al-doped strontium titanate (Al-$SrTiO_3$ or STO:Al), which has a band gap of 3.2 eV, shows good photocatalytic performance for overall water splitting in the presence of cocatalysts when irradiated with light having a wavelength shorter than 390 nm; further, sacrificial reagents are not required, and the apparent quantum efficiency of RhCrO$_x$/STO:Al is approximately 69% at 365 nm.[28-29] Previously, the group of Kyoto University found that Al-SrTiO$_3$ fabricated using a flux method has several nanometer-sized stepwise edges on the surface, and this catalyst has a good CO formation rate, as well as a high selectivity for CO evolution, in aqueous solutions. It is known that the crystallinity and Brunauer–Emmett–Teller (BET) surface area, which are influenced by the fabrication conditions such as calcination temperature and time, can affect the properties of photocatalysts.[30-31] Thus, it is important to find a balance between the crystallinity and BET surface area to optimize the conversion of CO$_2$ and the selectivity toward CO evolution because the two factors have a trade-off relationship, i.e., the crystallinity increases with decrease in the BET surface area. More importantly, the calcination conditions also affect the doping and microstructure of the photocatalysts significantly.[28] Herein, the author demonstrates the effect of fabrication conditions, such as calcination temperature and time, on the properties of Al-SrTiO$_3$ and the photocatalytic performance for the conversion of CO$_2$ into CO using H$_2$O as an electron donor under photoirradiation.

Furthermore, the cocatalyst on the surface of the photocatalyst plays an important role during the photocatalytic reaction process. Kudo et al. first reported that Ag-loaded ALa$_4$Ti$_4$O$_{15}$ shows good selectivity for the photocatalytic conversion of CO$_2$ into CO in aqueous solution rather than H$_2$ evolution, as compared to pristine ALa$_4$Ti$_4$O$_{15}$.[21] This Ag cocatalyst has been widely used for the conversion of CO$_2$ into CO with water as an electron donor under photoirradiation.[5, 11, 14, 30, 32-34] The Ag cocatalyst has been reported to enhance the selectivity toward CO evolution and also improve the photocatalytic activity related to charge transfer. Thus, in this study, the Ag cocatalyst was loaded onto Al-SrTiO$_3$ using various methods, and the effect of the amount of loaded Ag was investigated.

Experimental Section

Preparation of Al-SrTiO$_3$

Al-doped SrTiO$_3$ photocatalysts were fabricated via a flux method using anhydrous SrCl$_2$ as the flux reagent. After grinding, the stoichiometric mixtures of SrTiO$_3$ (0.01 mol, 99.9%, Wako, Japan), Al$_2$O$_3$ (0.0002 mol, < 50 nm particle size, Sigma–Aldrich, Germany), and anhydrous SrCl$_2$ (0.1 mol, 98.0%, Kanto Chemical Co., Inc., Japan) were calcined at 1273, 1323, 1373, 1423, or 1473 K for 10 h in air or calcined at 1423 K for 1, 5, 10, 15, or 20 h in air.

Cocatalyst loading

An Ag cocatalyst was employed to modify the surface of the as-prepared Al-$SrTiO_3$ photocatalyst via the chemical reduction (CR) method. More specifically, Al-$SrTiO_3$ (0.75 g) was dispersed in deionized ultrapure water (50 mL), and a 0.1 M aqueous solution of $AgNO_3$ (0.695 mL) and 0.4 M aqueous solution of NaH_2PO_2 (0.75 mL) were added to the suspension. After maintaining the suspension at a constant temperature of 353 K for 1.5 h, it was filtered and then dried under air at 298 K overnight. The Ag cocatalyst was also loaded on the Al-doped $SrTiO_3$ by photodeposition (PD). Subsequently, 0.75 g of Al-$SrTiO_3$ was dispersed in deionized ultrapure water (1.0 L), and a 0.1 M aqueous solution of $AgNO_3$ (0.695 mL) was added to the suspension. After the flow of Ar gas through the solution for 1.0 h, the suspension was irradiated using a 400-W high-pressure Hg lamp with a quartz jacket connected to a water-cooling system, and Ar gas was bubbled into the suspension at a flow rate of 30 mL min^{-1}. Subsequently, vacuum filtration and drying of the cocatalyst-loaded Al-$SrTiO_3$ was carried out at 298 K in air overnight. The Ag cocatalyst was also loaded on the Al-$SrTiO_3$ catalyst using the impregnation (IMP) method; in this process, Al-$SrTiO_3$ (0.75 g) was dispersed in deionized ultrapure water (20 mL), and a 0.1 M aqueous solution of $AgNO_3$ (0.695 mL) was added to the suspension. After aging at 353 K for 0.5 h, the water was completely evaporated at 353 K. Finally, the dried mixture was ground and calcined at 723 K for 2 h in air.

Characterization

The structure and crystalline nature of the prepared Al–$SrTiO_3$ were characterized by X-ray diffraction (XRD) using a Rigaku Ultima IV powder diffractometer and Cu K_α (λ = 0.154056 nm) radiation generated at a voltage and current of 40 kV and 40 mA, respectively. UV-visible diffuse reflectance spectroscopy (UV-vis DRS) was performed using a JASCO V-670 spectrometer equipped with an integrating sphere. Spectralon®, supplied by Labsphere Inc., was used as a standard reflection sample. Scanning electron microscopy (SEM) images were obtained using a field-emission scanning electron microscope (SU-8220, Hitachi High-Technologies) equipped with an energy dispersive X-ray spectroscopy (EDS) unit at an acceleration voltage of 15.0 kV. X-ray photoelectron spectroscopy (XPS) was recorded using an X-ray photoelectron spectrometer (ESCA 3400, Shimadzu Corp.). Inductively coupled plasma-optical emission spectrometry (ICP-OES, iCAP7400, Thermo Fisher Scientific, Inc.) was used to determine the metal compositions in the Al-$SrTiO_3$. An FT-IR spectrometer (FT/IR-4700, JASCO Corp.) was used to collect the FT-IR spectra of the adsorbed CO_2 species on the surface of the $SrTiO_3$ and Al-$SrTiO_3$ photocatalysts. For measurement, a photocatalyst sample (50 mg) was pressed into a 10 mm-diameter wafer. Then, the wafer was placed into cylindrical cell with a CaF_2 window and a water-cooling system. Before each measurement, the wafer was treated at 673 K for 30 min under vacuum. Subsequently, O_2 was introduced into the cylindrical cell, and the sample was maintained at 673 K for 30 min, followed by treatment under vacuum at 673 K for a further 30 min. This process was applied to remove the any organic contaminants and water from the wafer. After the wafer had cooled to 303 K, CO_2 (3.2 kPa) was introduced into the cell for measurement. The measurements were made in transmission mode, and data from 128 scans were accumulated at a resolution of 4 cm^{-1}.

Photocatalytic reaction

The photocatalytic conversion of CO_2 using H_2O as an electron donor was performed in a quasi-flow batch system with an internal-irradiation-type reaction vessel at 25 °C and under ambient pressure. Ag-loaded Al-$SrTiO_3$ (0.5 g) was dispersed in a 0.1 M aqueous solution of $NaHCO_3$ (1.0 L), and CO_2 gas (99.999%) was bubbled into the suspension at a flow rate of 30 mL min^{-1}. The suspension was then irradiated using a 400-W high-pressure Hg lamp with a Pyrex® jacket connected to a water-cooling system to cut off any light with $\lambda < 300$ nm. The gaseous products evolved from the photoreaction system (e.g., H_2, O_2, and CO) were detected using a thermal conductivity detector–gas chromatography (TCD–GC) and a GC-8A chromatograph (Shimadzu Corp.) equipped with a MS-5A column and Ar as the carrier gas or by flame ionization detector–gas chromatography (FID–GC) using a methanizer and a ShinCarbon ST column with N_2 as the carrier gas.

Results and Discussion

Figure 1(A) shows the XRD patterns of Al–$SrTiO_3$ samples fabricated at different temperatures. All diffraction peaks can be attributed to the pure perovskite structure of $SrTiO_3$ without any impurity peaks. The full width at half maximum (FWHM) of the (110) peak decreased with increase in the calcination temperature of $SrTiO_3$ (as shown in Table 1), indicating that the crystallinity of the samples increased after calcination. On increasing the calcination temperature from 1373 to 1473 K, the FWHM value of the (110) reflection showed no obvious changes, which suggests that the crystallinity was not improved in this temperature range. Moreover, the BET surface area was stable at 3.6 $m^2\ g^{-1}$ when the calcination temperature was lower than 1423 K (Table 1). Furthermore, the BET surface area decreased to 2.9 $m^2\ g^{-1}$ on calcination at 1473 K. No remarkable changes, such as new absorption edges or peaks, were observed in the UV-Vis DR spectra after the doping of $SrTiO_3$ with Al at different calcination temperatures (as shown in Figure 1(B)), which also indicates that the calcination temperature had no effect on the band gap of Al–$SrTiO_3$.

SEM images of the $SrTiO_3$ and Al–$SrTiO_3$ samples prepared at various temperature are shown in Figure 2. As mentioned in previous work,[35] many nanosteps appeared on the surface of the sample after doping of Al species into $SrTiO_3$. Interestingly, Figures 2(b)–(f) show that the nanosteps on the surface of the samples became clearer as the calcination temperature increased from 1273 to 1473 K during fabrication. However, the calcination temperature had almost no effect on the particle size of the Al–$SrTiO_3$ photocatalyst.

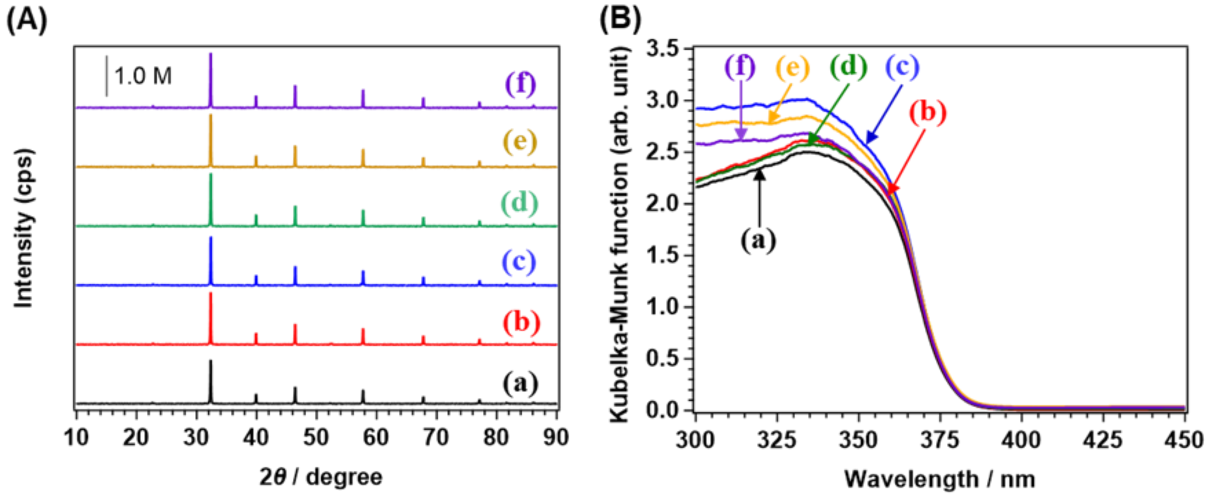

Figure 1. (A) XRD patterns and (B) UV-Vis DR spectra of (a) pristine $SrTiO_3$ and 4 mol% Al-$SrTiO_3$ calcined at (b) 1273, (c) 1323, (d) 1373, (e) 1423, and (f) 1473 K in air for 10 h.

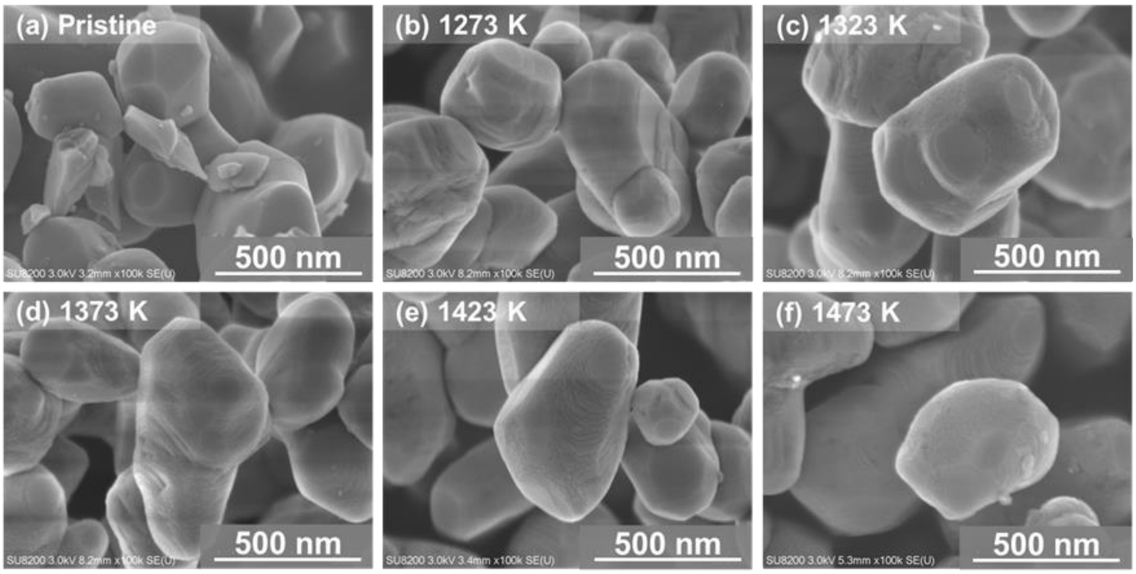

Figure 2. SEM images of the (a) pristine $SrTiO_3$ and 4 mol% Al–$SrTiO_3$ calcined at (b) 1273, (c) 1323, (d) 1373, (e) 1423, and (f) 1473 K in air for 10 h.

Table 1. BET surface area, FWHM of the {110} diffraction peak of Al–$SrTiO_3$ fabricated in different conditions.

Calcination condition	**BET/m^2 g^{-1}**	**FMHW/ deg.**	**ICP Al/(Al+Ti) %**
Pristine STO	3.7	0.105	0.76
Al–$SrTiO_3$_10 h_1273 K	3.5	0.091	1.9
Al–$SrTiO_3$_10 h_1323 K	3.7	0.084	3.1
Al–$SrTiO_3$_10 h_1373 K	3.6	0.088	3.2
Al–$SrTiO_3$_10 h_1423 K	3.6	0.084	4.0
Al–$SrTiO_3$_10 h_1473 K	2.9	0.083	4.2
Al–$SrTiO_3$_1423 K_1 h	3.2	0.090	1.9
Al–$SrTiO_3$_1423 K_5 h	3.4	0.084	2.6
Al–$SrTiO_3$_1423 K_10 h	3.6	0.089	4.0
Al–$SrTiO_3$_1423 K_15 h	4.3	0.086	3.6
Al–$SrTiO_3$_1423 K_20 h	3.7	0.087	3.7

Figure 3 shows the formation rates of CO, H_2, and O_2 as products and the selectivity toward CO evolution for the photocatalytic conversion of CO_2 using H_2O as an electron donor over Ag/Al–$SrTiO_3$ prepared by calcination at various temperatures for 15 h. As shown, the formation rates of CO, H_2, and O_2, which indicate the photocatalytic activity, were significantly enhanced after calcination, and all the Ag/Al–$SrTiO_3$ photocatalysts exhibited excellent selectivity (> 96%) toward CO evolution. For the samples prepared at higher calcination temperatures, the photocatalytic activities were improved gradually. The highest rate of CO formation (4.1 μmol h^{-1}) was obtained over the Ag/Al–$SrTiO_3$ sample calcined at 1423 K. However, when the calcination temperature was increased to 1473 K, the photocatalytic activity suddenly decreased.

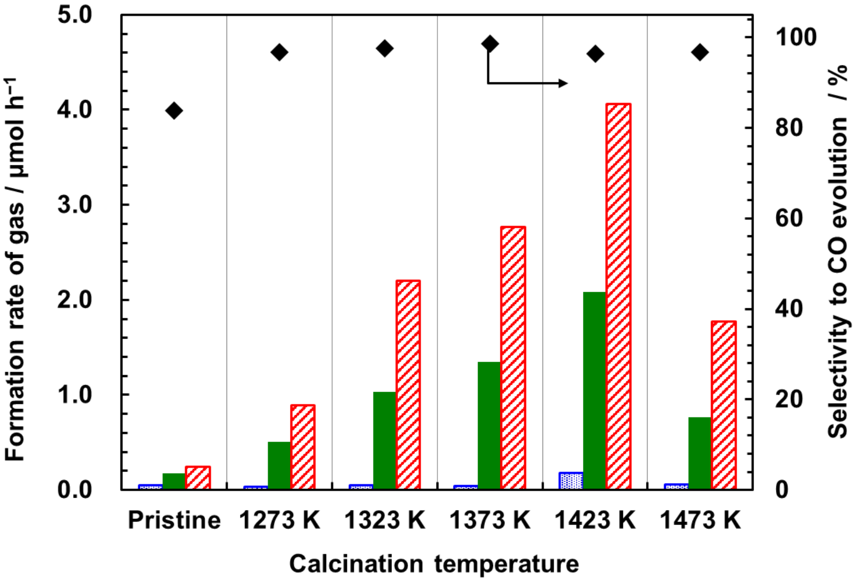

Figure 3. Formation rates of H_2 (blue dotted), O_2 (green filled), and CO (red slashed) and the selectivity toward CO evolution for the photocatalytic conversion of CO_2 using H_2O as an electron donor over pristine $SrTiO_3$ and Al–$SrTiO_3$ fabricated at 1273, 1323, 1373, 1423, and 1473 K in air for 10 h, respectively. Amount of photocatalyst: 0.5 g, Ag loading: 1.0 wt.%, volume of reaction solution (H_2O): 1.0 L, additive: 0.1 M $NaHCO_3$, CO_2 flow rate: 30 mL min^{-1}, and light source: 400-W high-pressure Hg lamp with a Pyrex® jacket to cut off light at $\lambda < 300$ nm.

Thus, the author selected 1423 K as the optimal calcination temperature to obtain the highest rate of CO formation. On the other hand, not only the calcination temperature but also the calcination time are important factors affecting the photocatalytic activity and selectivity. The samples were also characterized by XRD, UV-vis DRS, and SEM, as shown in Table 1 and Figures 4 and 5. The same trend was observed as that in the case of calcination temperature. Figure 6 shows the formation rates of H_2, O_2, and CO and the selectivity toward CO evolution for the photocatalytic conversion of CO_2 using H_2O as an electron donor over Ag-modified Al–$SrTiO_3$ calcined at 1423 K for various hours. The formation rates of H_2, O_2, and CO increased with increase in calcination time to 15 h, and the maximum formation rate of CO was achieved at 15 h of calcination time but decreased slightly at higher calcination temperatures. In particular, note that the photocatalytic product (CO) is derived from the CO_2 bubbled through the system rather than other adventitious carbon sources.[35]

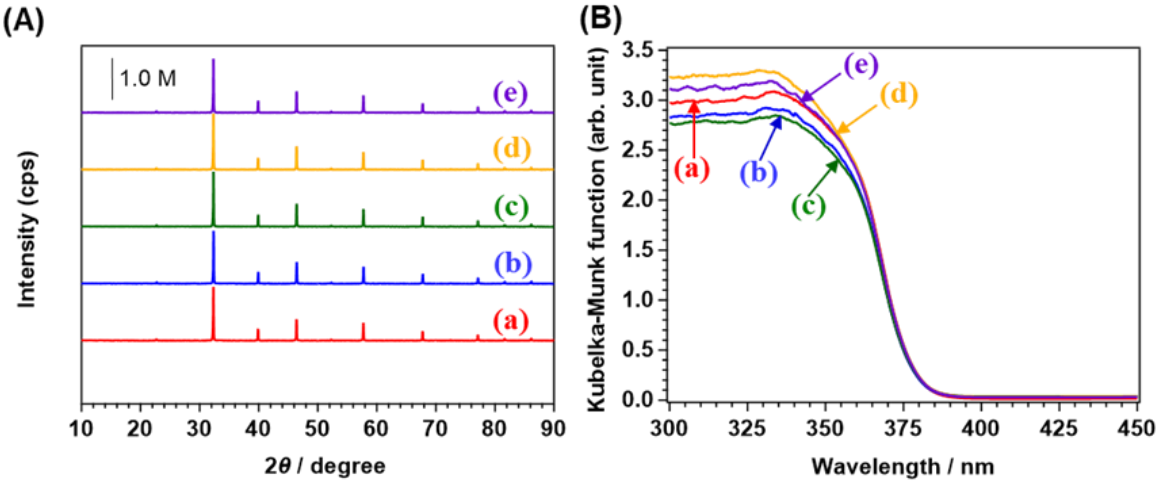

Figure 4. (A) XRD patterns and (B) UV-vis DR spectra of Al–$SrTiO_3$ calcined at 1423 K in air for (a) 1, (b) 5, (c) 10, (d)15, and (e) 20 h

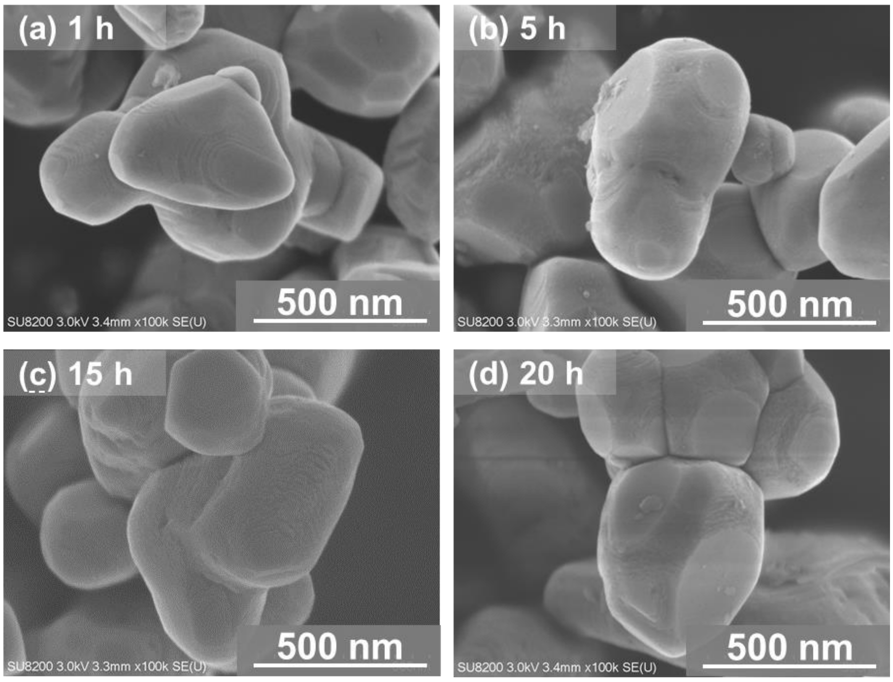

Figure 5. SEM images of the 4 mol% Al–$SrTiO_3$ calcined at 1473 K for (a) 1 h, (b) 5 h, (c) 15 h, and (d) 20 h.

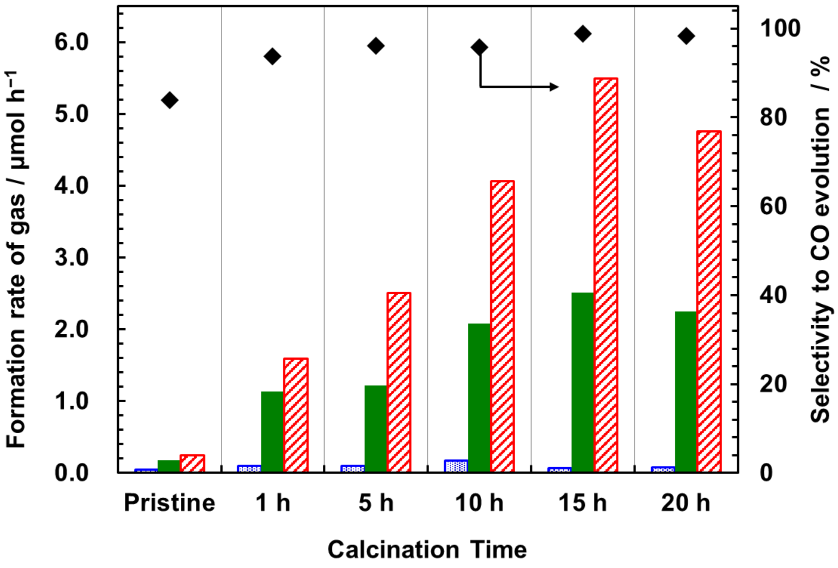

Figure 6. Formation rates of H_2 (blue dotted), O_2 (green filled), and CO (red slashed) and the selectivity toward CO evolution for the photocatalytic conversion of CO_2 using H_2O as an electron donor over pristine Al–$SrTiO_3$ fabricated at 1423 K for 1, 5, 10, 15, and 20 h, respectively. Amount of photocatalyst: 0.5 g, Ag loading: 1.0 wt.%, volume of reaction solution (H_2O): 1.0 L, additive: 0.1 M $NaHCO_3$, CO_2 flow rate: 30 mL min^{-1}, and light source: 400-W high-pressure Hg lamp with a Pyrex® jacket to cut off light at $\lambda < 300$ nm.

The calcination conditions affect the physical properties of the samples such as crystallinity, microstructure, and the bandgap of the samples; and these could affect the photocatalytic performance of the photocatalysts.[22, 30-31] In this work, the author focused on the amount of Al dopant as a differentiator affecting the formation rate of CO and selectivity toward CO evolution for the photocatalytic conversion of CO_2 with H_2O as an electron donor. The ratio of Al in the Al–$SrTiO_3$ samples prepared under different conditions were detected by ICP–OES and are listed in Table 1. As mentioned in the previous works, Al from the environment could influence the ICP-OES result, which is the reason why 0.76% Al was detected in the pristine $SrTiO_3$. Therefore, the value of Al/(Ti + Al) (Table 1 and Figure 7) detected by ICP–OES includes background effects.[35] Figure 7 shows the relationship between the CO formation rate and the degree of Al doping. These results show that the degree of Al doping increased with increase in calcination temperature or time. In addition, the formation rate of CO showed a similar trend to the amount of Al dopant. Specifically, when the Al/(Al + Ti) ratio was higher than 3.5%, the CO formation rate was far from the fitting line, which suggests that factors other than the Al ratio, which are affected by the calcination conditions, may affect the photocatalytic performance of Al–$SrTiO_3$. However, the author found that, if the amount of the Al was too high, the formed defects might have a negative effect on the activity.[36] Thus, the photocatalytic activity of Ag/Al–$SrTiO_3$ is dependent on the molar ratio of Al in the photocatalysts at lower Al contents.

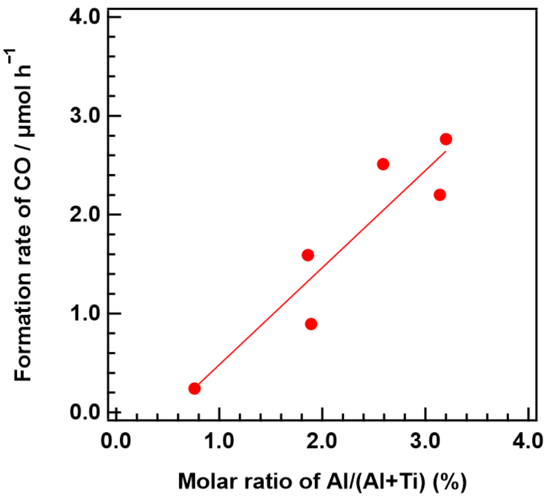

Figure 7. Relationship between the CO formation rate and the Al/(Al + Ti) ratio detected by ICP–OES

The Ag cocatalyst has been reported to have a significant effect on the photocatalytic activity and the selectivity toward CO evolution of the photocatalytic CO_2 reduction reaction.[11, 21, 30] Thus, it is important to investigate the loading and fabrication of the Ag cocatalyst. Figure 8 shows the change with time of the rates of H_2, O_2, and CO formation and the selectivity toward CO evolution for the photocatalytic conversion of CO_2 using H_2O as an electron donor over Ag/Al–$SrTiO_3$. Surprisingly, there was almost no activity in the case of Ag/Al–$SrTiO_3$ fabricated by the IMP method. Ag/Al–$SrTiO_3$ prepared by the CR method showed the highest selectivity toward CO evolution (98.8%). The formation rate of CO was stable at 5.5 μmol h^{-1} over 5 h photocatalytic reaction. The highest formation rate of CO (10.2 μmol h^{-1}) with 70.5% selectivity toward CO evolution was observed in the initial cycles over Ag/Al–$SrTiO_3$ fabricated by the PD method; however, subsequently, CO production dramatically decreased. The formation rate of H_2 increased with decrease in the formation of CO, although the formation rate of O_2 was stable. Thus, these results indicate that the total photocatalytic activity was stable over the Ag/Al–$SrTiO_3$ fabricated by the CR method.

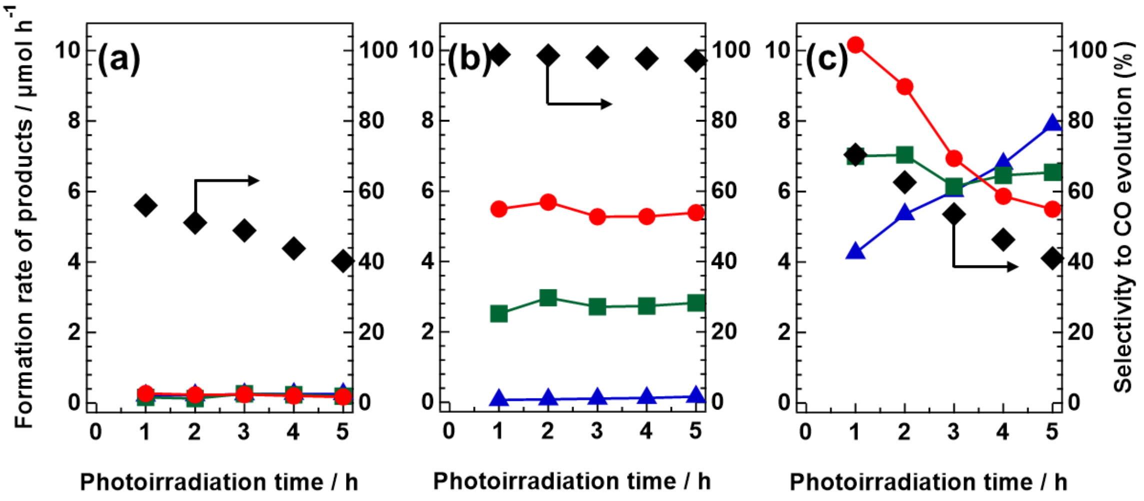

Figure 8. Formation rates of H_2 (blue triangle), O_2 (green square), and CO (red circle) for the photocatalytic conversion of CO_2 using H_2O as an electron donor and the selectivity to CO evolution (black diamond) over (a) Ag/Al-$SrTiO_3$ (IMP method), (b) Ag/Al-$SrTiO_3$ (CR method), and (c) Ag/Al-$SrTiO_3$ (PD method).

The Ag 3d X-ray photoelectron spectra of Ag/Al–$SrTiO_3$ prepared by different methods and the

Auger parameters are given in Figures 9(A) and 9(B), respectively. The Ag XPS peaks for Ag $3d_{5/2}$ and Ag $3d_{3/2}$ indicate the presence of Ag; however, it is difficult to remove the charging effect and distinguish the chemical state of the Ag clearly. Thus, the Auger parameters were calculated using the binding energy (Ag $3d_{5/2}$) and the kinetic energy ($M_4N_{45}N_{45}$) (as shown in the Figure 10).[37-39] The Auger parameters (Figure 9B) indicate that the chemical state of Ag in the sample prepared by the IMP method is AgO (725.0 eV).[40] On the other hand, the relevant peaks in the spectra of the Ag/Al-$SrTiO_3$ samples prepared by the CR and PD methods were located at around 726.0 eV and corresponded to metallic Ag.[39-40]

The UV-vis DR spectra of the Ag/Al–$SrTiO_3$ catalysts are shown in Figure 9(C). A broad absorption band corresponding to surface plasmon resonance was observed in the case of the Ag/Al–$SrTiO_3$ samples fabricated by both CR and PD methods. The peak positions and intensities are different because the size distribution of Ag/Al–$SrTiO_3$ fabricated by the CR method was different from that fabricated by the PD method, as shown in Figures 11(b) and 11(c). On the other hand, in the case of the IMP method, there was no absorption, which means that AgO was generated on the surface, as mentioned above.[30, 41]

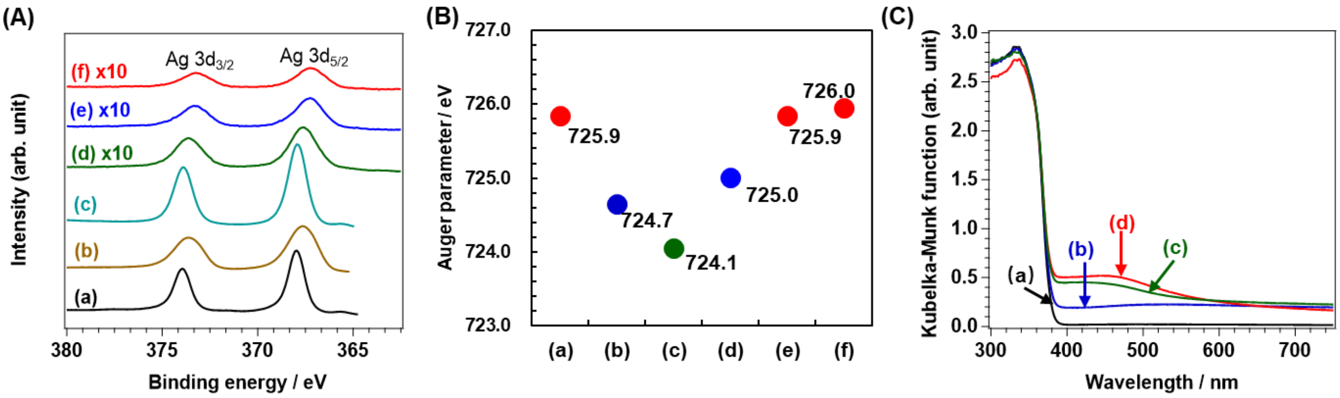

Figure 9. (A) XPS spectra of Ag 3d (a) Ag, (b) AgO, (c) Ag_2O, (d) Ag_IMP, (e) Ag_CR, and (f) Ag_PD. (B) Auger parameters of the various Ag species (a) Ag, (b) AgO, (c) Ag_2O, (d) Ag_IMP, (e) Ag_CR, and (f) Ag_PD. (C) UV-vis DR spectra of (a) Al–$SrTiO_3$ and Ag/Al–$SrTiO_3$ fabricated by (b) IMP, (c) CR, and (d) PD methods.

Next, SEM images of the Ag/Al–$SrTiO_3$ samples modified by all methods were collected before and after 5 h of photocatalytic conversion of CO_2 using H_2O as an electron donor, as shown in Figure 11. Figures 11(a)–(c) show the SEM images of Ag/Al–$SrTiO_3$ samples prepared by different methods (IMP, CR, PD, respectively). The particle size of the Ag cocatalyst on the surface of Al–$SrTiO_3$ prepared by the IMP method was less than 5 nm, as shown in Figure 11(a). On the other hand, in the case of the CR method, Ag cocatalyst particles from 5 to 25 nm were randomly dispersed on the surface, as shown in Figure 11(b). Interestingly, the Ag cocatalysts prepared using the PD method only appeared on the smooth facets of Al–$SrTiO_3$, and the particle sizes ranged from approximately 10 to 40 nm, as shown in Figures 11(c) and 12, which indicates that the size of these Ag cocatalysts was larger than those fabricated by using the IMP and CR methods. Figures 8(d–f) show aggregated Ag nanoparticles, which are, thus, much larger than those before reaction. The author found that the Ag Auger parameter of Ag/Al–$SrTiO_3$ prepared by IMP was similar to that of AgO (see Figure 9(B)), whereas the Ag Auger parameters of the samples prepared by the CR and PD methods could be assigned to metallic Ag. The XPS analysis shown in Figure 13 indicates that the Auger parameters of Ag in the Ag/Al–$SrTiO_3$ samples prepared by IMP, CR, and PD methods were 725.8, 726.1, and 726.2 eV, respectively. This indicates that, after photocatalytic reaction, the chemical state of Ag in all samples was metallic.

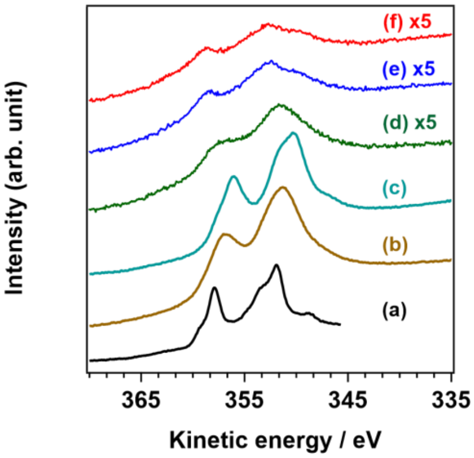

Figure 10. the X-ray-excited Ag MNN Auger spectra of (a) Ag, (b) AgO, (c) Ag_2O, (d) Ag_IMP, (e) Ag_CR, and (f) Ag_PD.

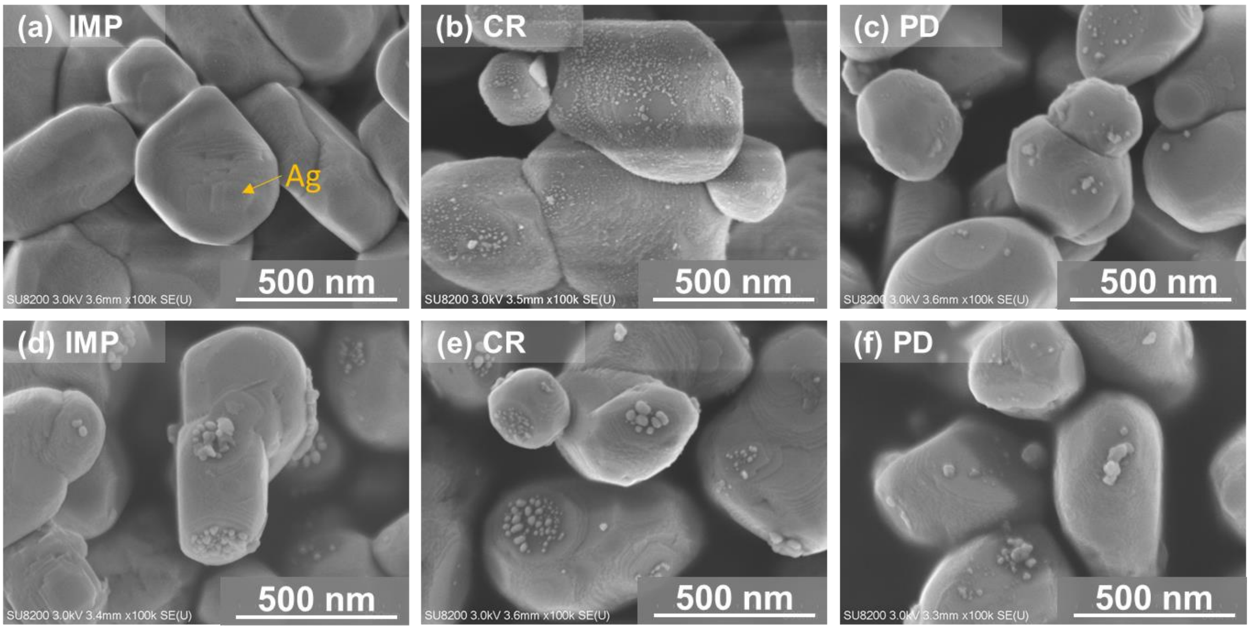

Figure 11. SEM images of cocatalyst-loaded Al–SrTiO$_3$ before and after 5 h photocatalytic reaction. (a), (d) Ag/Al–SrTiO$_3$ (IMP method), (b), (e) Ag/Al–SrTiO$_3$ (CR method), and (c), (f) Ag/Al-SrTiO$_3$ (PD method). (a–c) Before reaction and (d–f) after reaction.

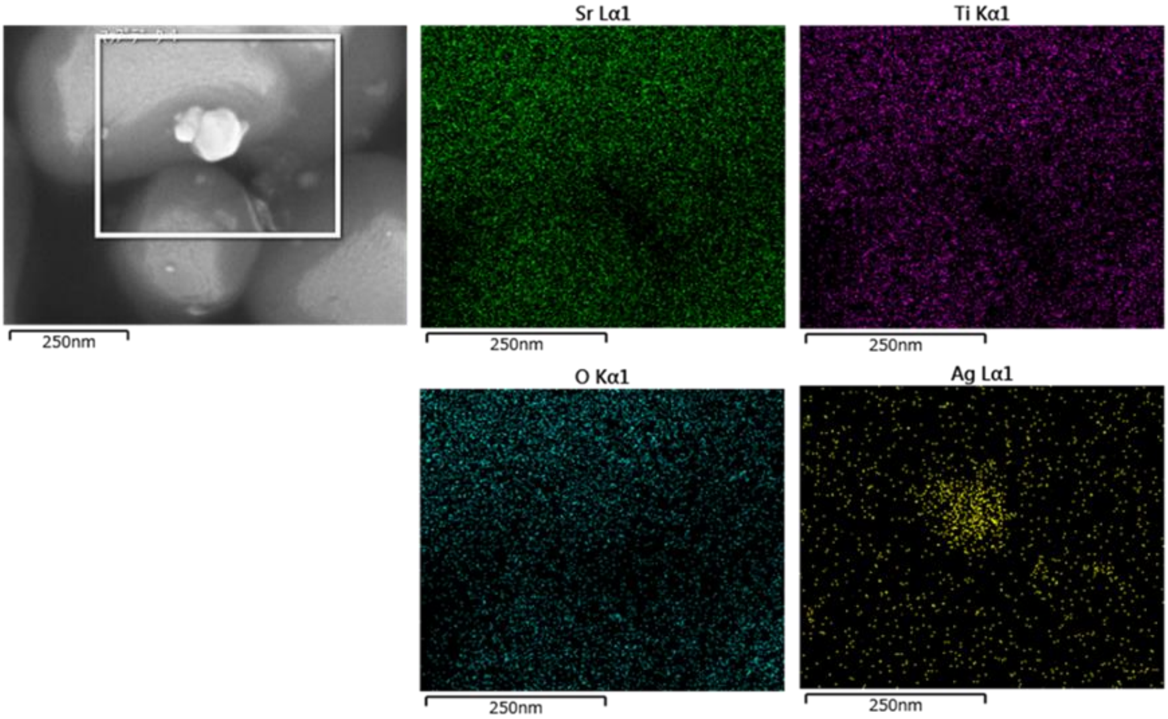

Figure 12. EDS analysis of 1.0 wt.% Ag/Al–SrTiO$_3$ prepared by PD method

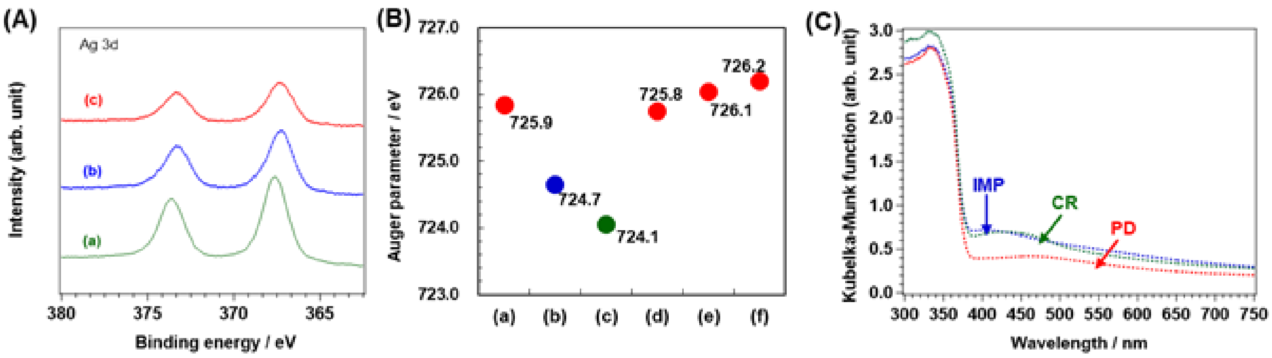

Figure 13. After photocatalytic reaction (A) XPS spectra of Ag 3d (a) Ag_IMP, (b) Ag_CR, and (c) Ag_PD method; (B) Auger parameters of the various Ag species (a) Ag; (b) AgO; (c) Ag2O; and (d) Ag_IMP, (e) Ag_CR, and (f) Ag_PD methods; (C) UV-vis DR spectra of Ag/Al–SrTiO3 fabricated by IMP, CR, and PD methods

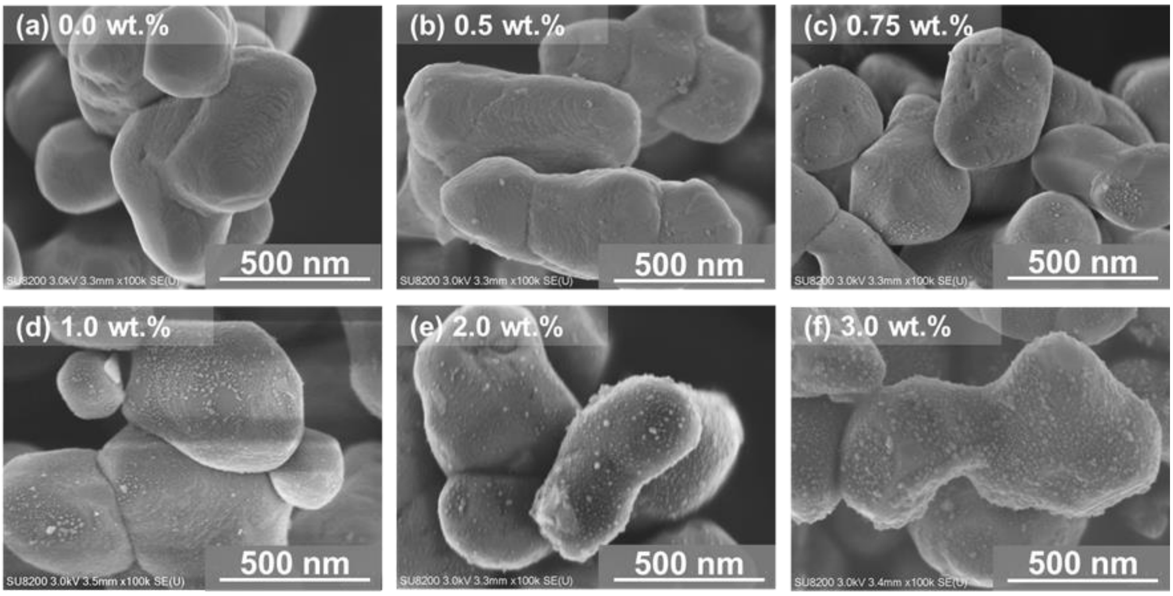

Figure 14. SEM images of the pristine Al–$SrTiO_3$ and the as-prepared Ag loaded Al–$SrTiO_3$ samples: (a) Pristine Al–$SrTiO_3$ (0.0 wt.% Ag); (b) 0.5 wt.% Ag/Al–$SrTiO_3$; (c) 0.75 wt.% Ag/Al–$SrTiO_3$; (d) 1.0 wt.% Ag/Al–$SrTiO_3$; (e) 2.0 wt.% Ag/Al–$SrTiO_3$; and (f) 3.0 wt.% Ag/Al–$SrTiO_3$.

As mentioned earlier, the Ag cocatalyst plays an important role in the photocatalytic conversion of CO_2 into CO with water as an electron donor in aqueous solution.[21, 32, 42] Figure 14 shows SEM images of Al–$SrTiO_3$ samples loaded with Ag (0.0–3.0 wt.%), which were fabricated using the CR method. These images indicate that the Ag cocatalyst nanoparticles were present on the surface of Al–$SrTiO_3$ and gradually became larger with increasing Ag loading. In addition, the surface of the Al–$SrTiO_3$ photocatalyst was almost totally covered with Ag nanoparticles.

Figure 15 shows the rates of formation of H_2, O_2, and CO over Al–$SrTiO_3$ with various loadings of Ag nanoparticles. The pristine Al–$SrTiO_3$ showed very poor photocatalytic activity and low selectivity towards CO evolution. After loading with a small amount of Ag cocatalyst, the selectivity towards CO was dramatically increased to approximately 98.5%, and the CO formation rate was improved with increase in the amount of loaded Ag cocatalyst. When the Ag cocatalyst loading was higher than 1.0 wt.%, the formation rates of all the photocatalytic products were decreased, and the total photocatalytic activity was reduced. The Ag nanoparticle cocatalyst significantly enhanced the CO formation rate by providing effective reduction sites or facilitating charge transfer. [43] [44] On the other hand, different cocatalysts showed different selectivities for the photocatalytic products. In addition, it was confirmed that Ag shows excellent selectivity for CO_2 reduction.[21] [42] Furthermore, anisotropic facets might form on the surface of the Al-$SrTiO_3$ after Al doping because the Ag cocatalyst was only present on the smooth facets after photoirradiation (see Figure 11). Therefore, the charge separation in $SrTiO_3$ should be promoted significantly after Ag modification and Al doping. [32, 36, 45-46] In addition, the *in situ* FT-IR spectra of CO_2 adsorbed species on the surface of $SrTiO_3$ and Al-$SrTiO_3$ samples are shown in Figure 16. The bands corresponding to adsorbed CO_2 were observed at 1217.8 and 1222.6 cm^{-1}(δCOH), 1386.6 and 1413.0 cm^{-1} (ν_{sym}OCO), and 1617 and 1628.8 cm^{-1}(ν_{asym}OCO) and assigned to bicarbonate. [47-50] Furthermore, peaks for bidentate carbonate were observed at 1314.3 and 1335 cm^{-1}.

As shown in Figure 14, the number and sizes of the Ag nanoparticles increased with increase in Ag loading from 0.5 to 3.0 wt.%. When the amount of Ag cocatalyst was lower than 1.0 wt.%, the number of active sites for the reduction of CO_2 linearly increased with increase in the loading of Ag; therefore, the rate of CO formation was enhanced. In contrast, the oversized Ag nanoparticles on the surface of Al–$SrTiO_3$ might block light absorption and cause a decrease in the activity; thus, the photocatalytic reactivity was decreased when the amount of Ag cocatalyst was higher than 1.0 wt.%.

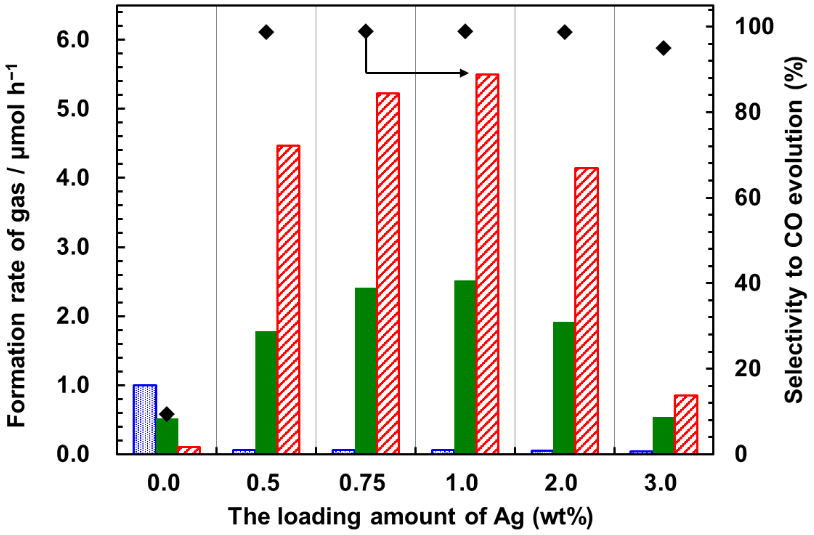

Figure 15. Formation rates of H_2 (blue dotted), O_2 (green filled), and CO (red slashed) for the photocatalytic conversion of CO_2 using H_2O as an electron donor over the 0.0, 0.5, 0.75, 1.0, 2.0, and 3.0 wt.% Ag-cocatalyst-loaded Al–$SrTiO_3$, respectively. Amount of photocatalyst: 0.5 g, volume of reaction solution (H_2O): 1.0 L, additive: 0.1 M $NaHCO_3$, CO_2 flow rate: 30 mL min^{-1}, and light source: 400-W high-pressure Hg lamp with a Pyrex® jacket to cut off light at λ < 300 nm.

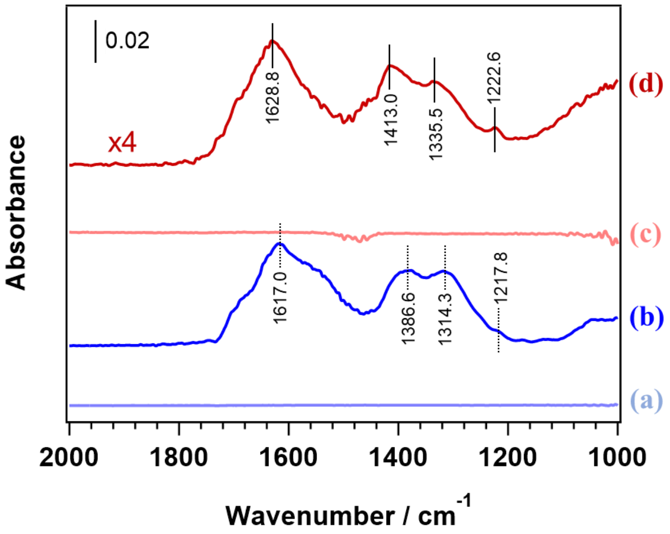

Figure 16. In situ FT-IR spectra over $SrTiO_3$ (a) after pretreatment and (b) in the presence of CO_2 (3.2 kPa); and, Al-$SrTiO_3$ (c) after pretreatment and (d) in the presence of CO_2 (3.2 kPa)

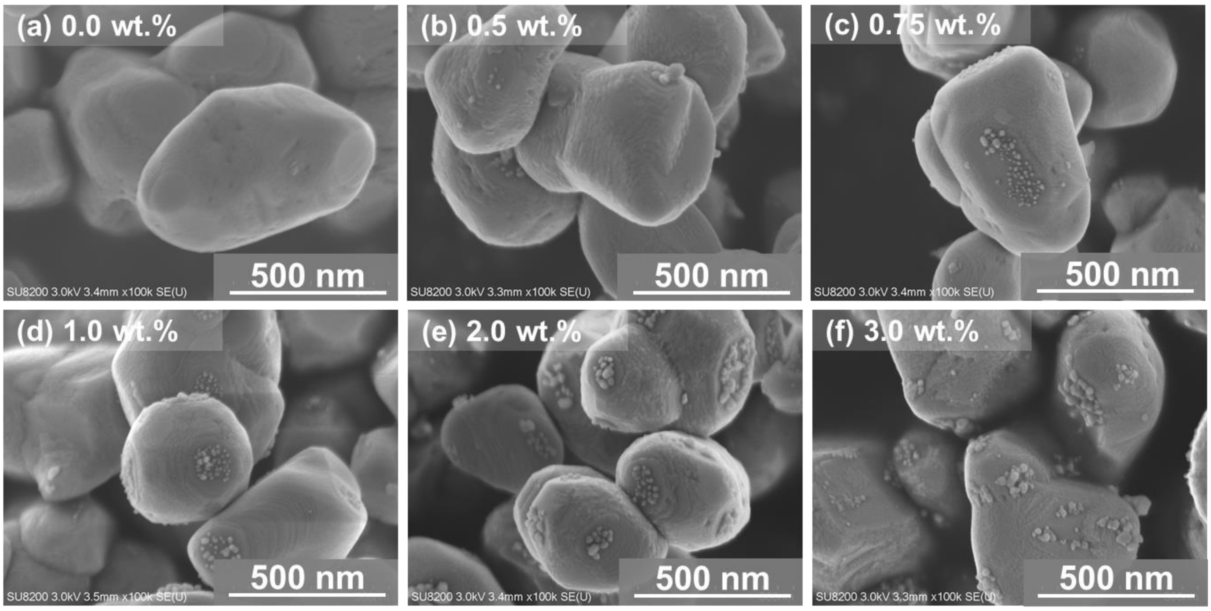

Figure 17. SEM images of the pristine Al–$SrTiO_3$ and the various amount of Ag-loaded Al–$SrTiO_3$ samples after 5 h photocatalytic reaction: (a) Pristine Al–$SrTiO_3$ (0.0-wt.% Ag), (b) 0.5-wt.% Ag/Al–$SrTiO_3$, (c) 0.75-wt.% Ag/Al–$SrTiO_3$, (d) 1.0-wt.% Ag/Al–$SrTiO_3$, (e) 2.0-wt.% Ag/Al–$SrTiO_3$, and (f) 3.0-wt.% Ag/Al–$SrTiO_3$

SEM images of the Ag-loaded Al–$SrTiO_3$ samples were obtained after 5 h of photocatalytic reaction, and the results are shown in Figure 17. The SEM images show that Ag nanoparticles were present on the smooth facets of the samples, and the nanoparticles increased in size as the Ag loading was increased. In particular, although there were significant changes to the size and the microstructure of Ag particles on the Al–$SrTiO_3$ samples, the rate of formation of photocatalytic products remained stable (Figure 8(b)), as did the selectivity for CO evolution. Thus, the Ag/Al–$SrTiO_3$ photocatalysts irradiated for 0.5, 1, and 3 h in aqueous $NaHCO_3$ solution with CO_2 flow were also observed by SEM (Figure 18). After 0.5 h of irradiation, it was found that the morphology of Ag was mostly significantly changed, the Ag cocatalyst particles only existed on the special facets, and the size of the Ag nanoparticles was slightly larger than those before, approximately 10–60 nm; after which, the size and microstructure was maintained until 5 h (Figure 17(d)). Consequently, the chemical state and the microstructure of Ag might be the most important factors affecting the photocatalytic performance

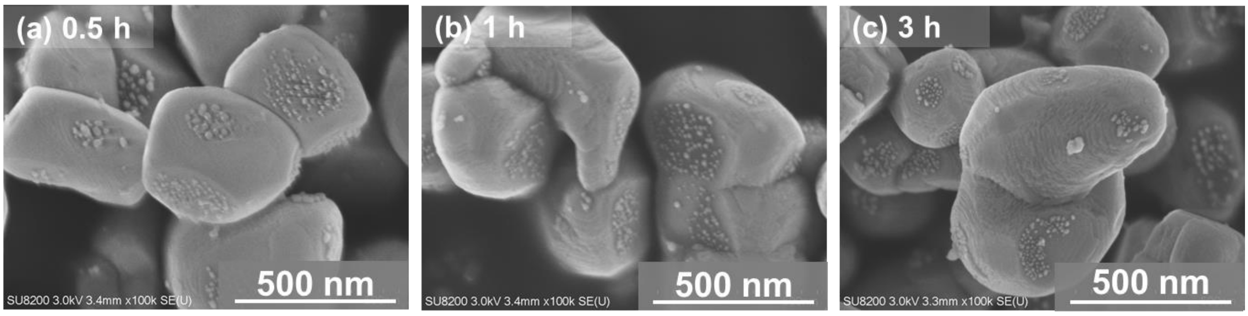

Figure 18. SEM images of the 1.0 wt.% Ag-loaded Al–SrTiO3 after photoirradiation for (a) 0.5, (b) 1, and (c) 3 h.

Conclusion

In the studied photocatalytic system, the activity was found to depend on the degree of Al doping, which was affected by the calcination conditions. Al–$SrTiO_3$, which was fabricated at 1423 K for 15 h, modified with Ag cocatalyst exhibited high activity and selectivity for CO evolution in the photocatalytic conversion of CO_2 using H_2O as an electron donor under photoirradiation at wavelengths greater than 300 nm. Compared with loading via the IMP and PD methods, the loading of Ag using the CR method resulted in a catalyst with an excellent CO formation rate (5.5 μmol h^{-1}) and high selectivity (98.8%) toward CO evolution. Furthermore, the amount of loaded Ag cocatalyst not only affected the size and the number of Ag nanoparticles but also determined the photocatalytic performance of the Ag/Al–$SrTiO_3$ photocatalyst. The results reported here provide a guide for the development of high efficiency photocatalysts for CO_2 reduction under irradiation.

Reference

1. D. Gust; T. A. Moore; A. L. Moore, *Acc. Chem. Res.* **2009**, 42 (12), 1890-1898.
2. T. Zhang; W. Lin, *Chem. Soc. Rev.* **2014**, 43 (16), 5982-5993.
3. S. N. Habisreutinger; L. Schmidt-Mende; J. K. Stolarczyk, *Angew. Chem. Int. Ed.* **2013**, 52, 7372-7408.
4. J. L. White; M. F. Baruch; J. E. Pander III; Y. Hu; I. C. Fortmeyer; J. E. Park; T. Zhang; K. Liao; J. Gu; Y. Yan, *Chem. Rev.* **2015**, 115, 12888-12935.

5. K. Teramura; T. Tanaka, *Phys. Chem. Chem. Phys.* **2018**, 20 (13), 8423-8431.

6. A. J. Morris; G. J. Meyer; E. Fujita, *Acc. Chem. Res.* **2009**, 42 (12), 1983-1994.

7. W. Tu; Y. Zhou; Z. Zou, *Adv. Mater.* **2014**, 26 (27), 4607-4626.

8. M. Halmann, *Nature* **1978**, 275 (5676), 115-116.

9. T. Inoue; A. Fujishima; S. Konishi; K. Honda, *Nature* **1979**, 277 (5698), 637-638.

10. Z. Huang; K. Teramura; S. Hosokawa; T. Tanaka, *Appl. Catal. B* **2016**, 199, 272-281.

11. R. Pang; K. Teramura; H. Asakura; S. Hosokawa; T. Tanaka, *Appl. Catal. B* **2017**, 218, 770-778.

12. R. Pang; K. Teramura; H. Tatsumi; H. Asakura; S. Hosokawa; T. Tanaka, *Chem. Commun.* **2018**, 54 (9), 1053-1056.

13. Z. Wang; K. Teramura; Z. Huang; S. Hosokawa; Y. Sakata; T. Tanaka, *Catal. Sci. & Technol* **2016**, 6, 1025-1032.

14. K. Teramura; H. Tatsumi; Z. Wang; S. Hosokawa; T. Tanaka, *Bull. Chem. Soc. Jpn.* **2015**, 88, 431-437.

15. K. Domen; S. Naito; M. Soma; T. Onishi; K. Tamaru, *J. Chem. Soc., Chem. Commun.* **1980**, (12), 543-544.

16. K. Domen; S. Naito; T. Onishi; K. Tamaru, *Chem. Lett.* **1982**, 11 (4), 555-558.

17. A. Kudo, *J. Phys. Chem. B* **2004**, 108, 8992-8995.

18. M. Ni; M. K. Leung; D. Y. Leung; K. Sumathy, *Renew. Sust. Energ. Rev.* **2007**, 11 (3), 401-425.

19. W. Zhao; W. Ma; C. Chen; J. Zhao; Z. Shuai, *J. Am. Chem. Soc.* **2004**, 126 (15), 4782-4783.

20. T. Ochiai; A. Fujishima, *J. Photochem. Photobiol. C* **2012**, 13 (4), 247-262.

21. K. Iizuka; T. Wato; Y. Miseki; K. Saito; A. Kudo, *J. Am. Chem. Soc.* **2011**, 133 (51), 20863-20868.

22. Z. Wang; K. Teramura; S. Hosokawa; T. Tanaka, *Appl. Catal. B* **2015**, 163, 241-247.

23. X. Zhu; A. Yamamoto; S. Imai; A. Tanaka; H. Kominami; H. Yoshida, *Chem. Commun.* **2019**, 13514-13517.

24. J. Yu; J. Low; W. Xiao; P. Zhou; M. Jaroniec, *J. Am. Chem. Soc.* **2014**, 136, 8839-8842.

25. H. Abdullah; M. M. R. Khan; H. R. Ong; Z. Yaakob, *J. CO_2 Util.* **2017**, 22, 15-32.

26. A. Anzai; N. Fukuo; A. Yamamoto; H. Yoshida, *Catal. Commun.* **2017**, 100, 134-138.

27. C. A. Gueymard, *Solar energy* **2004**, 76 (4), 423-453.

28. Y. Ham; T. Hisatomi; Y. Goto; Y. Moriya; Y. Sakata; A. Yamakata; J. Kubota; K. Domen, *J. Mater. Chem. A* **2016**, 4, 3027-3033.

29. T. H. Chiang; H. Lyu; T. Hisatomi; Y. Goto; T. Takata; M. Katayama; T. Minegishi; K. Domen, *ACS Catal.* **2018**, 8, 2782-2788.

30. Z. Wang; K. Teramura; S. Hosokawa; T. Tanaka, *J. Mater. Chem. A* **2015**, 3, 11313-11319.

31. M. Okazaki; M. Eguchi; T. Uchiyama; D. Lu; H. Kato; Y. Uchimoto; M. Kakihana; K. Maeda, *Dalton Trans.* **2017**, 46, 16959-16966.

32. H. Nakanishi; K. Iizuka; T. Takayama; A. Iwase; A. Kudo, *ChemSusChem* **2017**, 10 (1), 112-118.

33. S. Iguchi; K. Teramura; S. Hosokawa; T. Tanaka, *Catal. Sci. Technol.* **2016**, 6 (13), 4978-4985.

34. Z. Huang; S. Yoshizawa; K. Teramura; H. Asakura; S. Hosokawa; T. Tanaka, *ACS Sustain. Chem. Eng.* **2018**, 6, 8247-8255.

35. S. Wang; K. Teramura; T. Hisatomi; K. Domen; H. Asakura; S. Hosokawa; T. Tanaka, *ACS Appl. Energy Mater.* **2020**, 3, 1468-1475.

36. A. Iwase; H. Kato; A. Kudo, *ChemSusChem* **2009**, 2, 873-877.

37. C. Wagner, *Faraday Discussions of the Chemical Society* **1975**, 60, 291-300.

38. M. C. Biesinger; L. W. Lau; A. R. Gerson; R. S. C. Smart, *Phys. Chem. Chem. Phys.* **2012**, 14 (7), 2434-2442.

39. W. Li; X. Liu; H. Cui; S. Huang; X. Hao, *J. Alloys Compd.* **2015**, 625, 277-283.

40. https://srdata.nist.gov/xps/EngElmSrchQuery.aspx?EType=AP&CSOpt=Retri_ex_dat&Elm=Ag.

41. K.-H. Chen; Y.-C. Pu; K.-D. Chang; Y.-F. Liang; C.-M. Liu; J.-W. Yeh; H.-C. Shih; Y.-J. Hsu, *J. Phys. Chem. C.* **2012**, 116 (35), 19039-19045.

42. J. Ran; M. Jaroniec; S. Z. Qiao, *Adv. Mater.* **2018**, 30 (7), 1704649.

43. J. Yang; H. Yan; X. Wang; F. Wen; Z. Wang; D. Fan; J. Shi; C. Li, *J. Catal.* **2012**, 290,

151-157.

44. J. Yang; D. Wang; H. Han; C. Li, *Acc. Chem. Res.* **2013**, 46 (8), 1900-1909.

45. L. C. Mu; Y. Zhao; A. L. Li; S. Y. Wang; Z. L. Wang; J. X. Yang; Y. Wang; T. F. Liu; R. T. Chen; J. Zhu; F. T. Fan; R. G. Li; C. Li, *Energy Environ. Sci.* **2016**, 9, 2463-2469.

46. T. Takata; J. Jiang; Y. Sakata; M. Nakabayashi; N. Shibata; V. Nandal; K. Seki; T. Hisatomi; K. Domen, *Nature* **2020**, 581 (7809), 411-414.

47. J. R. Copeland; I. A. Santillan; S. M. Schimming; J. L. Ewbank; C. Sievers, *J.Phys. Chem. C* **2013**, 117 (41), 21413-21425.

48. G. S. Foo; Z. D. Hood; Z. Wu, *ACS Catal.* **2018**, 8 (1), 555-565.

49. I. V. Chernyshova; P. Somasundaran; S. Ponnurangam, *Proc. Nat. Acad. Sci.* **2018**, 115 (40), E9261-E9270.

50. H. Tsuneoka; K. Teramura; T. Shishido; T. Tanaka, *J. Phys. Chem. C* **2010**, 114 (19), 8892-8898.

Chapter 2

Effective Driving of Ag-Loaded and Al-Doped $SrTiO_3$ under Irradiation at λ >300 nm for the Photocatalytic Conversion of CO_2 by H_2O

Abstract

Al-doped strontium titanite (Al−$SrTiO_3$) containing numerous stepwise edges on the surface was found to exhibit an excellent performance in the photocatalytic conversion of CO_2 by H_2O as an electron donor under photoirradiation at >300 nm with Ag modification, while in contrast, the Ag-loaded pristine $SrTiO_3$ was inactive as a photocatalyst for this reaction. CO was stably evolved as the main reduction product at a rate of 7.2 μmol h^{-1} over the Ag-loaded Al−$SrTiO_3$, and a small amount of H_2 was generated during the three runs. The selectivity of electrons generated by charge transfer toward CO evolution was ∼98.0%. In addition, the stoichiometric formation of O_2 was observed, indicating that H_2O acts as an electron donor for the reduction of CO_2. Furthermore, isotopic experiments performed using $^{13}CO_2$ revealed that the CO product is derived from CO_2 bubbled into an aqueous solution of $NaHCO_3$ and not from residual carbon species on the catalyst surface.

Introduction

The emission of CO_2 as a greenhouse gas is one of the most predominant causes of global warming, [1-2] which is known to result in climate change, sea surface elevation, and species extinction. [3-5] To address the issues caused by CO_2, artificial photosynthesis, which is the photocatalytic conversion of CO_2 into chemicals such as carbon monoxide (CO), formic acid (HCOOH), methanol (CH_3OH), methane (CH_4), and other organic chemicals, has been reported to exhibit potential in terms of optimizing the energy structure and achieving energy recycling. [2, 6-18] As such, numerous studies have focused on the development and design of novel photocatalysts for the reduction of CO_2, where electron donors such as sacrificial reagents are required due to the redox nature of the photocatalytic reaction. [6–16, 19] For example, water (H_2O) is the most attractive electron donor due to its substantial reserves on earth, relative cheapness, and nontoxicity. Indeed, the group of Kyoto University has reported that Ag-loaded $ZnGa_2O_4/Ga_2O_3$, [8] $ZnGa_2O_4$, [9] $LaTi_2O_7$, [10] SrO-modified Ta_2O_5, [11] $ZnTa_2O_6$, [13] $Sr_2KTa_5O_{15}$, [12] and $SrNb_2O_6$ [15] exhibited excellent performances for the photocatalytic conversion of CO_2 using H_2O as an electron donor. However, the evolution of H_2 rather than CO is preferred when H_2O is used as the electron donor, since the redox potential of CO_2/CO (−0.51 V vs NHE, at pH 7) is more negative than that of H^+/H_2 (−0.41 V vs NHE, at pH 7) in an aqueous solution. [6] The selectivity of CO formation ($\boldsymbol{S}_{CO}$ (%)) and the consumed electrons and holes ($\boldsymbol{e^-/h^+}$) for this process can be calculated according to eqs 1 and 2:

$$\boldsymbol{S}_{CO}\ (\%) = 2\boldsymbol{R}_{CO}/(2\boldsymbol{R}_{CO} + 2\boldsymbol{R}_{H2}) \times 100 \qquad (1)$$

$$\boldsymbol{e^-/h^+} = (2\boldsymbol{R}_{CO} + 2\boldsymbol{R}_{H2}) / 4\boldsymbol{R}_{O2} \qquad (2)$$

where $\boldsymbol{R}_{CO}$, $\boldsymbol{R}_{H2}$, and $\boldsymbol{R}_{O2}$ represent the photocatalytic formation rates of CO, H_2, and O_2, respectively. When H_2O serves as an electron donor, the value of the consumed $\boldsymbol{e^-/h^+}$ is equal to 1.

Although many photocatalysts have been widely investigated for the photocatalytic conversion of CO_2, the discovery of highly efficient photocatalysts is still necessary. In this context, the use of doping metal cations has been widely investigated to enhance photocatalytic activities by improving the physical and chemical properties of catalysts. [16, 20-30] For example, dopants can modify the energy band position through the formation of a new energy level in the photocatalyst, [16, 20, 26] or changes in the photocatalyst morphological structure can take place to increase the rate of photogenerated electron pairs. [24, 30-31] It is also known that the particle size and morphological structure of semiconductor photocatalysts can affect their photocatalytic properties in the photocatalytic reaction occurring on the surface. [19, 31-35] The design and development of a suitably shaped material is therefore necessary to improve the photocatalytic properties. As such, perovskite-based semiconductors have been considered attractive host materials because of their layered structures and the wide variety of available perovskite compounds. [30, 36-37] More specifically, Kudo et al. found that $NaTaO_3$ with a perovskite structure exhibits a particularly high activity in the overall splitting of water into H_2 and O_2. [38-40] Furthermore, the formation of nanometer-scale steps on the surface of $NaTaO_3$ was reported after the doping of lanthanum and alkaline earth metal ions, resulting in improved photocatalytic activities for the water splitting reaction. [30-31] In addition to the surface structure, the particle size of the photocatalysts was also affected by the dopants and dopant impurities, which in turn could affect crystal growth. [24, 28, 41] Moreover, Jonathan et al. proposed a theoretical model to describe the relationship between the photoreactivity, the doping ratio, and the particle size. [28] It was revealed that the particle diameter decreased upon increasing the doping ratio. In addition, Domen et al. reported that the doping of Al into $SrTiO_3$ photocatalysts gave rise to the desirable properties of the perovskite photocatalysts and enhanced the photocatalytic activity. [24] Furthermore, the particle size of $SrTiO_3$ significantly increased upon decreasing the doping degree of Al after flux treatment at high temperatures. It was also found that Al-doped $SrTiO_3$, which was loaded with suitable cocatalysts such as $Rh_{2-y}Cr_yO_3$ and $MoO_y/RhCrO_x$, exhibited a promising photocatalytic activity for overall water splitting under photoirradiation at $\lambda > 300$ nm; [21, 24] the apparent quantum efficiency of the $MoO_y/RhCrO_x$ loaded and Al−doped $SrTiO_3$ reached close to 69% at 365 nm.

Thus, the author herein describes her investigation into the photoreduction of CO_2 by H_2O under photoirradiation using an Al-doped $SrTiO_3$ photocatalyst with an Ag cocatalyst to effectively reduce CO_2 into CO at $\lambda > 300$ nm. The presence of Al dopants on the surface layer of the $SrTiO_3$ particles will be investigated, and the size of the Al-$SrTiO_3$ particles will be compared to those of the flux-treated $SrTiO_3$ in the absence of Al to determine the effect of the doped metal cations on particle growth.

Experimental

Preparation of the Al-doped $SrTiO_3$

Al-doped $SrTiO_3$ photocatalysts were fabricated via a flux method using anhydrous $SrCl_2$ as the flux reagent. [24] More specifically, a mixture of $SrTiO_3$ (99.9%, Wako, Japan), Al_2O_3 (<50 nm particle size, Sigma-Aldrich, Germany), and anhydrous $SrCl_2$ (98.0%, Kanto Chemical Co., Inc., Japan) were added to an alumina mortar and ground for 10 min. The molar ratio of $SrCl_2$:$SrTiO_3$ was fixed at 10.0. The ground mixture was then transferred into an alumina crucible and calcined at 1423 K under air for 15 h. Various Al-doped $SrTiO_3$ species were prepared by adjusting the molar ratio of Al_2O_3 to $SrTiO_3$ in the mixture, and these samples were termed as *x* mol% Al−$SrTiO_3$, where *x* represents the molar ratio of Al to Ti, i.e., 0, 2, 4, or 16. For comparison, bare $SrTiO_3$ photocatalysts without Al doping were also calcined using the flux reagent in an yttria crucible (i.e., 0 mol% $SrTiO_3$-Y).

Loading of the cocatalyst

An Ag cocatalyst was employed to modify the surface of the as-prepared Al−$SrTiO_3$ photocatalyst via a chemical reduction method. More specifically, Al-$SrTiO_3$ (0.75 g) was dispersed in deionized ultrapure water (50 mL), and a 0.1 M aqueous solution of $AgNO_3$ (0.695 mL) and a 0.4 M aqueous solution of NaH_2PO_2 (0.75 mL) were added to the suspension. After the suspension was maintained at a constant temperature of 353 K for 1.5 h, it was filtered and then dried under air at 298 K overnight.

Characterization

The structure and crystalline nature of the prepared Al−$SrTiO_3$ were characterized by X-ray diffraction (XRD) using a Rigaku Ultima IV powder diffractometer equipped with a Cu Kα (λ = 0.154056 nm) radiation source, and using a voltage and current of 40 kV and 40 mA, respectively. UV-vis diffuse reflectance spectroscopy (UV-vis DRS) was performed using a JASCO V-670 spectrometer equipped with an integrating sphere. Spectralon®, which was supplied by Labsphere Inc., was used as a standard reflection sample. Scanning electron microscopy (SEM) images were obtained using a field-emission scanning electron microscope (SU-8220, Hitachi High-Technologies) equipped with an energy dispersive X-ray spectroscopy (EDS) unit at an acceleration voltage of 15.0 kV. The Brunauer–Emmett–Teller (BET) surface area was measured by N_2 adsorption at 77 K using a volumetric gas adsorption apparatus (BELmini, Bel Japan, Inc.). X-ray photoelectron spectroscopy (XPS) was performed by using an X-ray photoelectron spectrometer (ESCA 3400, Shimadzu Corp.), and the chemical concentrations of the various atoms at various points among the depth profiles were observed via Ar ion sputtering (Emission 10 mA; Accel HT: 0.5 kV). Inductively coupled plasma optical emission spectrometry (ICP-OES, iCAP7400, Thermo Fisher Scientific, Inc.) was used to determine the metal compositions in the Al−$SrTiO_3$.

Photocatalytic reaction

The photocatalytic conversion of CO_2 by H_2O was performed in a CO_2 flowing batch system with an inner-irradiation-type reaction vessel at 25°C and under ambient pressure. Ag-loaded Al−$SrTiO_3$ (0.5 g) was dispersed in a 0.1 M aqueous solution of $NaHCO_3$ (1.0 L), and CO_2 gas (99.999%) was bubbled into the suspension at a flow rate of 30 mL min^{-1}. The suspension was then irradiated using a 400 W high-pressure Hg lamp with a Pyrex® jacket connected to a water-cooling system to cut off any light with a wavelength of <300 nm. The gaseous products evolved from the photoreaction system (e.g., H_2, O_2, and CO) were detected by thermal conductivity detector−gas chromatography (TCD-GC) using a GC-8A chromatograph (Shimadzu Corp.) equipped with a 5 Å molecular sieve column with Ar as the carrier gas and by flame ionization detector−gas chromatography (FID-GC) using a methanizer and a ShinCarbon ST column with N_2 as the carrier gas. In the isotope-labeling experiment, $^{12}CO_2$ gas was replaced by $^{13}CO_2$. The formation of ^{13}CO and ^{12}CO under photoirradiation was analyzed by using a quadrupole-type mass spectrometer (BEL Japan, Inc., BEL Mass) combined with TCD-GC using Ar as the carrier gas.

Results and discussion

The author initially examined the effect of varying the quantity of the Al precursor, and so 0 (0 mol% Al vs Ti), 2, 4, and 16 mol% Al−doped $SrTiO_3$ samples were fabricated via a flux method in an alumina crucible. The 0 mol% Al−doped $SrTiO_3$ sample (0 mol% $SrTiO_3$−Y) was also obtained via calcining $SrTiO_3$ and flux $SrCl_2$ in an yttria crucible in the absence of Al_2O_3 to avoid any influence from Al present in the crucible material. The crystal structures of the pristine $SrTiO_3$ and the various prepared Al−$SrTiO_3$ species were measured by using XRD, as shown in Figure 1(A), where all diffraction peaks could be assigned to the pure phase of $SrTiO_3$ with a *Pm*-3*m* (211) space group (ICSD 23076). No peaks were observed corresponding to Al species (Figure 1(A)), and the XRD peaks shifted to the higher energy slightly (Figure 1(B)), thereby indicating that Al is highly dispersed within the $SrTiO_3$ bulk. It is known that the ionic radius of the six-coordinated Ti^{4+} (0.605 Å) is slightly larger than that of Al^{3+} (0.535 Å), [42] and so when Al^{3+} ions replace the Ti^{4+} ions present at the B sites of the perovskite structure, the Bragg equation states that the diffraction pattern should shift to higher angles. The small shift observed in Figure 1(B) therefore appears to confirm that the Al^{3+} ions occupied the B sites of the $SrTiO_3$ perovskite. In addition, as shown in Figure 1(C), the lattice spacing of the (110) plane decreases linearly upon increasing the amount of Al species from 0 to 2.16 mol%, as determined by ICP-OES (Table 1), indicating that almost all Al species were doped into the catalyst. However, the lattice spacing of the (110) plane at an Al content of 4.59 mol% did not exhibit a linear tendency, indicating that only some of the Al species were doped into the catalyst. It is likely that the excess Al was present on the surface of the catalyst. [43-44] The ICP-OES analysis suggested that the pristine $SrTiO_3$, 0 mol% $SrTiO_3$−Y, and 0 mol% Al−$SrTiO_3$ also contained 0.63, 0.68, and 1.50% Al, respectively (Table 1). Nevertheless, no obvious peaks for Al 2p were detected in the case of the pristine $SrTiO_3$ or the 0 mol% $SrTiO_3$−Y samples, as shown in Figure 2. Thus, the tiny amount of Al detected at <0.7% can be attributed to the background level during ICP-OES measurements. The XPS Y 3d spectrum for the 0 mol% $SrTiO_3$−Y sample is given in Figure 2(d).

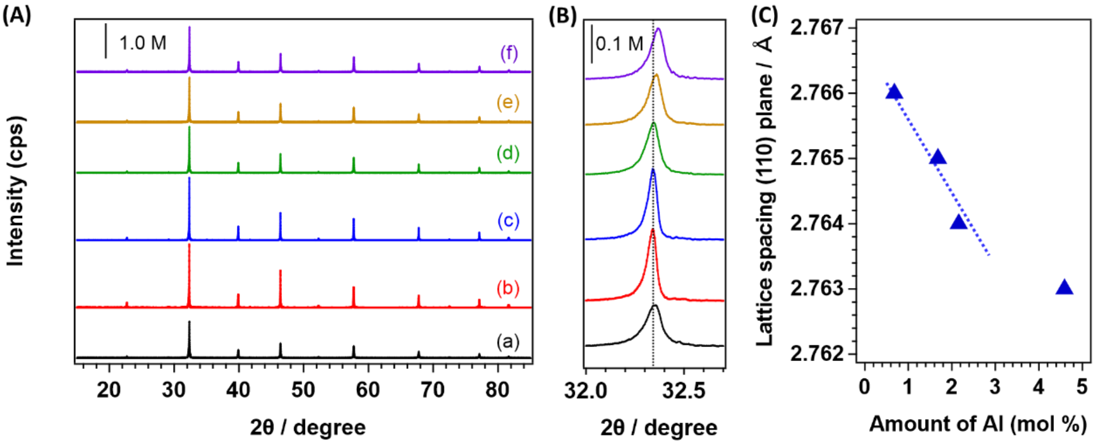

Figure 1. XRD patterns of the pristine $SrTiO_3$ and the various Al−$SrTiO_3$ species: (A) and (B) (a) pristine $SrTiO_3$; (b) 0 mol% $SrTiO_3$−Y; (c) 0 mol% Al-$SrTiO_3$; (d) 2 mol% Al−$SrTiO_3$; (e) 4 mol%

Al-SrTiO$_3$; and (f) 16 mol% Al−SrTiO$_3$. (C) Relationship between the amount of Al (Al/(Al+Ti) as detected by ICP-OES, 0 mol% SrTiO$_3$−Y (0.68), 2 mol% Al−SrTiO$_3$ (1.68), 4 mol% Al-SrTiO$_3$ (2.16), and 16 mol% Al−SrTiO$_3$ (4.59) and the shift in the lattice spacing of the (110) plane at ~32.3°.

Table 1. BET surface area, FWHM of the {110} diffraction peak, Molar ratio, determined by ICP-OES

Various kinds of catalyst	BET/m^2 g^{-1}	FMHW	Al / Ti*100 (experiment) (%)	Al/(Al+Ti)*100 (ICP-OES) (%)
Pristine SrTiO$_3$	3.7	0.105		0.63
0 mol % SrTiO$_3$-Y	1.1	0.057	0	0.68
0 mol % Al-SrTiO$_3$	1.8	0.053	0	1.50
2 mol% Al-SrTiO$_3$	4.1	0.087	2	1.68
4 mol% Al-SrTiO$_3$	4.5	0.087	4	2.16
16 mol% Al-SrTiO$_3$	4.1	0.087	16	4.59

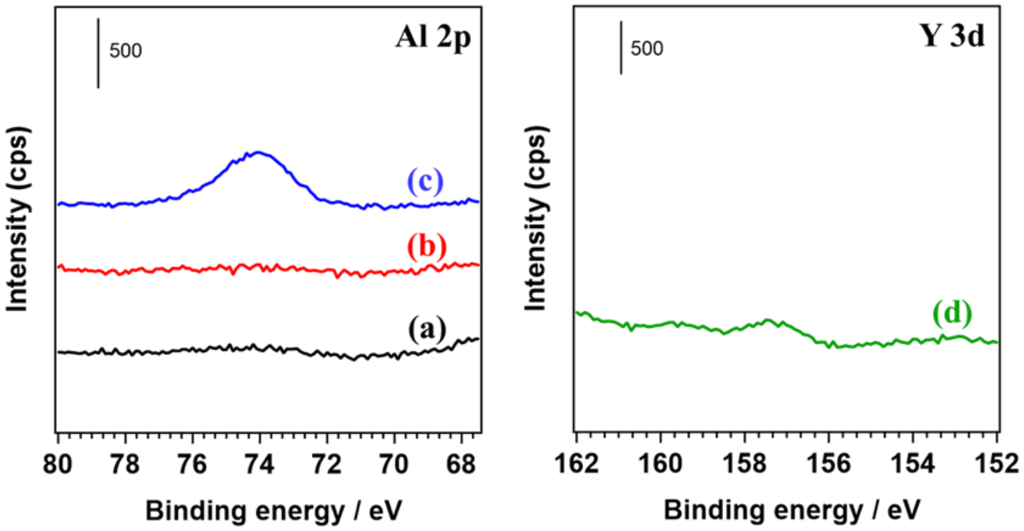

Figure 2. XPS Al 2p for (a) pristine SrTiO$_3$; (b) 0 mol% SrTiO$_3$-Y; (c) 0 mol% Al-SrTiO$_3$; (d) the XPS Y3d for the 0 mol% SrTiO$_3$-Y.

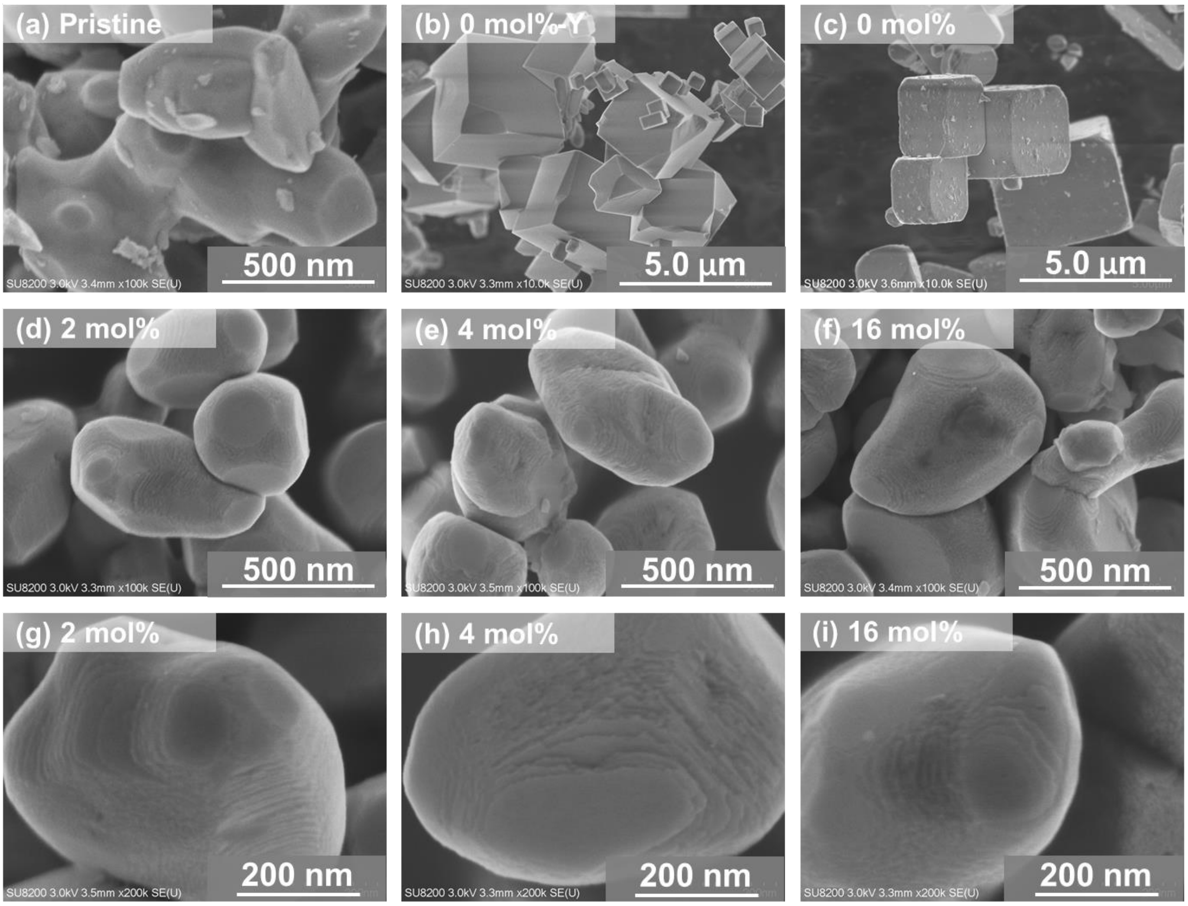

Figure 3. SEM images of the pristine $SrTiO_3$ and the as as-prepared Al−$SrTiO_3$ samples: (a) pristine $SrTiO_3$, (b) 0 mol% $SrTiO_3$−Y, (c) 0 mol% Al−$SrTiO_3$, (d, g) 2 mol% Al−$SrTiO_3$, (e, h) 4 mol% Al−$SrTiO_3$, and (f, i) 16 mol% Al−$SrTiO_3$.

Figure 3 shows the SEM images of the pristine $SrTiO_3$, the 0 mol% $SrTiO_3$−Y, and the 0, 2, 4, and 16 mol% Al−doped $SrTiO_3$ fabricated via the flux method in an alumina crucible. As shown in Figure 3(a), a formless microstructure was observed for the pristine $SrTiO_3$, and the BET surface area was ~3.7 m^2g^{-1}. In contrast, the 0 mol% $SrTiO_3$−Y and 0 mol% Al−$SrTiO_3$ samples were essentially cubic in structure, with some larger particles being observed than for the pristine $SrTiO_3$. However, several smaller particles were also present (Figures 3(b) and 3(c), see the SEM images in Figure 4 for more details). The author also noted that the surface of 0 mol% Al−$SrTiO_3$ was less smooth than that of 0 mol% $SrTiO_3$−Y, and the BET surface areas of the 0 mol% $SrTiO_3$−Y and 0 mol% Al-$SrTiO_3$ samples were 1.1 and 1.8 m^2g^{-1}, respectively (see Table 1 for further details). In the presence of varying amounts of doped Al, the shapes and sizes of the $SrTiO_3$ catalysts were similar to that of the irregularly-shaped pristine SrTiO$_3$; however, the morphological structure changed, and several smooth facets of the polygonous Al−SrTiO$_3$ bulk were surrounded by numerous nanosteps, as shown in Figures 3(g-i). This observation revealed that Al doping resulted in a decrease in the particle size and an increase in the number of stepwise edges on the samples, which is similar to the case of the alkaline earth metal-doped NaTaO$_3$. [30-31] It should be noted that these nanostep defects may suppress the crystal growth of SrTiO$_3$ during calcination.

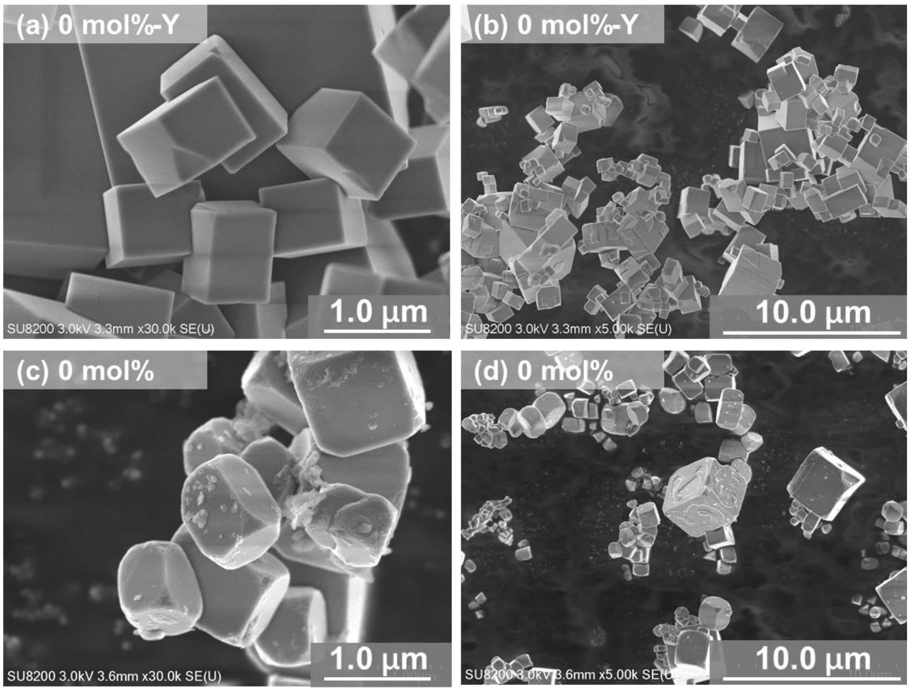

Figure 4. SEM images of (a) and (b) 0 mol% SrTiO$_3$-Y; (c) and (d) 0 mol% Al-SrTiO$_3$

UV-vis DR spectra of various SrTiO$_3$ samples were then collected as shown in Figure 5, and the absorption edges were observed at ~390 nm, which corresponds with previous reports. [22, 24, 45] However, the absorption edges of the flux-treated samples 0 mol% SrTiO$_3$−Y and 0 mol% Al−SrTiO$_3$ shifted slightly to higher wavelengths.

The dependence of Al doping on the photoreduction of CO$_2$ to CO was then examined, as presented in Figure 6. It should be noted that the efficiency of CO evolution increased significantly after the doping of Al into SrTiO$_3$. Interestingly, the formation rates of CO, H$_2$, and O$_2$ over 0 mol% Al−SrTiO$_3$ were significantly higher than those over 0 mol% SrTiO$_3$−Y and over the pristine SrTiO$_3$. It is possible that Al species originating from the alumina crucible may be doped into the SrTiO$_3$

photocatalyst, thereby enhancing the photocatalytic activity for the reduction of CO_2. [24] Indeed, ICP results (as shown in Table 1) suggested that 0 mol% Al-$SrTiO_3$ contains a significantly greater quantity of Al than 0 mol% $SrTiO_3$−Y. It should also be noted here that 0 mol% Al−$SrTiO_3$ exhibited a significantly lower photocatalytic activity than 2 mol% Al−$SrTiO_3$, despite 0 mol% Al−$SrTiO_3$ containing a significant amount of Al. This could be attributed to the particle size of 0 mol%Al−$SrTiO_3$ being larger than that of the other Al-$SrTiO_3$ species, thereby resulting in a lower BET surface area (see Figure 3 and Table 1). On the other hand, numerous nanosteps on the surface of the 2 mol% Al−$SrTiO_3$ formed by the Al doping and the well dispersed Al dopant might have an important impact on the photocatalytic performance of the photocatalyst by promoting the charge separation.[31, 46] Among the various Al-$SrTiO_3$ species, 4 mol% Al-$SrTiO_3$ exhibited the highest rate of CO evolution, at a rate of 7.2 μmol h^{-1}, while the formation rates of H_2 and O_2 were 0.15 and 3.58 μmol h^{-1}, respectively. Moreover, no differences were observed between the XRD patterns of the Ag-loaded Al−doped $SrTiO_3$ after the reaction (Figure 7), thereby suggesting that the crystal structure of Al-$SrTiO_3$ is stable during the photocatalytic reaction. The Ag/Al−$SrTiO_3$ and latest CO_2 reduction photocatalysts that act in aqueous solutions under irradiation are summarized in Figure 2 of the General introduction section of this thesis.

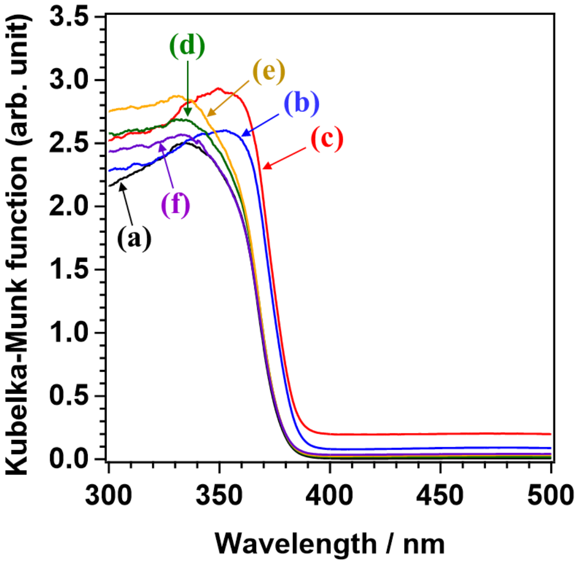

Figure 5. UV-Vis DR spectra of various kinds of $SrTiO_3$: (a) pristine $SrTiO_3$; (b) 0 mol% $SrTiO_3$-Y; (c) 0 mol% Al-$SrTiO_3$; (d) 2 mol% Al-$SrTiO_3$; (e) 4 mol% Al-$SrTiO_3$; and (f) 16 mol% Al-$SrTiO_3$.

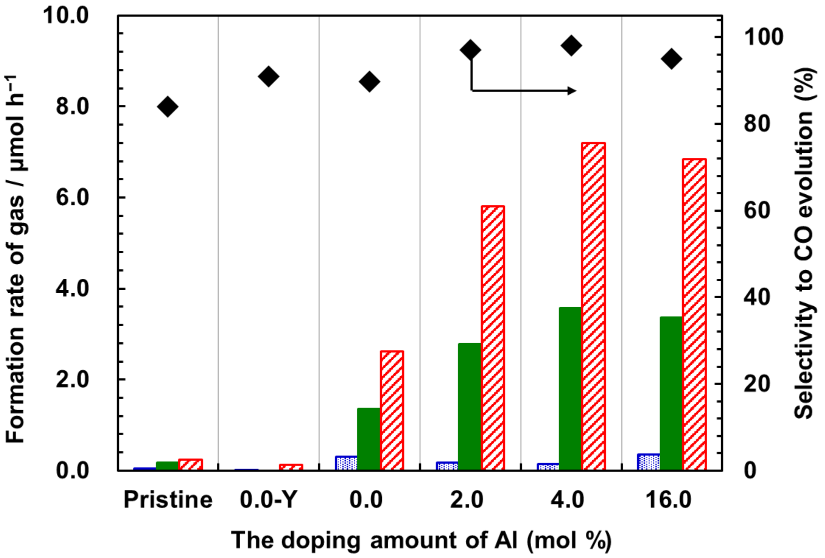

Figure 6. Formation rates of H_2 (blue dotted), O_2 (green filled), and CO (red slashed) and the selectivity toward CO evolution for the photocatalytic conversion of CO_2 by H_2O over the Ag-loaded pristine $SrTiO_3$, the 0 mol% $SrTiO_3$-Y, and the 0, 2, 4, and 16 mol% Al−$SrTiO_3$ photocatalysts. Amount of photocatalyst: 0.5 g; Ag loading: 1.0 wt%; volume of reaction solution (H_2O): 1.0 L; additive: 0.1 M $NaHCO_3$; CO_2 flow rate: 30 mL min^{-1}; light source: 400 W high-pressure Hg lamp with a Pyrex® jacket to cut off light at $\lambda < 300$ nm.

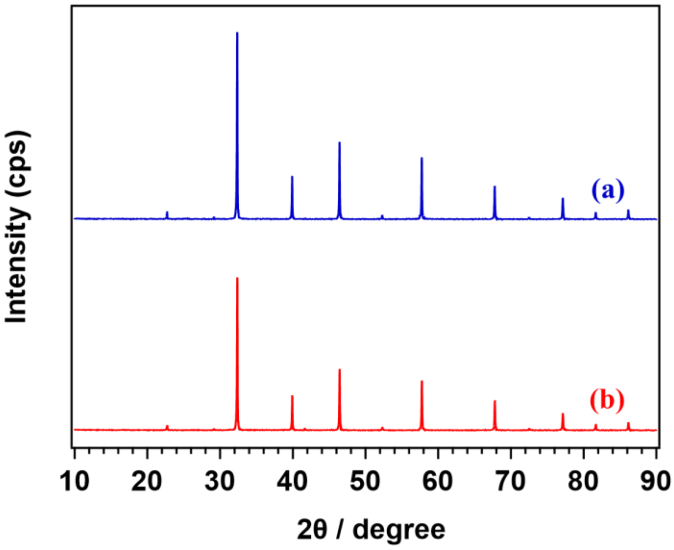

Figure 7. XRD patterns of Ag/Al-$SrTiO_3$ (a) as-prepared, (b) after 5 hours photoreaction.

The above results therefore indicated that Al doping could significantly improve the activity of the photocatalytic conversion of CO_2 by H_2O over Al−$SrTiO_3$ under photoirradiation at $\lambda > 300$ nm. To uncover the underlying cause of the photocatalytic performance enhancement of Al−$SrTiO_3$, it is necessary to investigate the position of Al in the Al−$SrTiO_3$ structure. Noble gas sputtering (5 s bursts) was therefore employed to observe the chemical composition of Al−$SrTiO_3$ at various points among the depth profiles. [47] Thus, Figure 8(a) shows the Al 2p XPS results for the 4 mol% Al−$SrTiO_3$ with various Ar sputtering times. The intensity of the Al 2p peak gradually decreased upon increasing the sputtering time. Normally, the molar ratio of Sr to Ti in the $SrTiO_3$ should be 1:1, and so if Al^{3+} replaces the sites of Ti^{4+}, the ratio of Sr to the total amount of Al and Ti in Al−$SrTiO_3$ should be equal to the value of Sr to Ti in the pristine $SrTiO_3$. The atomic ratios of Sr, Ti, and Al to the total amount of Ti and Al were therefore calculated from the area of the peaks (as shown in Figure 8(b)). It is important to note that at the surface of the pristine $SrTiO_3$, the molar ratio of Sr to Ti is higher than inside the photocatalyst, and the molar ratio becomes stable at ~120% after sputtering for 10 s (see Figure 9 for more details). The value of ***Sr/(Ti+Al)*** before sputtering is lower than after sputtering for 5 s, suggesting that a few Al species existed on the surface as Al_2O_3 or other derivatives. During the initial 25 s of Ar ion sputtering, the atomic concentration of Al decreased sharply, and the concentration of Ti increased. This was followed by the atomic concentrations of Al and Ti gradually becoming stable around 10.0%, which is nearly 4.6 times higher than the Al concentration detected by the ICP-OES. It should be noted that the concentrations of atoms estimated by XPS (as shown in Figure 8) were not perfectly accurate, since they were found to be inconsistent with those observed by ICP-OES. However, it is common in XPS analysis to estimate the ratio of each element, since not all particles are etched in the same proportion, and it is also difficult to employ exact atomic sensitivity factors (ASF). However, the XPS measurements clearly showed the elemental distribution of Al-$SrTiO_3$. The value of Sr to Ti and Al became stable at ~110% after 5 s of Ar ion sputtering. The XPS results therefore suggest that Al species exist on the surface of Al-$SrTiO_3$, although a small quantity of alumina is also present on the catalyst surface, and some of the Al atoms replace the Ti sites in the perovskite structure. In view of the obtained XRD patterns and SEM images, we concluded that when Al atoms replace the Ti sites, several defects are formed on the edges of the perovskite $SrTiO_3$ layers due to the unmatched ionic radii and valence states, which restrict growth of the crystal cell during calcination, thereby resulting in the formation of nanosteps.

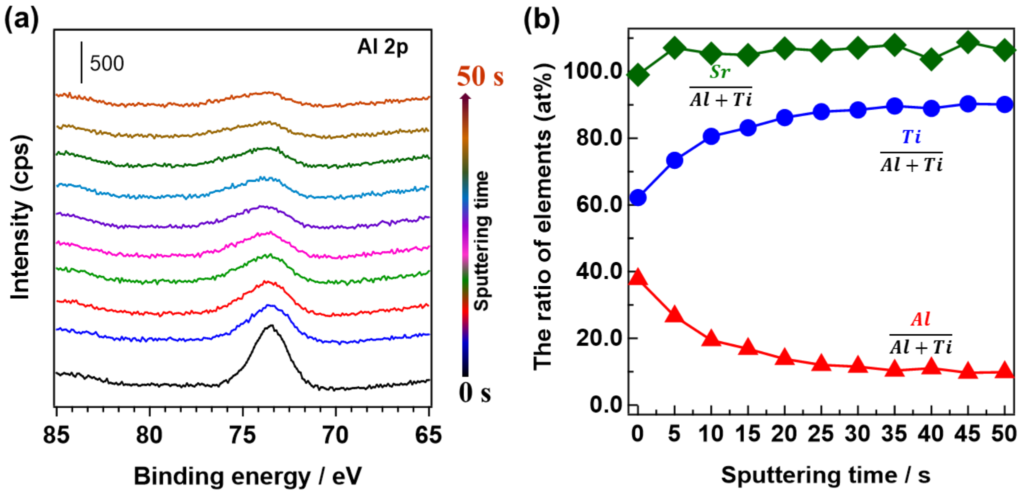

Figure 8. XPS data: (a) Al 2p for 4 mol% Al−$SrTiO_3$ with various Ar sputtering times; (b) 4 mol% Al-$SrTiO_3$, where the atomic ratios of Al, Sr, and Ti to the totals of Ti and Al are indicated.

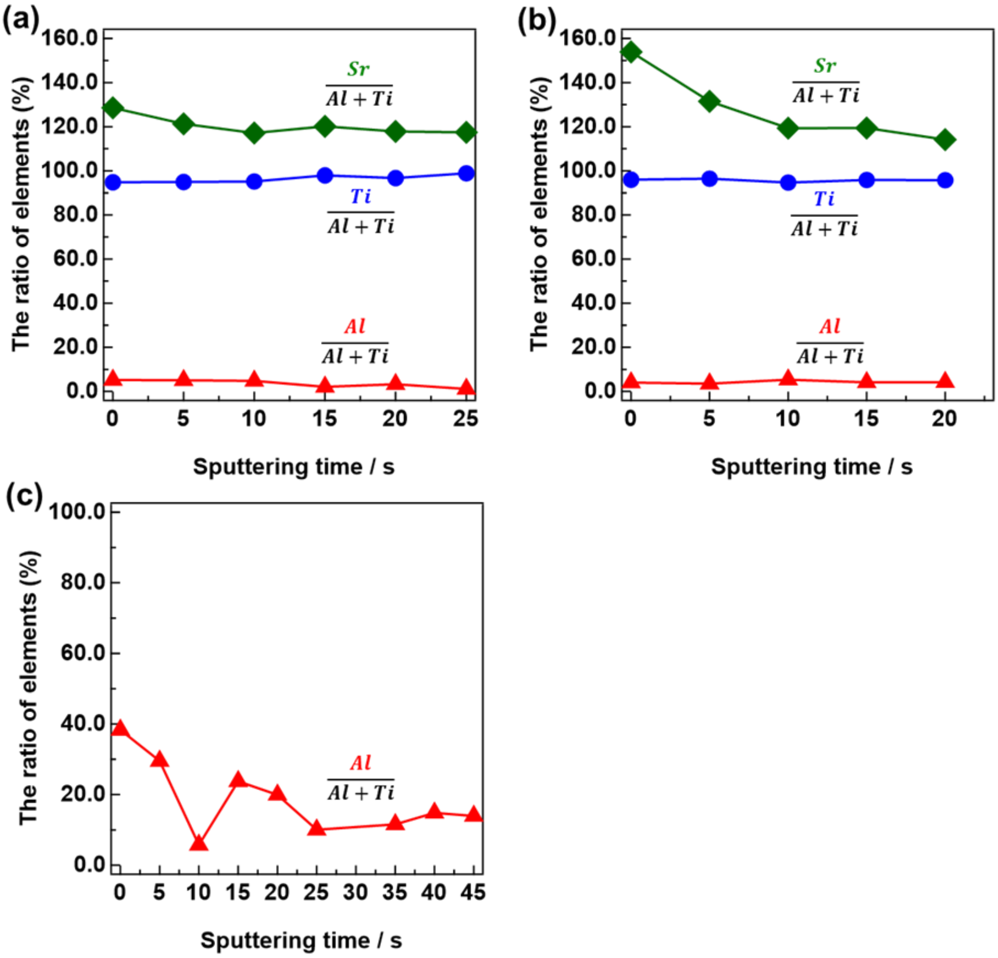

Figure 9. Atom ratio of Al, Sr, Ti elements to the total of Ti and Al; Sr/(Al+Ti), Ti/(Al+Ti), Al/(Al+Ti) (a) pristine $SrTiO_3$; (b) 0 mol% SrTiO3-Y; (c) 0 mol% Al- $SrTiO_3$

Furthermore, it is important to confirm the effect of the reaction conditions on the formation rates of the photocatalytic products. As shown in Figure 10(a), no product evolution was observed in the absence of photoirradiation, and only small quantities of O_2 were detected without a photocatalyst. In the absence of a Ag cocatalyst (Figure 10(c)), the selectivity toward CO evolution was particularly poor (9.5%) and the formation rates of H_2 and O_2 were only 0.99 and 0.51 μmol h^{-1} (Figure 10(c)), respectively. The total photocatalytic activity shown in Figure 10(d) in the absence of the $NaHCO_3$ additive remained low, although the selectivity toward CO evolution was high at 82.2%. The formation rate of CO decreased when using Ar gas instead of bubbling CO_2 gas. In addition, the pH value of the suspension under Ar bubbling increased from 9.14 to 9.22 during the reaction, which was significantly higher than that in the absence of $NaHCO_3$ additives (i.e., 3.55; see Figures 11(a,b)). Moreover, the best photocatalytic performance was observed for the Ag-loaded Al-$SrTiO_3$ with CO_2 bubbling and $NaHCO_3$ addition under irradiation, as the pH value of the suspension was maintained stable at ~6.88 during the reaction (see Figure 11(c)). These can therefore be considered independent factors during the photocatalytic reduction of CO_2 in an aqueous solution. In addition, the stoichiometric formation of O_2 was detected, thereby indicating that H_2O acted as an electron donor.

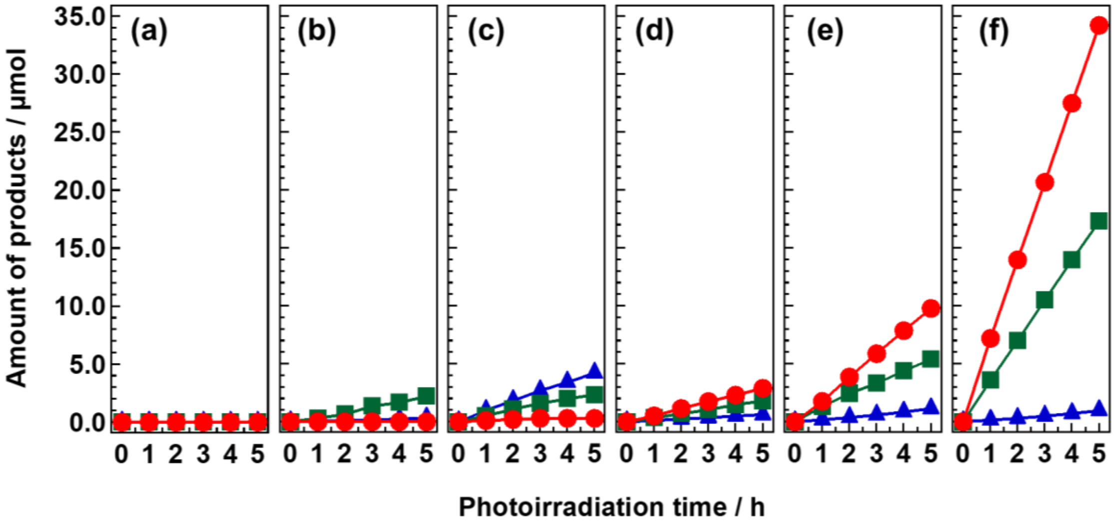

Figure 10. Formation rates of H_2 (blue triangle), O_2 (green square), and CO (red circle) for the photocatalytic conversion of CO_2 by H_2O over 1 wt% Ag-loaded 4 mol% Al−$SrTiO_3$. (a) without irradiation; (b) without catalyst; (c) without cocatalyst; (d) without the $NaHCO_3$ additive; (e) flowing Ar gas, without a CO_2 gas flow; (f) typical conditions. Amount of photocatalyst: 0.5 g; Ag loading:

1.0 wt%; volume of reaction solution (H_2O): 1.0 L; additive: 0.1 M $NaHCO_3$; CO_2 flow rate: 30 mL min^{-1}; light source: 400 W high-pressure Hg lamp with a Pyrex® jacket to cut off light at λ < 300 nm.

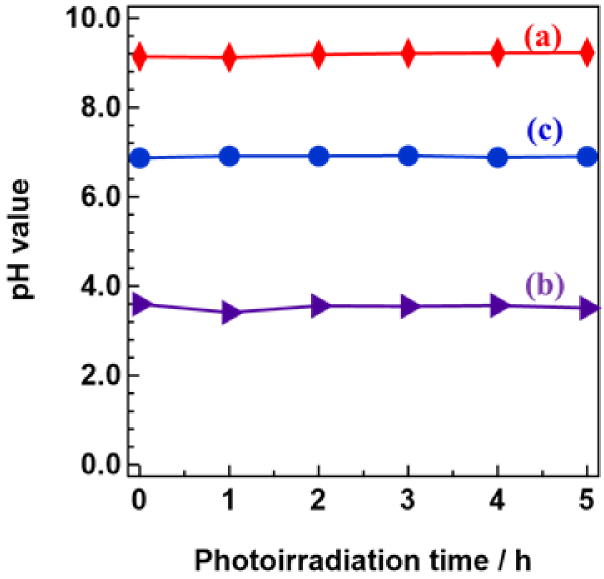

Figure 11. pH value of the suspension solution during the photocatalytic reaction; (a) flowing Ar gas, without a CO_2 gas flow; (b) without the $NaHCO_3$ additive; (c) typical conditions

Stability is one of the most important factors in estimating the properties of photocatalysts. Thus, Figure 12 shows the time-dependent evolution of CO, H_2, and O_2 as products during the photocatalytic reduction of CO_2 by H_2O as an electron donor under photoirradiation conditions. It should be noted that the photocatalysts were vacuum-filtered, washed with ultrapure water, and dried under air at room temperature for every 5 h of photoreaction carried out. The balance of $\boldsymbol{e^-/h^+}$ was found to be ~1.0, which indicates that H_2O successfully functions as an electron donor during the whole reaction. The formation rate of O_2 did not decrease significantly during the reaction, although the formation rate of CO slightly decreased after 15 h. These results suggest that the prepared Ag/Al−$SrTiO_3$ is stable during the photocatalytic reaction. The photocatalytic reduction of CO_2 reaction was also performed over Ag/Al-$SrTiO_3$ on the 1.0 L scale (0.1 M $NaHCO_3$ aq) with constant CO_2 bubbling over 10 h (Figure 13). Thus, after 10 h of the photocatalytic reaction, the selectivity to CO evolution was found to decrease slightly. The SEM images of Ag/Al-$SrTiO_3$ before and after the reaction are shown in Figure 14, where it is apparent that the Ag nanoparticles on Ag/Al-$SrTiO_3$

became aggregated following the photocatalytic reaction.

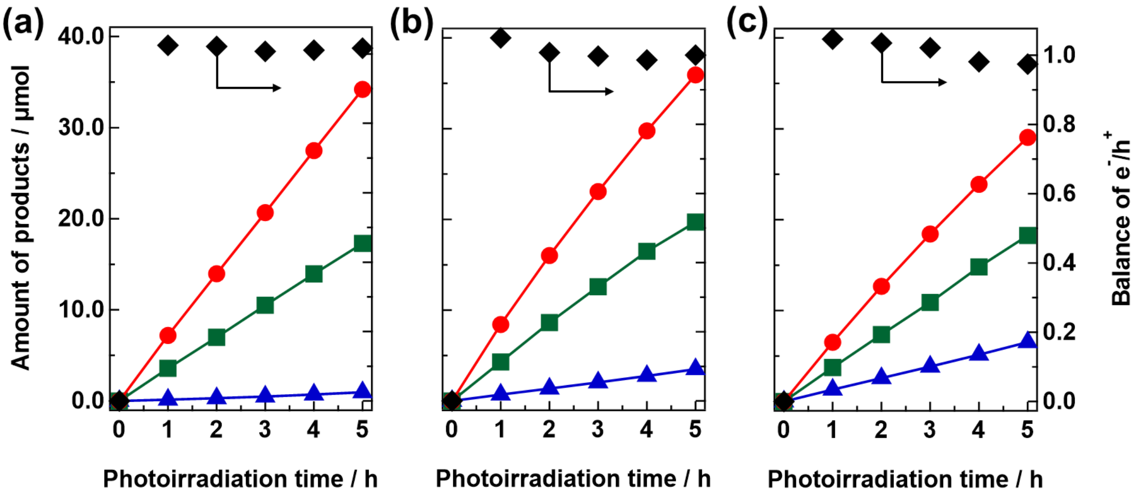

Figure 12. Time-dependent evolution of H_2 (blue triangle), O_2 (green square), and CO (red circle) over 1 wt% Ag-loaded 4 mol% Al-$SrTiO_3$: (a) first run; (b) second run; and (c) third run. Amount of catalyst: 0.5 g; 1 wt% Ag modified by the chemical reduction method; volume of reaction solution: 1.0 L of a 1.0 M $NaHCO_3$ aqueous solution; CO_2 flow rate: 30 mL/min; light source: 400 W high-pressure Hg lamp.

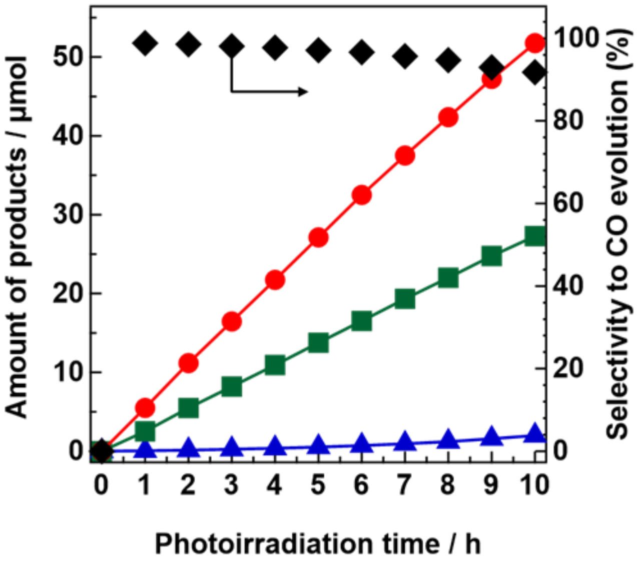

Figure 13. Time-dependent evolution of H_2 (blue triangle), O_2 (green square), CO (red circle), and selectivity to CO evolution (black rhombus) over Ag-loaded Al-$SrTiO_3$ for 10 h without a break.

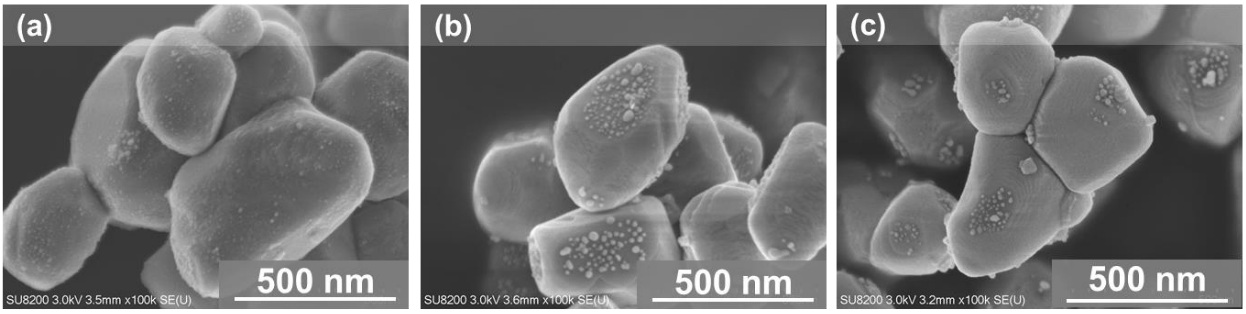

Figure 14. the SEM images of Ag/Al-$SrTiO_3$; (a) before reaction; (b) after 5 h photocatalytic reaction; (c) after 15 h photocatalytic reaction

To confirm that the CO was derived from CO_2 bubbled into the aqueous solution rather than from any organic contaminants present in the photocatalytic reaction system, isotope-labeling experiments were performed using $^{13}CO_2$ over the Ag loaded Al−$SrTiO_3$ photocatalyst. Thus, Figure 15 shows the obtained GC and MS (m/z = 28, 29) results for the reaction, where peaks corresponding to H_2, N_2, O_2, and CO were observed at 2.2, 4.1, 6.1, and 14.2 min in the TCD-GC chromatogram, respectively. In addition, the peak at ~6.0 min in the m/z = 28 spectrum was assigned to N_2 from the air, since the peak position was the same as that monitored by TCD-GC, and no peaks corresponding to ^{12}CO were detected. Moreover, the peak observed in the m/z = 29 spectrum, which was assigned to ^{13}CO gas, appeared at the same retention time as that monitored by TCD-GC. This result indicated that the CO evolved over the Ag-loaded Al-$SrTiO_3$ catalyst was derived from the introduced CO_2 gas.

Conclusion

In summary, the author successfully prepared an Al-doped $SrTiO_3$ perovskite-based photocatalyst using a facile flux method. The subsequently prepared Ag-loaded Al−$SrTiO_3$ was found to exhibit a high selectivity toward CO evolution and a good stability in the conversion of CO_2 into CO using H_2O as an electron donor in aqueous solution under irradiation. The rate of CO formation for this system was 7.2 μmol h^{-1}, and the selectivity toward CO evolution was ~98.0%. Overall, it was found that Al doping into the perovskite-structured catalyst enhanced the photoreduction of CO_2. In addition, with the exception of small quantities of Al_2O_3 on the $SrTiO_3$

surface, the majority of Al was doped on the layered edges of the perovskite structure. After doping, numerous stepwise edge structures were observed on the surface of the Al-doped $SrTiO_3$. These results are of importance as the development of novel catalysts for the photoreduction of the greenhouse gas CO_2 is necessary. Further studies are now required to confirm the role of the Al dopants and to develop a more efficient means to utilize the effect of this doping.

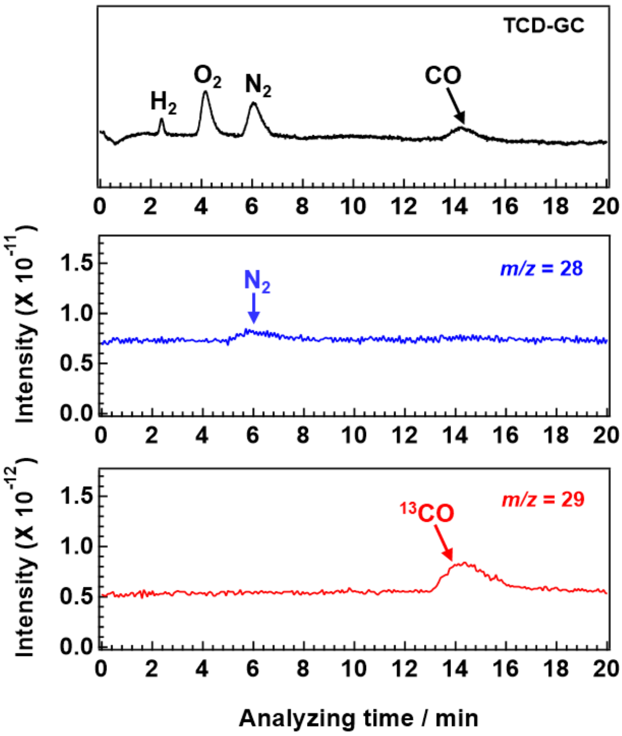

Figure 15. Gas chromatogram and mass spectra (*m/z* 28, 29) for the photocatalytic conversion of $^{13}CO_2$ by water over the Ag-loaded Al−$SrTiO_3$ photocatalyst. Amount of catalyst: 0.5 g; 1 wt% Ag modified by the chemical reduction method; volume of reaction solution: 1.0 L of a 1.0 M $NaHCO_3$ aqueous solution; CO_2 flow rate: 30 mL/min; light source: 400 W high-pressure Hg lamp.

Reference

1. P. M. Cox; R. A. Betts; C. D. Jones; S. A. Spall; I. J. Totterdell, *Nature* **2000**, 408, 750.

2. S. N. Habisreutinger; L. Schmidt-Mende; J. K. Stolarczyk, *Angew. Chem. Int. Ed.* **2013**, 52, 7372-7408.

3. T. P. Dawson; S. T. Jackson; J. I. House; I. C. Prentice; G. M. Mace, *Science* **2011**, 332,

53-58.

4. M. P. McCarthy; M. J. Best; R. A. Betts, *Geophys. Res. Lett.* **2010**, 37, L09705.

5. J. F. Mitchell, *Rev. Geophys.* **1989**, 27, 115-139.

6. J. L. White; M. F. Baruch; J. E. Pander III; Y. Hu; I. C. Fortmeyer; J. E. Park; T. Zhang; K. Liao; J. Gu; Y. Yan, *Chem. Rev.* **2015**, 115, 12888-12935.

7. K. Iizuka; T. Wato; Y. Miseki; K. Saito; A. Kudo, *J. Am. Chem. Soc.* **2011**, 133, 20863-20868.

8. Z. Wang; K. Teramura; Z. Huang; S. Hosokawa; Y. Sakata; T. Tanaka, *Catal. Sci. & Technol* **2016**, 6, 1025-1032.

9. Z. Wang; K. Teramura; S. Hosokawa; T. Tanaka, *J. Mater. Chem. A* **2015**, 3, 11313-11319.

10. Z. Wang; K. Teramura; S. Hosokawa; T. Tanaka, *Appl. Catal. B* **2015**, 163, 241-247.

11. K. Teramura; H. Tatsumi; Z. Wang; S. Hosokawa; T. Tanaka, *Bull. Chem. Soc. Jpn.* **2015**, 88, 431-437.

12. Z. Huang; S. Yoshizawa; K. Teramura; H. Asakura; S. Hosokawa; T. Tanaka, *ACS Omega* **2017**, 2, 8187-8197.

13. S. Iguchi; K. Teramura; S. Hosokawa; T. Tanaka, *Catal. Sci. Technol.* **2016**, 6 (13), 4978-4985.

14. Z. Huang; S. Yoshizawa; K. Teramura; H. Asakura; S. Hosokawa; T. Tanaka, *ACS Sustain. Chem. Eng.* **2018**, 6, 8247-8255.

15. R. Pang; K. Teramura; H. Asakura; S. Hosokawa; T. Tanaka, *Appl. Catal. B* **2017**, 218, 770-778.

16. S. Kikkawa; K. Teramura; H. Asakura; S. Hosokawa; T. Tanaka, *J. Phys. Chem. C* **2018**, 122, 21132-21139.

17. L. Y. Wu; Y. F. Mu; X. X. Guo; W. Zhang; Z. M. Zhang; M. Zhang; T. B. Lu, *Angew.Chem. Int.Ed.* **2019**, 58, 9491-9495.

18. X. Zhu; A. Yamamoto; S. Imai; A. Tanaka; H. Kominami; H. Yoshida, *Chem. Commun.* **2019**, 13514-13517.

19. H. Yoshida; L. Zhang; M. Sato; T. Morikawa; T. Kajino; T. Sekito; S. Matsumoto; H. Hirata, *Catal. Today* **2015**, 251, 132-139.

20. W. Choi; A. Termin; M. R. Hoffmann, *J. Phys. Chem.* **1994**, 98, 13669-13679.

21. T. H. Chiang; H. Lyu; T. Hisatomi; Y. Goto; T. Takata; M. Katayama; T. Minegishi; K. Domen, *ACS Catal.* **2018**, 8, 2782-2788.

22. A. Kudo, *J. Phys. Chem. B* **2004**, 108, 8992-8995.

23. H. Luo; T. Takata; Y. Lee; J. Zhao; K. Domen; Y. Yan, *Chem. Mater.* **2004**, 16, 846-849.

24. Y. Ham; T. Hisatomi; Y. Goto; Y. Moriya; Y. Sakata; A. Yamakata; J. Kubota; K. Domen, *J. Mater. Chem. A* **2016**, 4, 3027-3033.

25. K. Iwashina; A. Kudo, *J. Am. Chem. Soc.* **2011**, 133, 13272-13275.

26. T. Umebayashi; T. Yamaki; H. Itoh; K. Asai, *J. Phys. Chem. Solids* **2002**, 63, 1909-1920.

27. J. Zhang; Y. Wu; M. Xing; S. A. K. Leghari; S. Sajjad, *Energy Environ. Sci.* **2010**, 3, 715-726.

28. J. Z. Bloh; R. Dillert; D. W. Bahnemann, *J. Phys. Chem. C* **2012**, 116, 25558-25562.

29. H. Huang; X. Li; J. Wang; F. Dong; P. K. Chu; T. Zhang; Y. Zhang, *ACS Catal.* **2015**, 5, 4094-4103.

30. H. Kato; K. Asakura; A. Kudo, *J. Am. Chem. Soc.* **2003**, 125, 3082-3089.

31. A. Iwase; H. Kato; A. Kudo, *ChemSusChem* **2009**, 2, 873-877.

32. R. Chen; S. Pang; H. An; J. Zhu; S. Ye; Y. Gao; F. Fan; C. Li, *Nature Energy* **2018**, 3, 655-663.

33. J. Yu; J. Low; W. Xiao; P. Zhou; M. Jaroniec, *J. Am. Chem. Soc.* **2014**, 136, 8839-8842.

34. L. C. Mu; Y. Zhao; A. L. Li; S. Y. Wang; Z. L. Wang; J. X. Yang; Y. Wang; T. F. Liu; R. T. Chen; J. Zhu; F. T. Fan; R. G. Li; C. Li, *Energy Environ. Sci.* **2016**, 9, 2463-2469.

35. H. Kato; M. Kobayashi; M. Hara; M. Kakihana, *Catal. Sci. Technol.* **2013**, 3, 1733-1738.

36. Y. Zhou; J. Chen; O. M. Bakr; H.-T. Sun, *Chem. Mater.* **2018**, 30, 6589-6613.

37. H.-C. Chen; C.-W. Huang; J. C. Wu; S.-T. Lin, *J. Phys. Chem. C* **2012**, 116, 7897-7903.

38. H. Kato; A. Kudo, *Chem. Phys. Lett.* **1998**, 295, 487-492.

39. H. Kato; A. Kudo, *Catal. Lett.* **1999**, 58, 153-155.

40. H. Kato; A. Kudo, *J. Phys. Chem. B* **2001**, 105, 4285-4292.

41. F. Wang; Y. Han; C. S. Lim; Y. Lu; J. Wang; J. Xu; H. Chen; C. Zhang; M. Hong; X. Liu, *Nature* **2010**, 463, 1061-1065.

42. B. R. D. Shannon, *Acta Cryst* **1976**, A32, 751-767.

43. C. Artini; G. A. Costa; M. Pani; A. Lausi; J. Plaisier, *J. Solid State Chem.* **2012**, 190, 24-28.

44. M. J. Lambregts; S. Frank, *Talanta* **2004**, 62, 627-630.

45. M. Okazaki; M. Eguchi; T. Uchiyama; D. Lu; H. Kato; Y. Uchimoto; M. Kakihana; K. Maeda, *Dalton Trans.* **2017**, 46, 16959-16966.

46. H. Nakanishi; K. Iizuka; T. Takayama; A. Iwase; A. Kudo, *ChemSusChem* **2017**, 10 (1), 112-118.

47. T. Hanawa; M. Ota, *App. Surf. Sci.* **1992**, 55, 269-276.

Chapter 3

Dual Ag/Co Cocatalyst Synergism for the Highly Effective Photocatalytic Conversion of CO_2 by H_2O over Al-$SrTiO_3$

Abstract

Loading Ag and Co dual cocatalysts on Al-doped $SrTiO_3$ (AgCo/Al-$SrTiO_3$) led to a significantly improved CO-formation rate and extremely high selectivity toward CO evolution (99.8%) using H2O as an electron donor when irradiated with light at wavelengths above 300 nm. Furthermore, the CO-formation rate over AgCo/Al-$SrTiO_3$ (52.7 μmol h^{-1}) was a dozen times higher than that over Ag/Al-$SrTiO_3$ (4.7 μmol h^{-1}). The apparent quantum efficiency for CO evolution over AgCo/Al-$SrTiO_3$ was about 0.03% when photoirradiated at a wavelength at 365 nm, with a CO-evolution selectivity of 98.6% (7.4 μmol h^{-1}). The Ag and Co cocatalysts were found to function as reduction and oxidation sites for promoting the generation of CO and O_2, respectively, on the Al-$SrTiO_3$ surface.

Introduction

The photo-irradiative conversion of CO_2 into chemicals over semiconductor photocatalysts typically includes three steps: (1) light harvesting, (2) photoexcited electron–hole pair generation, separation, and transfer (charge transfer), and (3) surface catalytic reactions that include reduction by electrons and oxidation by holes.[1-3] An urgent challenge involves preventing the rapid recombination of photogenerated electron–hole pairs within single photocatalyst particles, which results in lower photocatalytic performance of the semiconductor catalyst.[4-6] Cocatalysts that provide essential functions during photocatalytic reactions not only promote the separation of photogenerated electron–hole pairs, but also reduce the activation potential and serve as active sites for the photocatalytic evolution of products.[1-2, 4, 7-14] Photocatalyst surfaces decorated with Ag nanoparticles were reported in 2011 to be good cocatalysts that exhibit superior selectivities for photocatalytic products, such as CO from CO_2, when photoirradiated.[12] In addition, many kinds of material, including noble metals (such as Au,[12] Pt,[15-16] and Pd[17]), non-noble metals (such as Cu[15, 18]), and metal oxides (such as MgO,[16] NiO,[19] and Cu_2O[20]) have been studied as cocatalysts for the photocatalytic conversion of CO_2 into chemicals such as CO and CH_4. Furthermore, dual cocatalysts have been investigated to overcome the shortcomings of single cocatalyst-loaded photocatalysts; i.e., to improve CO_2 chemisorption,[16] suppress the back reaction,[21] and enhance the consumption of photogenerated holes.[22-23] Dual metal–metal alloy cocatalysts (such as Pt-Cu,[15] and Au-Cu[24-25]) and metal–metal-oxide dual cocatalysts (such as Pt-MgO,[16] Ni@NiO,[26] Ag@Cr,[21, 27] and Pt@Cu_2O[28]) have been loaded onto the surfaces of photocatalysts to improve their photocatalytic performance for the conversion CO_2 into chemicals when photoirradiated. Specifically, a photocatalytic reaction contains two important components: (1) photoexcited electrons for the reduction reaction, and (2) photoexcited holes for the oxidation reaction, based on charge balance. Normally, attention is only paid to the photocatalytic CO_2 reduction side involving photoexcited electrons, while the H_2O oxidation process has largely been neglected. Improving the activity of the oxidation half-reaction should reduce photoexcited electron–hole recombination inside a single photocatalyst, which would enhance the activity of the reduction half reaction as larger numbers of electrons are transferred for the photocatalytic reaction on the surface of the photocatalyst.

The morphological structure of a semiconductor catalysts is known to clearly affect photocatalytic performance, as photocatalytic reactions occur on its surface. Recently, Yu et al. reported that the photocatalytic activity for CO_2 reduction over anatase TiO_2 depended on the {001}:{101} facet ratio.[29] In particular, the crystal structures of La-doped $NaTaO_3$,[30] anatase TiO_2,[31-32] $BiVO_4$,[11, 33-34] 18-facet-$SrTiO_3$,[35] and Al-$SrTiO_3$[36-37] have been studied as water-splitting photocatalysts, with photogenerated electrons and holes reportedly spatially transferred to different exposed facets when photoirradiated, which is considered to enhance photocatalytic activity. Li et al. proposed that cocatalysts on the spatial facets of the $BiVO_4$ photocatalyst not only serve their traditional reaction roles, but also align the built-in electric field vectors of the photocatalyst particles, which maximizes the separation and transfer of photoexcited electrons and holes.[11] CoO_x and other Co species have recently been loaded on various photocatalysts as oxidation cocatalysts that enhance photocatalytic oxygen-evolution reaction (OER) activity.[38-39] In particular, Domen et al. reported that Al-$SrTiO_3$ modified with the dual Rh/Cr_2O_3 cocatalyst and CoOOH on its various facets exhibited extremely high photocatalytic water-splitting activity without losses due to charge recombination, with a quantum efficiency of up to 96% at wavelengths of 350–360 nm.[37] Furthermore, the photocatalytic activity for CO_2 reduction has also been significantly improved by simultaneously loading dual cocatalysts (reduction and oxidation cocatalysts) onto different spatial facets of a photocatalyst.[22, 40-42] In our previous work, Al-$SrTiO_3$ fabricated using a flux method and modified with a Ag cocatalyst showed good efficiency and selectivity towards CO evolution in an aqueous solution when irradiated with light at wavelengths above 300 nm.[43-44] In addition, the Ag cocatalyst on the surface of Al-$SrTiO_3$ prepared using a chemical reduction (CR) method was found to show good photocatalytic performance for the reduction of CO_2 compared to those prepared by impregnation (IMP) and photodeposition (PD) methods, because highly dispersed metallic Ag nanoparticles were produced.[44-46] Herein, we report the effect of Ag and Co dual-cocatalyst loading on Al-$SrTiO_3$ (AgCo/Al-$SrTiO_3$) on the photocatalytic reactivity for the conversion of CO_2 into CO when photoirradiated, with water as the reductant.

Experimental

Preparing Al-$SrTiO_3$

Perovskite-structured $SrTiO_3$ was fabricated using a solid-state reaction, with stoichiometric $SrCO_3$ (3.10 g) and TiO_2 (1.59 g) as the Sr and Ti sources.[47] The $SrCO_3$:TiO_2 molar ratio was 1.05 because $SrCO_3$ was observed to evaporate. After grinding for 10 min, the mixture was transferred to an alumina crucible and calcined at 1373 K for 10 h in air, after which the sample was washed at 353 K with ultrapure deionized water several times and dried at 298 K overnight. A facile flux method was used to fabricate Al-$SrTiO_3$ using the prepared $SrTiO_3$.[36, 43]

Loading the catalyst onto the Al-$SrTiO_3$

The Ag and Co dual cocatalyst was simultaneously used to modify the surface of the as-prepared Al-$SrTiO_3$ photocatalyst using a chemical-reduction (CR) method. Al-$SrTiO_3$ (0.75 g) was dispersed in ultrapure deionized water (50 mL) and 0.1 M aqueous solutions of $AgNO_3$ (0.695 mL) and $Co(NO_3)_2$ (0.347 mL), and a 0.4 M aqueous solution of NaH_2PO_2 (1.50 mL) were added to the suspension in a stepwise manner. After the suspension was maintained at 353 K for 1.5 h, it was filtered and the collected powder was dried in air at 298 K overnight. Meanwhile, the Ag and Co dual cocatalyst was also singly loaded on Al-$SrTiO_3$ using the CR method. The Ag and Co-loaded Al-$SrTiO_3$ sample are referred to as "Ag(*x*)Co(*y*) Al-$SrTiO_3$", where *x* is the Ag cocatalyst loading (0.0, 0.5, 1.0, 1.5, 1.7, 2.0m and 2.5 mol%) and *y* is the Co cocatalyst loading (0.0, 0.425, 0.85, 1.275, 1.7, and 2.5 mol%).

For the impregnation (IMP) method, an aqueous solution of $AgNO_3$ (0.695 mL, 0.1M) and $Co(NO_3)_2$ (0.347 mL, 0.1M) was dispersed into 20 mL of an aqueous suspension of Al-$SrTiO_3$ (0.75 g). After aging at 353 K for 0.5 h, the mixture was evaporated at 353 K for 1.0 h with stirring, after which the dried mixture was ground and calcined at 723 K for 2 h in air.

The various cocatalysts were used to modify the surfaces of Al-$SrTiO_3$ photocatalysts using the photodeposition (PD) method, in which 0.75 g of Al-$SrTiO_3$ was dispersed in ultrapure deionized water (1000 mL), and a 0.1 M aqueous solution of $AgNO_3$, H_2PtCl_6, or $HAuCl_4$ (0.695 mL) was added into the suspension. In addition, a stoichiometric amount of $NaIO_3$ was added into the suspension as the hole donor when MnO_2, PbO_2, or Co_3O_4 catalysts were loaded onto Al-$SrTiO_3$

using $Mn(NO_3)_2$, $Pb(NO_3)_2$, or $Co(NO_3)_2$ (0.347 mL, 0.1 M aq.) as the metal source. After purging the air from the reactor with flowing Ar, the suspension was irradiated using a 400-W high-pressure Hg lamp with a quartz jacket connected to a water-cooling system, while Ar was bubbled through the suspension at 30 mL min^{-1}. The cocatalyst-loaded Al-$SrTiO_3$ samples were then vacuum filtered, washed, and dried at 298 K in air overnight.

Characterization

The crystalline properties of $SrTiO_3$ and Al-$SrTiO_3$ were characterized by X-ray diffractometry (XRD) using a Rigaku Ultima IV powder diffractometer equipped with a Cu Kα (λ = 0.154056 nm) radiation source operating at 30 kV and 30 mA. UV-visible diffuse reflectance (UV-vis DR) spectroscopy on a JASCO V-670 instrument equipped with an integrating sphere was used to acquire absorption spectra of the samples. Spectralon® (Labsphere Inc.) was used as the standard reflection sample. In addition, the microstructure and morphology of each sample was examined by field-emission scanning electron microscopy (SEM; SU-8220, Hitachi High-Technologies, Japan), augmented by energy dispersive X-ray spectroscopy (EDS) (15.0 kV). Meanwhile, transmission electron microscopy (TEM, JEM-2100F, Japan) was used to examine the morphologies of the AgCo/Al-$SrTiO_3$ photocatalysts. The actual amounts of the Ag and Co species loaded on the AgCo/Al-$SrTiO_3$ samples were determined by X-ray fluorescence (XRF) with an energy-dispersive X-ray (EDX-8000, Shimadzu, Japan) spectrometer. Co 2p X-ray photoelectron spectra of AgCo/Al$SrTiO_3$ were acquired to determine the valences of the Co cocatalysts (XPS, ESCA 3400, Shimadzu Corp., Japan). The X-ray absorption fine structure (XAFS) of the Ag K-edge (beam line BL01B1) and Co K-edge (beam line BL37XU) were examined at the SPring-8 synchrotron facility. The liquid products in the reaction solution was analysed using the high-performance liquid chromatography (HPLC 4000, JASCO Corp., Japan)

Photocatalytic reactions

CO_2 was photocatalytically converted with H_2O as the electron donor using a quasi-flow batch system with an internal-irradiation-type reaction vessel at 298 K and under ambient pressure. AgCo/Al-$SrTiO_3$ (0.5 g) was added to an aqueous solution of $NaHCO_3$ (0.1 M, 1.0 L) and CO_2 (99.999%, 30 mL min^{-1}) was bubbled through the suspension. A 400-W high-pressure Hg lamp with a water-cooled Pyrex® jacket (to cut off light at $\lambda < 300$ nm) was used to irradiate the sample. The gaseous products that evolved from the photoreaction system (i.e., H_2, and O_2) were analyzed by gas chromatography with a thermal conductivity detector (TCD–GC; Model: GC-8A, Shimadzu Corporation, Japan.) with a 5A molecular sieve (MS 5A) column, and Ar a the carrier gas. In addition, the photocatalytic CO product was analyzed using a flame-ionization detector (FID–GC; Model: GC-8A, Shimadzu Corporation, Japan) with a methanizer, and a Shincarbon ST column, and N_2 as the carrier gas.

The photocatalytic reaction was also carried out in a quasi-flow batch system in a 200 mL reactor with external irradiation at 365 nm to determine the apparent quantum efficiency (QE). AgCo/Al-$SrTiO_3$ (0.1 g) was dispersed in $NaHCO_3$ (0.1 M, 0.2 L) with CO_2 (99.999%, 30 mL min^{-1}) bubbling. The suspension was then irradiated at 365 nm using an LED controller (Model: IRS-1000, CELL System Co., Ltd., Japan). The photoirradiation area was a 5-cm-diameter circle. The gaseous products were analyzed using the same TCD–GC and FID–GC systems detailed above.

Results and Discussion

Figures 1(b) and (c) show the XRD patterns of $SrTiO_3$ and Al-$SrTiO_3$, in which most peaks are assigned to the $SrTiO_3$ phase (Figure 1(a)), with only a few small peaks attributable to the $Sr_3Ti_2O_7$ phase. Moreover, the impurity phase was absent after doping with Al using the flux method (Figure 1(c)), with all peaks assigned to the Al-$SrTiO_3$ phase. Furthermore, Figures 1(d)–(e) show SEM images of $SrTiO_3$ and Al-$SrTiO_3$. The $SrTiO_3$ and Al-$SrTiO_3$ particles exhibit irregular polyhedral morphologies, with numerous nanosteps formed on the spatial surfaces of Al-$SrTiO_3$, as reported previously.[43] The morphologies and crystalline structures of the prepared samples are consistent with those in previous reports.[36, 43]

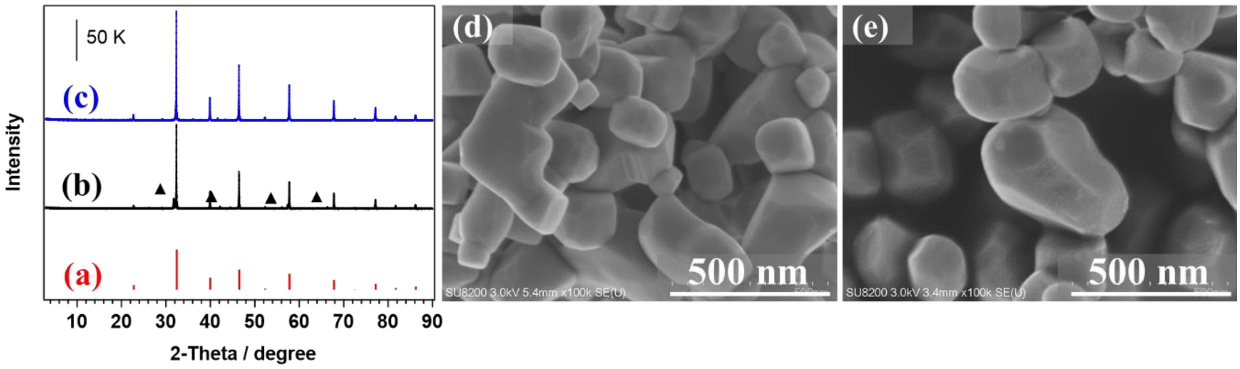

Figure 1. XRD patterns of (a) the $SrTiO_3$ reference (ICSD no. 23076) and the synthesized (b) $SrTiO_3$ (▲ $Sr_3Ti_2O_7$) and (c) Al-$SrTiO_3$. SEM images of the synthesized (d) $SrTiO_3$ and (e) Al-$SrTiO_3$.

The photocatalytic performance of Al-$SrTiO_3$ modified with various cocatalysts, including single Ag and Co, and dual Ag and Co cocatalysts prepared by the CR method are summarized in Table 1. H_2, O_2, and CO were detected by GC as the gaseous products, and no liquid products were observed in the reaction solutions by using high-performance liquid chromatography (HPLC). Importantly, the consumed e^-/h^+ ratios were found to be close to 1.0 over the $SrTiO_3$, Ag/$SrTiO_3$, Co/Al-$SrTiO_3$, and AgCo/Al-$SrTiO_3$ photocatalysts. Table 2 shows that Ag and Co were successfully loaded on the surface of the Al-$SrTiO_3$ photocatalyst. Only very small amounts of gaseous H_2, O_2, and CO were detected over bare Al-$SrTiO_3$, and the H_2-formation rate was much higher than the CO-formation rate with non-stoichiometric amounts of O_2 produced. The main reductive product was found to be gaseous CO (97.7%) over Ag/$SrTiO_3$, and a stoichiometric amount of O_2 was evolved, which indicates that H_2O functions as an electron donor in the photocatalytic reaction. The CO-formation rate was significantly enhanced (4.7 μmol h^{-1}) compared to the undoped catalyst. As mentioned in previous reports,[12-13, 48] Ag functions as a potential cocatalyst that enhances the photocatalytic activity for the reduction of CO_2 and is selective toward CO evolution. Furthermore, the Al-$SrTiO_3$ photocatalyst was also loaded with Co species, as Co has been described to be a good cocatalyst for the photocatalytic oxidation of water;[38-39] while high H_2- and O_2-formation rates (41.6 and 19.5 μmol h^{-1}, respectively) were obtained over Co/Al-$SrTiO_3$, and that for CO formation was only 0.1 μmol h^{-1}, which indicates that overall only water splitting took place over the Co/Al-$SrTiO_3$ photocatalyst. Surprisingly, the highest CO-formation rate (52.7 μmol h^{-1}), which is 10-times higher than that observed for Ag/Al-$SrTiO_3$, was delivered by the Al-$SrTiO_3$ photocatalyst dual-modified with both Ag and Co by the CR method (AgCo/Al-$SrTiO_3$_CR). Meanwhile, the selectivity for CO evolution was further improved to 99.8%, with only a trace of H_2 evolved over AgCo/Al-$SrTiO_3$_CR. To the best of our knowledge, this is the highest selectivity for CO evolution reported for photocatalytic CO_2 conversion using H_2O as a reductant under aqueous conditions at wavelength (λ) above 300 nm .[12-13, 21, 23, 49-52] Consequently, we conclude that Co species in the photocatalyst significantly enhance photocatalytic performance for CO_2 conversion because they effectively promote the water-oxidation half reaction.

The H_2-, O_2-, and CO-formation rates during the photocatalytic conversion of CO_2 by H_2O over AgCo/Al-$SrTiO_3$ prepared by the IMP, CR, and PD methods are also listed in Table 1. The amounts of Ag and Co loaded into AgCo/Al-$SrTiO_3$ prepared by these methods were determined by XRF spectroscopy (Table 2), which suggested that the Ag and Co cocatalysts had been successfully loaded onto the surface of the Al-$SrTiO_3$ prepared using each method.

The selectivity toward CO evolution was very low (59.2%) over AgCo/Al-$SrTiO_3$_PD. In addition, AgCo/Al-$SrTiO_3$_IMP exhibited a very low CO-formation rate of 4.1 μmol h^{-1}. Undoubtedly, the highest CO-formation rate was delivered by AgCo/Al-$SrTiO_3$ prepared by the CR method, with exceptionally good selectivity toward CO evolution also observed. Compared with Ag/Al-$SrTiO_3$ and Co/Al-$SrTiO_3$, AgCo/Al-$SrTiO_3$ prepared by the PD and CR methods exhibited higher activities for the photocatalytic CO_2 reduction and H_2O oxidation, which indicates that, apart from Co playing an important role in enhancing the water oxidation half reaction, the Ag and Co species function synergistically. Furthermore, the amounts of the Ag and Co cocatalysts loaded by the CR method were also determined by XRF spectroscopy, the results of which are summarized in Table 2. The XRF-determined amount of Ag on the surface of the Al-$SrTiO_3$ photocatalyst was found to be similar to the amount of Ag precursor used in the reaction (Table 2), whereas the amount of Co was determined to be lower than the amount of precursor used, particularly at Co precursor levels higher than 0.85%. The effect of the loaded-amount of the dual Ag and Co cocatalyst on the photocatalytic activity for CO_2 reduction are shown in Figures 2–4, which reveal that photocatalytic performance depends on the Ag and Co loading. These results show that Ag(1.7)Co(0.85)/Al-$SrTiO_3$ and Ag(1.7)Co(1.275)/Al-$SrTiO_3$ prepared by the CR method exhibit the highest CO-formation rates of 52.7 μmol h^{-1} and 54.6 μmol h^{-1}, respectively, with good selectivities toward CO evolution. Ag(1.7)Co(0.85)/Al-$SrTiO_3$ is referred to as AgCo/Al-$SrTiO_3$_CR hereafter.

Table 1. Photocatalytic conversion of CO_2 into CO by reduction with H_2O over various cocatalyst-loaded photocatalysts prepared by CR method [a]

Photocatalyst	**Product formation rate (μmol h^{-1})**			**Selectivity toward CO (%)**	e^-/h^+
	H_2	**O_2**	**CO**		
Al-$SrTiO_3$	0.35	0.2	0.08	18.5	1.08
Ag/Al-$SrTiO_3$	0.1	2.6	4.7	97.7	0.92
Co/Al-$SrTiO_3$	41.6	19.5	0.1	0.2	1.07
AgCo/Al-$SrTiO_3$_CR	0.1	25.8	52.7	99.8	1.02
AgCo/Al-$SrTiO_3$_PD	14.1	17.5	20.5	59.2	0.99
AgCo/Al-$SrTiO_3$_IMP	0.2	2.8	4.1	95.0	0.77

[a] Photocatalytic reaction conditions: Amount of photocatalyst, 0.5 g; amount of Ag loaded, 1.7 mol%; amount of Co loaded, 0.85 mol%; volume of the reaction solution (H_2O), 1.0 L; additive, 0.1 M $NaHCO_3$; CO_2 flow rate, 30 mL min^{-1}; light source, 400 W high-pressure Hg lamp with a Pyrex® jacket (to cutoff light at λ < 300 nm).

Table 2. The XRF data of the different amount of Ag and Co loaded Al-$SrTiO_3$ prepared by CR, PD, IMP method.

Sample	Ag mol%	Co mol%
Ag(0)Co(0)	0.00	0.00
Ag(1.7)Co(0)_CR	1.78	0.00
Ag(1.7)Co(0.425)_CR	1.68	0.35
Ag(1.7)Co(0.85)_CR	1.82	0.76
Ag(1.7)Co(1.275)_CR	1.72	0.69
Ag(1.7)Co(1.7)_CR	1.84	1.06
Ag(0)Co(0.85)_CR	0.00	0.75
Ag(0.5)Co(0.85)_CR	0.53	0.89
Ag(1.0)Co(0.85)_CR	1.02	0.83

Ag(1.5)Co(0.85)_CR	1.62	0.91
Ag(2.0)Co0.85)_CR	2.13	0.76
Ag(0.5)Co(0.25)_CR	0.45	0.29
Ag(1.0)Co(0.5)_CR	1.03	0.49
Ag(1.5)Co(0.75)_CR	1.82	0.68
Ag(1.7)Co(0.85)_CR	1.82	0.76
Ag(2.0)Co(1.0)_CR	1.97	0.61
Ag(2.5)Co(1.25)_CR	2.57	0.53
Ag(1.7)Co(0.85)_PD	1.75	0.86
Ag(1.7)Co(0.85)_IMP	1.67	0.87
Ag(1.7)Co(0.85)_CR_hv 5h	1.71	0.77

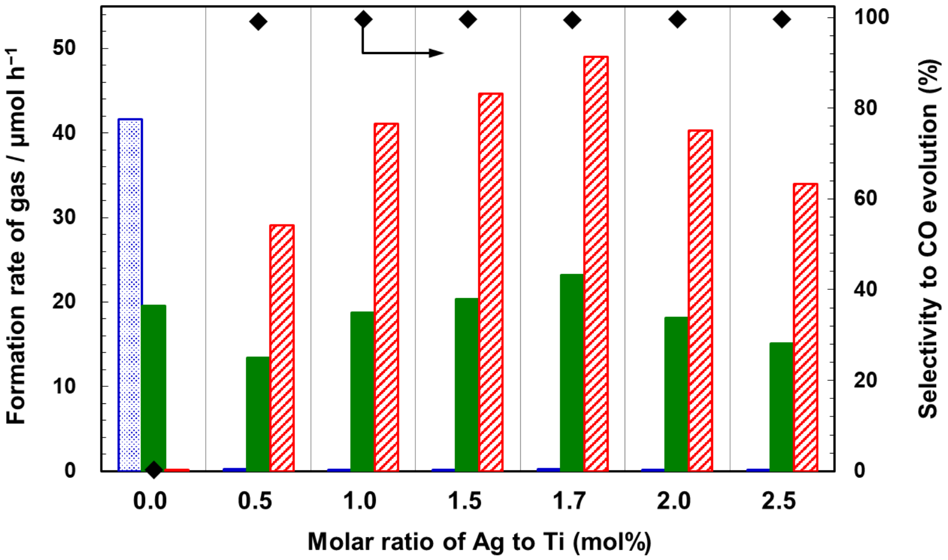

Figure 2. Formation rates of H_2 (blue dotted), O_2 (green filled), and CO (red slashed) for the photocatalytic conversion of CO_2 by H_2O over the 0.85 mol% Co and various amounts of the 0.00, 0.50, 1.0, 1.5, 2.00, and 2.5 mol% Ag cocatalyst loaded Al-$SrTiO_3$ prepared by CR method.

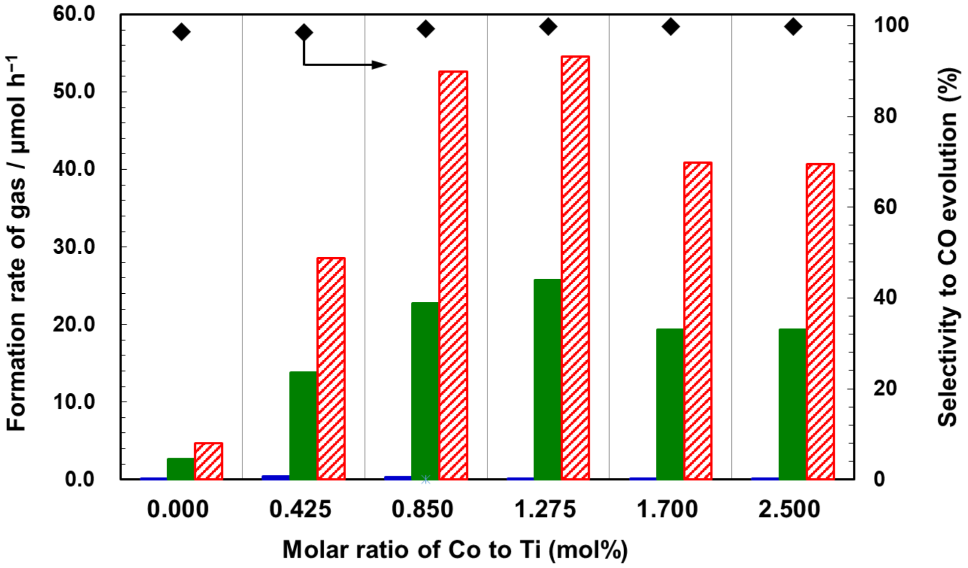

Figure 3. Formation rates of H_2 (blue dotted), O_2 (green filled), and CO (red slashed) for the photocatalytic conversion of CO_2 by H_2O over the 1.7 mol% Co and various amounts of the 0.00, 0.425, 0.850, 1.275, 1.7, and 2.5 mol% Co cocatalyst loaded Al-$SrTiO_3$ prepared by CR method.

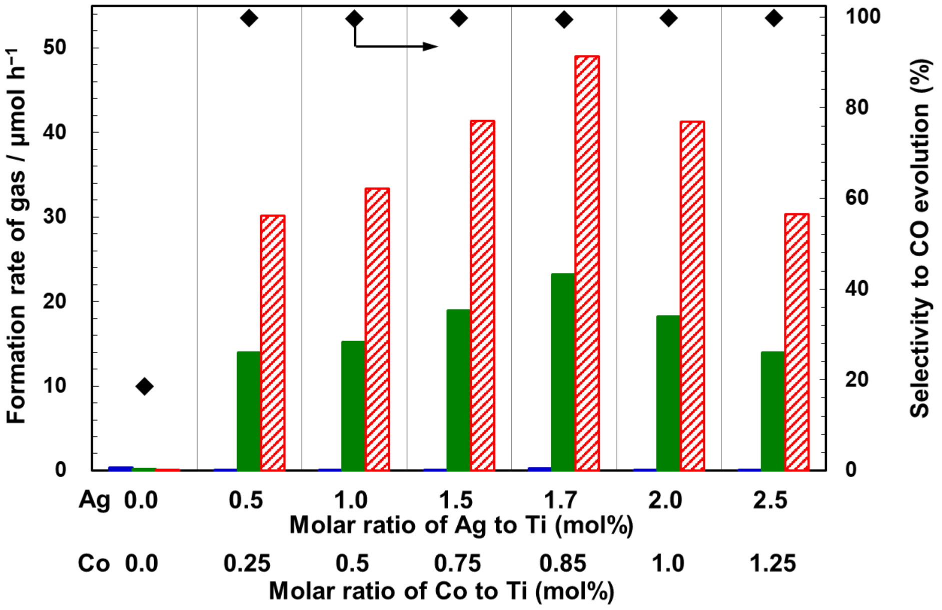

Figure 4. Formation rates of H_2 (blue dotted), O_2 (green filled), and CO (red slashed) for the photocatalytic conversion of CO_2 by H_2O over the different amount of Ag and Co loaded Al-$STiO_3$ prepared by CR method.

To determine apparent quantum efficiencies, photocatalytic CO_2 reductions over AgCo/Al-$SrTiO_3$_CR were also carried out in aqueous $NaHCO_3$ (0.1 M) using various light sources. Figure 5(a) shows time courses for the evolution of CO, H_2, and O_2 during the photocatalytic conversion of CO_2 by H_2O over AgCo/Al-$SrTiO_3$_CR when irradiated at wavelengths (λ) above 300 nm for 5 h under typical conditions. Importantly, the same reaction (photocatalytic reduction of CO_2 by H_2O) was also carried out under monochromatic light ($\lambda = 365$ nm) in $NaHCO_3$ (0.2 L, 0.1 M), the results of which are shown in Figure 5(b); the CO-formation rate was approximately 7.4 µmol h^{-1} with good selectivity toward CO evolution (98.6%). The apparent quantum efficiency (***AQE***) of 0.03% was calculated using Eq. (1):

$$\boldsymbol{AQE}\ (\%) = \mathbf{(number\ of\ reacted\ electrons\ /number\ of\ incident\ photons)\times 100} \qquad (1)$$

Although this ***AQE*** value is much lower than desired, it is important to note that a ***AQE*** was obtained in this photocatalytic CO_2-reduction system. The amounts of Ag and Co in the AgCo/Al-$SrTiO_3$ photocatalyst were also determined by XRF spectroscopy after CO_2 had been photoreduced for 5 h, the results of which are summarized in Table 2, which reveals that Ag and Co loadings are only slightly lower compared to those of the as-prepared sample. These results suggest that Ag and Co are durable under the reaction conditions, as their photocatalyst loadings were stable over the 5-h duration of the photocatalytic reaction.

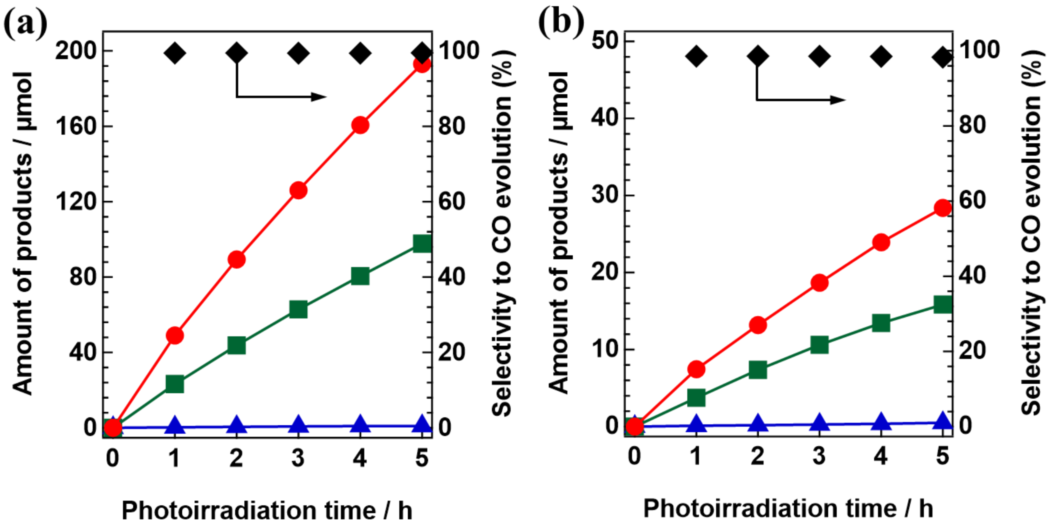

Figure 5. Time courses for the evolution of H_2 (blue triangle), O_2 (green square), CO (red circle), and selectivity toward CO evolution (black) for the photocatalytic conversion of CO_2 by H_2O over AgCo/Al-$SrTiO_3$ using various light sources: (a) 400-W high pressure Hg lamp with a Pyrex® jacket at $\lambda > 300$ nm, (b) LED lamp at $\lambda = 365$ nm. Photocatalytic reaction conditions: Amount of photocatalyst, (a) 0.5g and (b) 0.1 g; amount of Ag loaded, 1.7 mol%; amount of Co loaded, 0.85 mol%; volume of the reaction solution (H_2O), (a) 1.0 L and (b) 0.2 L; additive, 0.1 M $NaHCO_3$; CO_2 flow rate; 30 mL min^{-1}.

Figure 6(a) shows Ag K-edge XANES spectra of Ag/Al-$SrTiO_3$ and AgCo/Al-$SrTiO_3$_CR, and those of Ag foil, Ag_2O, and Ag_3PO_4 as references. The absorption edges of the Ag species in Ag/Al-$SrTiO_3$ and AgCo/Al-$SrTiO_3$ prepared by the CR method are consistent with that of Ag foil, at 25528 eV; [21, 23] in addition, the Ag K-edge XANES spectra of Ag/Al-$SrTiO_3$ and AgCo/Al-$SrTiO_3$_CR exhibit features that are similar to that of Ag foil. These results indicate that the Ag species in these photocatalysts are metallic, and the presence of Co does not influence the chemical state of the Ag species. Figure 6(b) shows the Co K-edge XANES spectra of Co/Al-$SrTiO_3$ and AgCo/Al-$SrTiO_3$_CR, with those of Co_3O_4, CoOOH, [53-54] $Co_3(PO_4)_2$, and CoO included for reference, which reveals that the Co K-edge XANES spectra of Co/Al-$SrTiO_3$ and AgCo/Al-$SrTiO_3$_CR do not match those of $Co_3(PO_4)_2$ and CoO; the AgCo/Al-$SrTiO_3$_CR absorption edge was closer to those of CoOOH and Co_3O_4. Furthermore, the white-line and peak maximum (7727.6 eV) in the Co K-edge XANES spectrum of AgCo/Al-$SrTiO_3$_CR are consistent with those of the CoOOH reference, even though the spectral features are slightly different.[54-55] The differences between the Co K-edge XANES spectra of AgCo/Al-$SrTiO_3$_CR and CoOOH are possibly ascribable to highly dispersed Co species on the Al-$SrTiO_3$ surface, as XANES spectra are reportedly affected by nanoparticle size.[56-57] In addition, the Co K-edge EXAFS oscillation of AgCo/Al-$SrTiO_3$_CR is approximately consistent with that of CoOOH rather than Co_3O_4 (Figure 7), which indicates that CoOOH exists on the AgCo/Al-$SrTiO_3$_CR surface. The XANES spectra of Co/Al-$SrTiO_3$ and AgCo/Al-$SrTiO_3$_CR also overlap, as shown in Figure 6(c). The Co absorption edge of Co/Al-$SrTiO_3$ is slightly shifted to lower energy compared to that of AgCo/Al-$SrTiO_3$_CR, while the Co K-edge XANES features are also different. Consequently, the presence of Ag affects the chemical structure of the Co species when Ag and Co species are simultaneously loaded using the CR method.

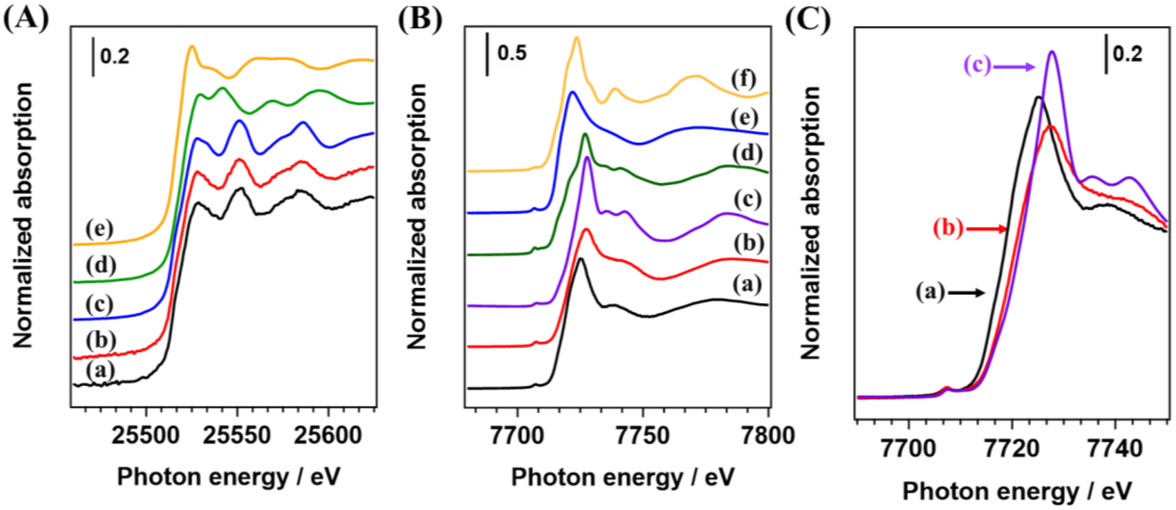

Figure 6. (A) Ag K−edge XANES spectra of (a) Ag/Al-$SrTiO_3$, (b) AgCo/Al-$SrTiO_3$_CR, (c) Ag foil, (d) Ag_2O, and (e) Ag_3PO_4. (B) and (C) Co K−edge XANES spectra of (a) AgCo/Al-$SrTiO_3$_CR, (b) Co/Al-$SrTiO_3$, (c) CoOOH, (d) Co_3O_4, (e) $Co_3(PO_4)_2$, and (f) CoO

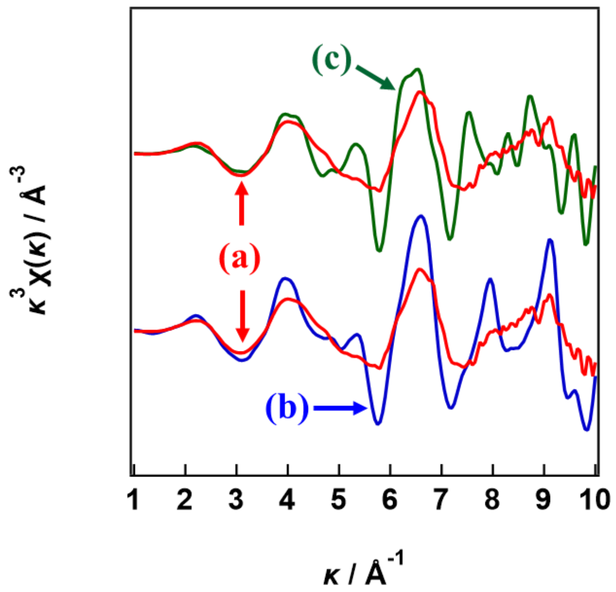

Figure 7. Co K−edge EXAFS oscillations of (a) AgCo/Al-$SrTiO_3$_CR, (b) CoOOH, and (c) Co_3O_4.

Figure 8 shows SEM images of the Ag/Al-$SrTiO_3$, Co/Al-$SrTiO_3$, and AgCo/Al-$SrTiO_3$_CR photocatalysts. Ag nanoparticles approximately 2−25 nm in size are uniformly dispersed on the Al-$SrTiO_3$ surface, as shown in Figure 8(a), while no obvious nanoparticles are observed in the SEM image of Co/Al-$SrTiO_3$ (Figure 8(b)), although the XRF data indicate that Co had been successfully loaded on the Al-$SrTiO_3$ surface (Table 2). In addition, the Co/Al-$SrTiO_3$ EDS map and Co 2p XPS spectrum (Figure 9) also show that Co species are present on the Al-$SrTiO_3$ surface. The author believes that the Co species on the Al-$SrTiO_3$ are too small to be observed by SEM. AgCo/Al-$SrTiO_3$_CR exhibited a similar morphology to that of Ag/Al-$SrTiO_3$; the Al-$SrTiO_3$ particles are well covered by nanoparticles around 2–20 nm in size, with nanoparticles larger than 20 nm rarely observed on the photocatalyst surface. Figures 8(d) and (e) show SEM images of Ag/Al-$SrTiO_3$, Co/Al-$SrTiO_3$, and AgCo/Al-$SrTiO_3$_CR after 5 h of photoirradiation, which reveal that Ag metal nanoparticles are only present on smooth Ag/Al-$SrTiO_3${100} facets, with no Ag nanoparticles present on other facets, whereas Co species are observed on nanostep Co/Al-$SrTiO_3${110} facets; therefore, the Ag metal and Co nanoparticles apparently moved to the smooth {100} and nanostep {110} facets during photoirradiation, respectively. Note that the positions of the Ag and Co species, which were highly dispersed on the surface in a random fashion, are different after photoirradiation. In addition, the Ag and Co nanoparticle cocatalysts are both observed on every facet of each Al-$SrTiO_3$ particle in Figure 8(f) in the case of AgCo/Al-$SrTiO_3$_CR, which indicates that the smooth {100} and nanostep {110} facets prefer to be decorated with Ag metal nanoparticles and Co nanoparticles, respectively, when irradiated. Moreover, the SEM images of the AgCo/Al-$SrTiO_3$ photocatalysts prepared by the IMP and PD methods are shown in Figure 10, which reveals that the surface of AgCo/Al-$SrTiO_3$_IMP contains several large cocatalyst particles (Figure 10(a)). Numerous Ag nanoparticles were observed to have aggregated on {100} facets after 5 h of photocatalytic reaction, in addition to the large cocatalyst particles on the surfaces of the photocatalyst particles. The unusual size of the cocatalyst on AgCo/Al-$SrTiO_3$_IMP negatively affects photocatalytic performance. Figure 10(b) shows that the Ag and Co dual cocatalyst is spatially located on the {100} facets and {110} facets when the PD method was used. In addition, the Ag nanoparticles on the {100} facets are much larger than those obtained using the CR method. Thus, the main reason for the poor selectivity of AgCo/Al-$SrTiO_3$_PD is likely to be the oversized Ag nanoparticles on its surface, as it is known that the Ag cocatalyst plays an important role during the photocatalytic reduction of CO_2 to CO. $BiVO_4$,[11, 34] 18-facet-$SrTiO_3$,[35] Al-$SrTiO_3$,[37] and $KTaO_3$,[40] which have exposed anisotropic facets, were also reported to exhibit similar properties. Li et al. reported that metals (Ag, Pt, and Au) and metal oxides (CoO_x, MnO_2, and PbO_2) are selectively loaded on various $BiVO_4$[11, 34] and 18-facet-$SrTiO_3$[35] facets when irradiated under aqueous conditions. In addition, the Rh/Cr hydrogen-evolution reaction (HER) cocatalyst and the CoOOH OER cocatalyst were also reported to be spatially photodeposited on the {100} and {110} facets of Al-$SrTiO_3$, respectivily.[37] Selective photodeposition was proposed to be due to the charge-rectification effect inside individual semiconductor photocatalyst particles.[37, 58] Moreover, an anisotropically deposited cocatalyst was reported to play a positive charge-separation and transfer role inside individual photocatalyst particles by aligning the electric fields built in the cocatalyst-loaded photocatalyst.[11] Therefore, Ag and Co species possibly appear on different Al-$SrTiO_3$ facets after photoirradiation because the {100} and {110} facets of Al-$SrTiO_3$ exhibit different band structures and band-edge positions.[29, 33, 37]

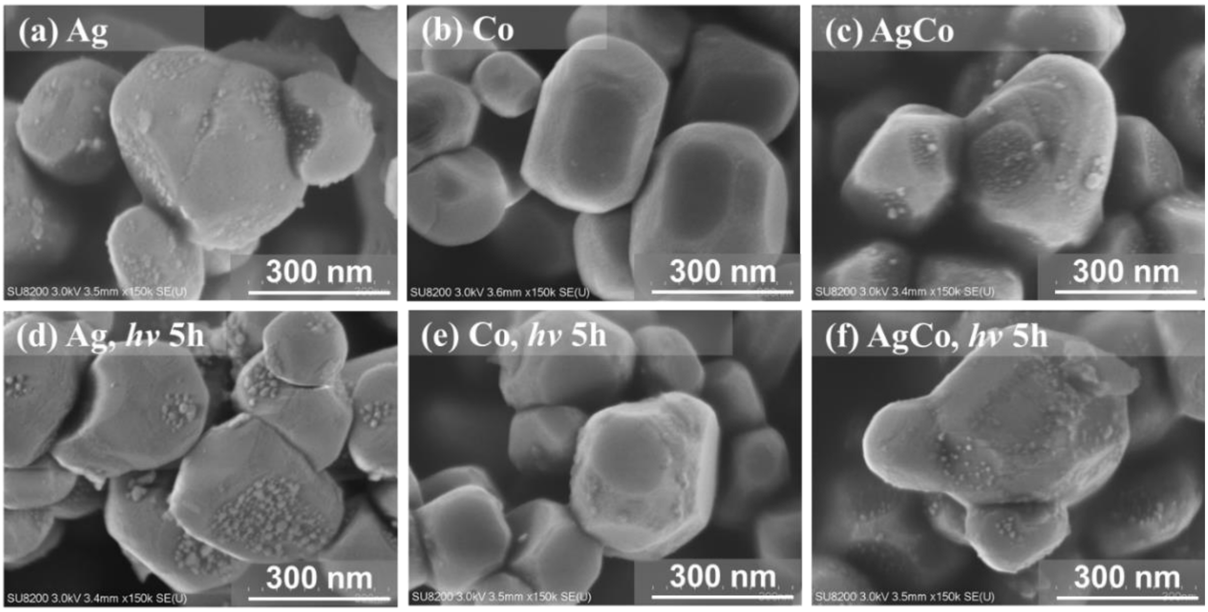

Figure 8. SEM images of various photocatalysts: (a, d) Ag/Al-$SrTiO_3$, (b, e) Co/Al-$SrTiO_3$, and (c, f) AgCo/Al-$SrTiO_3$_CR; (a–c) show fresh samples and (d–f) show samples after 5 h of photoirradiation.

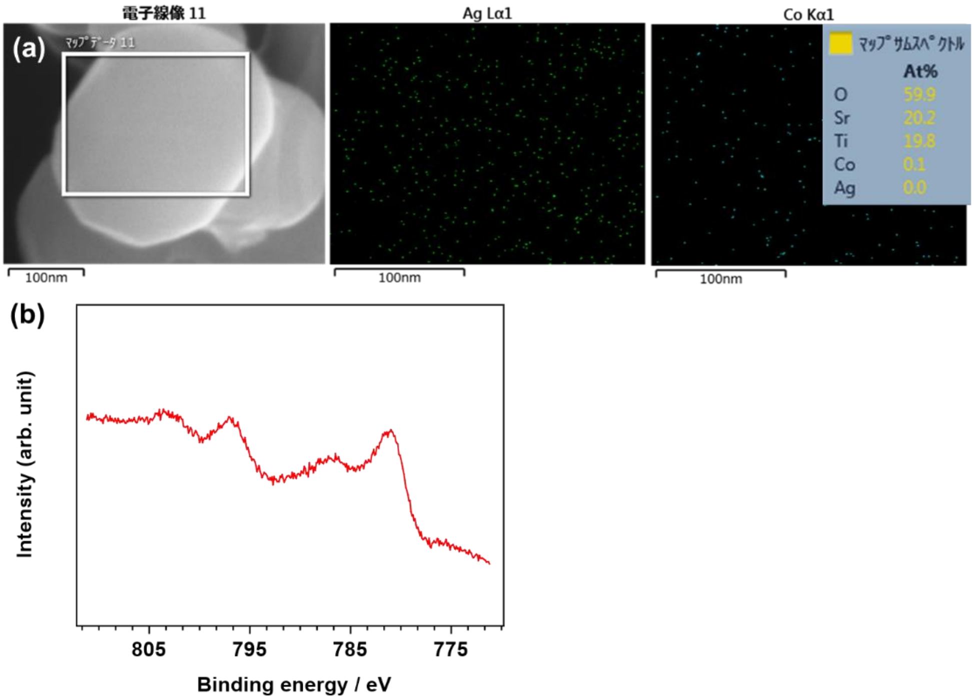

Figure 9 (a) The EDX mapping and spectra of the Co/Al-$SrTiO_3$, (b) Co 2p XPS spectrum of AgCo/Al-$SrTiO_3$_CR.

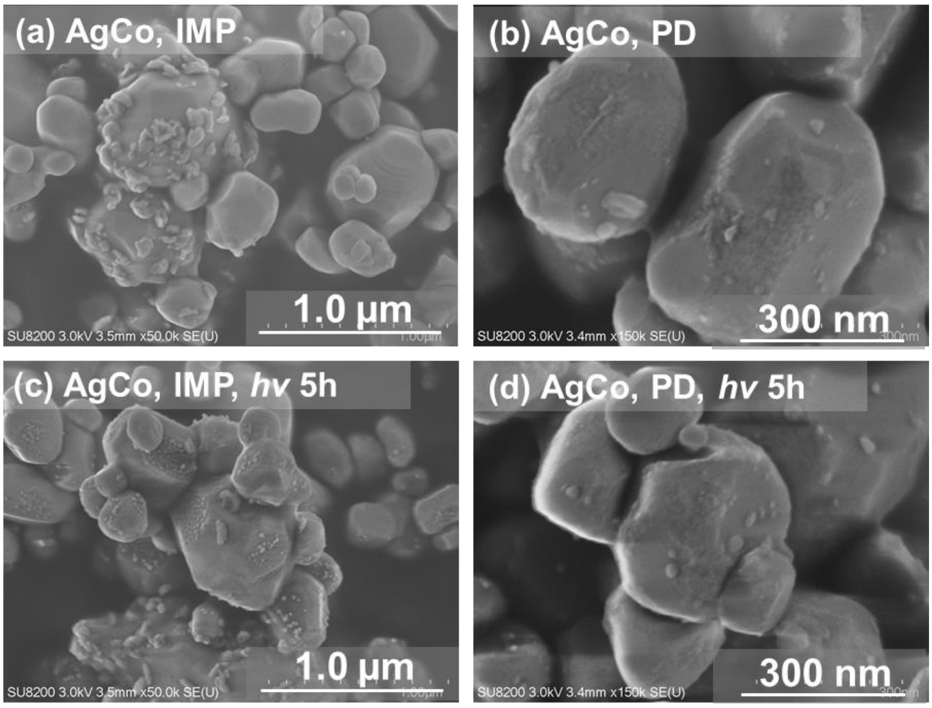

Figure 10. SEM image of the different cocatalyst loaded Al-$SrTiO_3$ prepared by different methods (a) and (c) AgCo prepared by IMP method, (b) and (d) Ag prepared by PD method, (a-b) before photocatalytic reaction, (c-d) after 5 h photocatalytic reaction.

The TEM images of AgCo/Al-$SrTiO_3$_CR reveal that the Ag and Co cocatalysts were deposited on the Al-$SrTiO_3$ surface, as shown in Figure 11, with nanoparticles around 2–20 nm in size; these nanoparticles exhibit a lattice distance of 0.242 nm, which is attributable to the Ag {111} facet.[59-60] Ag nanoparticles are aggregated on the {100} facets of single photocatalyst particles and much larger particles were observed after 5 h of photoirradiation, with the largest around 20 nm in size. In addition, Figures 11(b) and (d) reveal the appearance of numerous small nanoparticles on the {110} facets of the photocatalyst. As mentioned earlier, the XANES spectrum (Figure 6) suggests that highly dispersed CoOOH was generated on the Al-$SrTiO_3$ surface; however, there are no clear CoOOH fringe patterns visible in Figure 11(d), although the fringe pattern of the {110} facet of metallic Ag is observed, which indicates that the main Co species in AgCo/Al-$SrTiO_3$_CR is amorphous CoOOH.

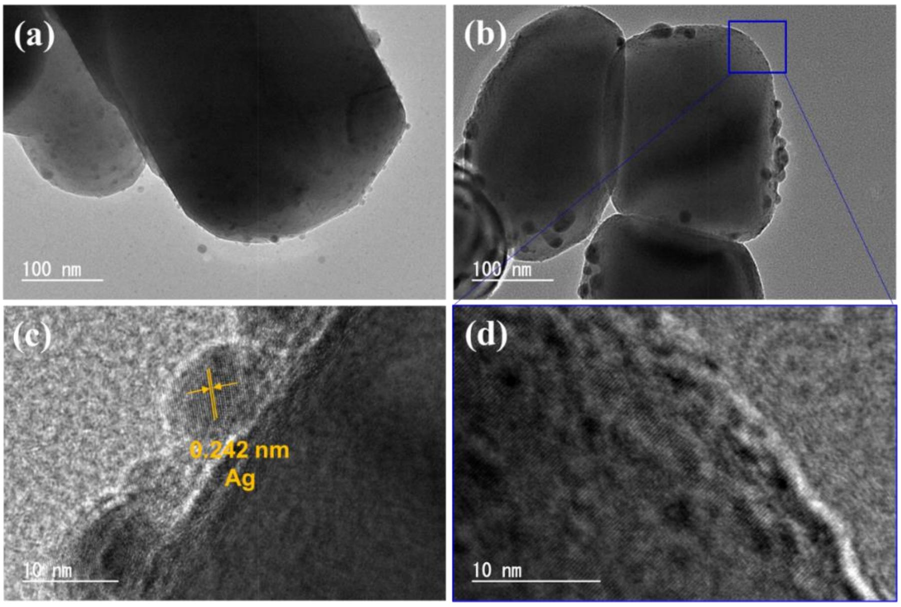

Figure 11. TEM images of AgCo/Al-$SrTiO_3$_CR photocatalysts: (a) before reaction and (b–d) after 5 h of photocatalysis. (c) Ag nanoparticles on a smooth Al-$SrTiO_3$ facet and (d) enlarged region showing AgCo/Al-$SrTiO_3$_CR nanostep facets.

The UV-Vis DR spectra of the Al-$SrTiO_3$, Ag/Al-$SrTiO_3$, Co/Al-$SrTiO_3$, and AgCo/Al-$SrTiO_3$_CR cocatalysts prepared by the CR method are shown in Figure 12. Al-$SrTiO_3$ exhibits an absorption edge at approximately 390 nm, which is consistent with that reported previously.[36, 43] However, broad absorption bands, which are assignable to surface plasmon resonance (SPR), are evident in the spectra of Ag/Al-$SrTiO_3$ and AgCo/Al-$SrTiO_3$_CR, but not Co/Al-$SrTiO_3$; these characteristic bands correspond to Ag nanopartices.[61] In addition, spectra f and g in Figure 12 reveal that that the SPR bands are slightly redshifted after use, which indicates that much larger nanoparticles are generated during photocatalysis. The author concludes that cocatalyst nanoparticles migrate and aggregate on the Al-$SrTiO_3$ surface during photoirradiation, as shown in the SEM and TEM images (Figures 8 and 11).[62]

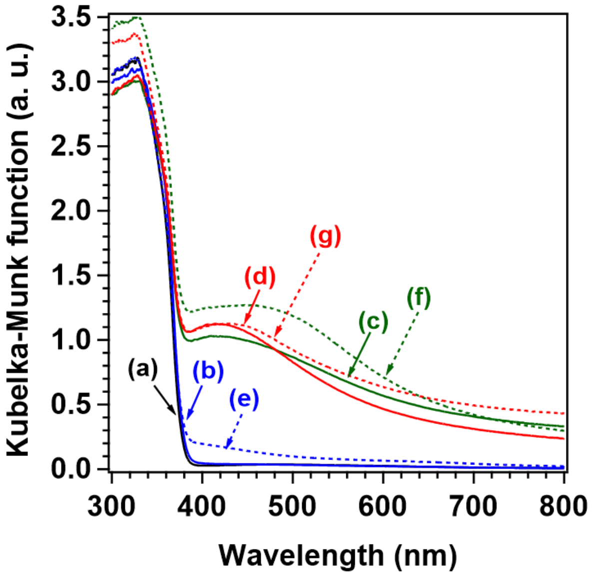

Figure 12. UV-Vis DR spectra: (a) Al-$SrTiO_3$, (b, e) Co/Al-$SrTiO_3$, (c, f) Ag/Al-$SrTiO_3$, and (d, g) AgCo/Al-$SrTiO_3$_CR. (b–d) As-prepared samples and (e–g) samples after 5 h of photocatalysis.

To further study the anisotropic properties of Al-$SrTiO_3$, the author investigated depositing various metals, such as Ag, Pt, Au, and metal oxides, such as MnO_2, PbO_2, and Co_3O_4, on the Al-$SrTiO_3$ surface by the PD method. Interestingly, metal nanoparticles (i.e., Ag, Pt, and Au), which were observed by EDS (Figure 13), were spatially deposited on the {100} facets of Al-$SrTiO_3$, as shown in Figures 14(a)–(c), which suggests that the metal cations in aqueous solutions of $AgNO_3$, H_2PtCl_6, and $HAuCl_4$ are reduced to Ag, Pt, and Au nanoparticles on the {100} facets by H_2O as the electron donor, as shown by the following equations:

$$\mathbf{Ag^{+} + e^{-} \rightarrow Ag} \qquad (2)$$

$$\mathbf{Au^{3+} + 3\ e^{-} \rightarrow Au} \qquad (3)$$

$$\mathbf{Pt^{4+} + 4\ e^{-} \rightarrow Pt} \qquad (4)$$

$$\mathbf{2H_2O \rightarrow 2O_2 + 4H^{+} + 4\ e^{-}} \qquad (5)$$

where Eqs. (2–4) show the reductions of metal ions and Eq. (5) shows the oxidation of water. Meanwhile, Figures 14(d)–(f) reveal that metal oxide nanoparticles (i.e., MnO_2, PbO_2, and Co_3O_4) are spatially located on the {110} facets when $NaIO_3$ was used as the hole donor, according to Eqs. (6–9):[35, 63]

$$\mathbf{Mn^{2+} + 2h^{+} + 2H_2O \rightarrow MnO_2 + 4H^{+}} \qquad (6)$$

$$\mathbf{3Co^{2+} + 3h^{+} + 4H_2O \quad \rightarrow \quad Co_3O_4 + 8H^{+}} \tag{7}$$

$$\mathbf{Pb^{2+} + 2h^{+} + 2H_2O \quad \rightarrow \quad PbO_2 + 4H^{+}} \tag{8}$$

$$\mathbf{IO_3^{-} + 4e^{-} + 6H^{+} \quad \rightarrow \quad I^{-} + 3H_2O} \tag{9}$$

where Eqs. (5–7) show metal-ion oxidation and Eq. (8) corresponds to the reduction of iodate.

The abovementioned results suggest that photogenerated electrons and holes selectively transfer to different facets of the photocatalyst because the electric fields within single photocatalyst particles are aligned;[11, 37] therefore, reductive and oxidative sites exist on different Al-$SrTiO_3$ facets. Table 3 summarizes the photocatalytic activities of various single-cocatalyst- and dual-cocatalyst-loaded Al-$SrTiO_3$ samples prepared by the PD method, which reveals that only the Ag metal nanoparticle cocatalyst exhibited good selectivity toward CO evolution (92.2%) by CO_2 reduction, even though the CO-formation rate was only 3.2 μmol h^{-1}. The Pt-, Au-, Co_3O_4-, MnO_2-, and PbO_2-loaded Al/$SrTiO_3$ only split water, with poor CO-evolution selectivities.

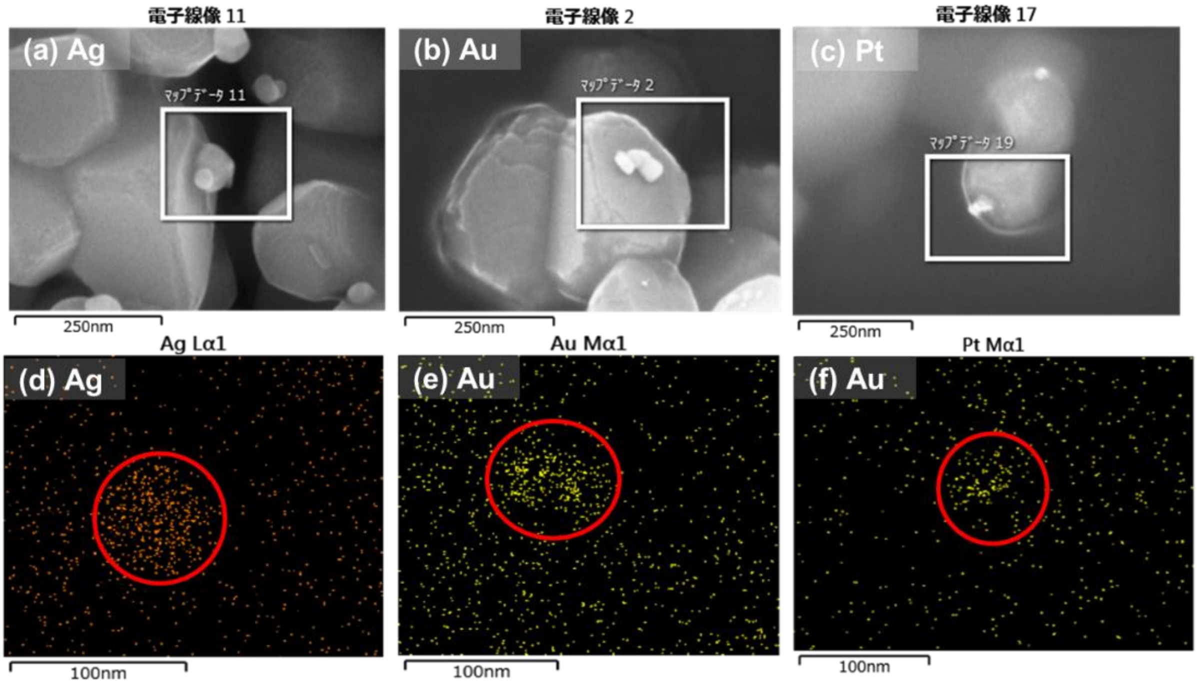

Figure 13. SEM images and EDS mappings of the different cocatalysts loaded Al-$SrTiO_3$ (a) and (d) Ag, (b) and (d) Au, (c) and (f) Pt.

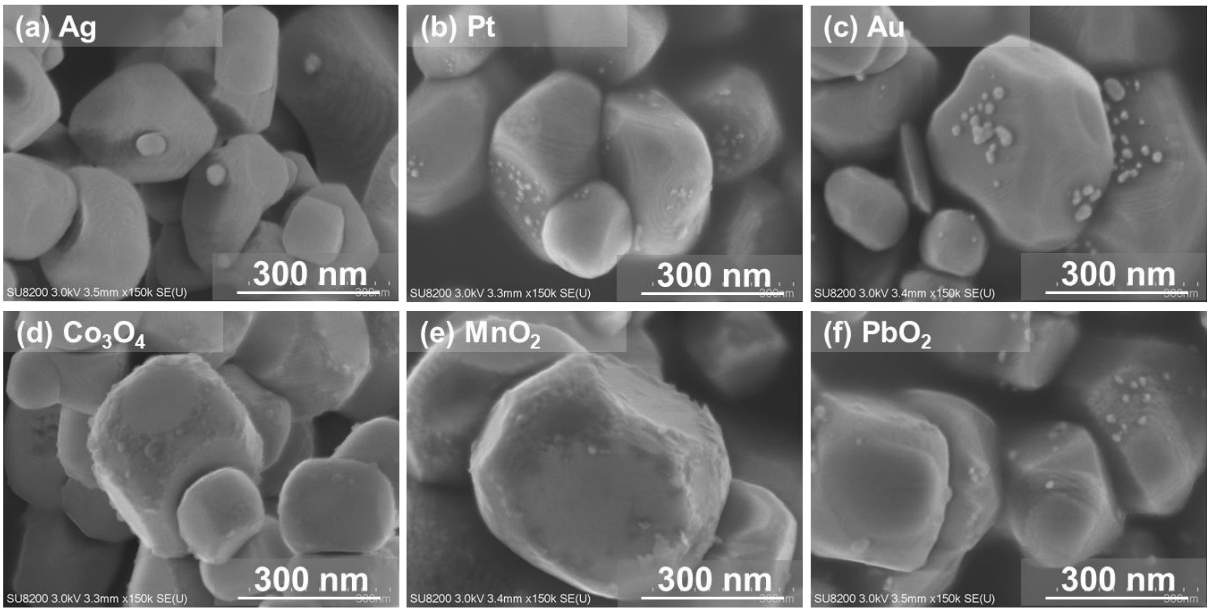

Figure 14. SEM images of various of cocatalyst-loaded Al-$SrTiO_3$ samples prepared by the PD method: (a) Ag, (b) Pt, (c) Au, (d) Co_3O_4, (e) MnO_2, and (f) PbO_2.

Table 3. Photocatalytic reduction of CO_2 into CO by H_2O over different cocatalyst loaded photocatalysts prepared by PD method [a]

Photocatalyst	**Formation rates of products (μmol h^{-1})**			**Selec. toward CO (%)**	**Consumed e^- /h+**
	H_2	**O_2**	**CO**		
Ag/Al-$SrTiO_3$	0.27	1.58	3.18	92.2	1.09
Pt/Al-$SrTiO_3$	96.7	48.9	0.00	0.00	0.99
Au/Al-$SrTiO_3$	17.2	8.52	0.25	1.43	1.02
MnO_2/Al-$SrTiO_3$	2.13	0.96	0.00	0.00	1.11
PbO_2/Al-$SrTiO_3$	Trace	Trace	Trace		
Co_3O_4/Al-$SrTiO_3$	9.28	4.92	0.04	0.47	0.95

[a] Photocatalytic reaction condition: 0.5g photocatalyst; 1.0 L $NaHCO_3$ (0.1 M) aqueous solution; 1.7 mol% Ag cocatalyst loading; 0.85 mol% Co cocatalyst loading; CO_2 flow (30 ml min^{-1}), 400 W high-pressure Hg lamp.

A possible mechanism for the photoreduction of CO_2 into CO over AgCo/Al-$SrTiO_3$_CR using H_2O as the reductant is depicted in Scheme 1. As mentioned above, different cocatalyst are spatially deposited on anisotropic facets, with Ag^+, Au^{3+}, and Pt^{4+} reduced and loaded onto smooth {100} facets, and Mn^{2+}, Co^{2+}, and Pb^{2+} oxidized and loaded on {110} facets. The author proposes that photogenerated electrons and holes are transferred to different Al-$SrTiO_3$ facets; therefore, reduction and oxidation occur at different facets.[35, 37] Even though the Ag and Co species were dispersed well on the surface of AgCo/Al-SrTiO3_CR, these Ag and Co were redeposited onto different crystal facets of the Al-$SrTiO_3$ during the photocatalytic reaction under photoirradiation as shown in Figure 4 and 5. Moreover, based on these results, CO_2 is photocatalytically converted into CO at Ag cocatalyst particles on the {100} facets of Al-$SrTiO_3$, whereas Co cocatalyst particles oxidize water on the {110} facets. Photocatalytic activity is significantly enhanced after dual cocatalyst loading because photogenerated electrons and holes move to different facets and are quickly captured by the Ag and Co cocatalysts, respectively.

Scheme 1. Plausible photoirradiation mechanisms: (a) cocatalyst loading by the PD method and (b) the photocatalytic conversion of CO_2 into CO over Al-$SrTiO_3$ modified with Ag and Co by the CR method using water as the reductant.

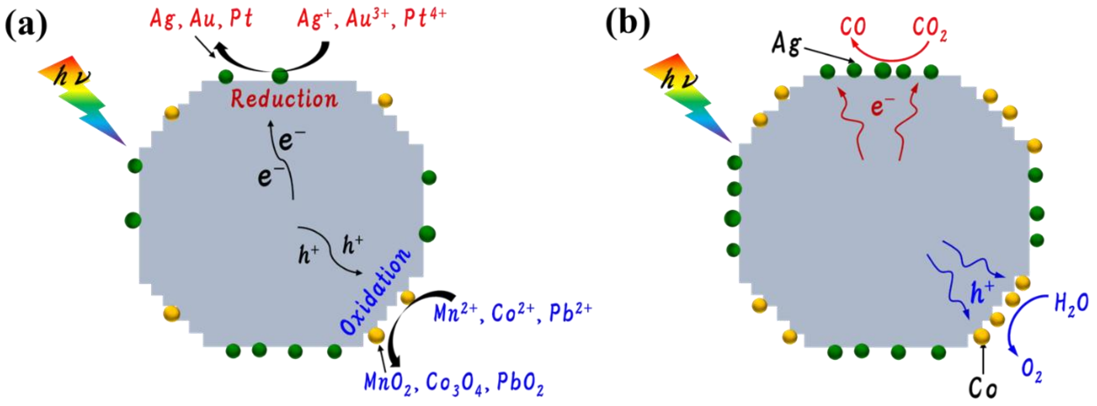

Conclusion

Loading Ag and Co onto Al-$SrTiO_3$ significantly improved its activity for the photocatalytic conversion of CO_2 by H_2O (as the electron donor), with extremely high selectivity toward CO evolution (99.8%), in which Ag and Co enable CO_2 reduction and H_2O oxidation on the Al-$SrTiO_3$

surface, respectively. A CO-evolution rate of up to 52.7 μmol h^{-1} was observed over AgCo/Al-$SrTiO_3$_CR when irradiated with light at wavelengths above 300 nm, which is ten-times higher than that observed for Ag/Al-$SrTiO_3$ (4.7 μmol h^{-1}). Furthermore, 7.4 μmol h^{-1} of CO gas was evolved when irradiated with LED light (365 nm), with a quantum efficiency of 0.03%. In addition, this study demonstrated that the reductive and oxidative sites are distributed on the {100} and {110} facets of Al-$SrTiO_3$, respectively. Therefore, photocatalytic CO_2 reduction and water oxidation occur separately on different Al-$SrTiO_3$ facets. Synergism between the Ag and Co dual cocatalysts effectively enhances the photocatalytic conversion of CO_2 over Al-$SrTiO_3$ with H_2O as the electron donor.

Reference

1. J. Yang; D. Wang; H. Han; C. Li, *Acc. Chem. Res.* **2013**, 46 (8), 1900-1909.
2. J. Ran; M. Jaroniec; S. Z. Qiao, *Adv. Mater.* **2018**, 30 (7), 1704649.
3. X. Chang; T. Wang; J. Gong, *Energy Environ. Sci.* **2016**, 9 (7), 2177-2196.
4. A. Kudo; Y. Miseki, *Chem. Soc. Rev.* **2009**, 38 (1), 253-278.
5. H. Abdullah; M. M. R. Khan; H. R. Ong; Z. Yaakob, *J. CO_2 Util.* **2017**, 22, 15-32.
6. R. Daghrir; P. Drogui; D. Robert, *Ind. Eng. Chem. Res.* **2013**, 52 (10), 3581-3599.
7. S. Trasatti, *J. Electroanal. Chem.* **1972**, 39 (1), 163-184.
8. K. Maeda; K. Teramura; N. Saito; Y. Inoue; K. Domen, *J. Catal.* **2006**, 243 (2), 303-308.
9. H. Kato; A. Kudo, *J. Phys. Chem. B* **2001**, 105 (19), 4285-4292.
10. X. Zong; H. Yan; G. Wu; G. Ma; F. Wen; L. Wang; C. Li, *J. Am. Chem. Soc.* **2008**, 130 (23), 7176-7177.
11. J. Zhu; S. Pang; T. Dittrich; Y. Gao; W. Nie; J. Cui; R. Chen; H. An; F. Fan; C. Li, *Nano Lett.* **2017**, 17 (11), 6735-6741.
12. K. Iizuka; T. Wato; Y. Miseki; K. Saito; A. Kudo, *J. Am. Chem. Soc.* **2011**, 133 (51), 20863-20868.
13. H. Nakanishi; K. Iizuka; T. Takayama; A. Iwase; A. Kudo, *ChemSusChem* **2017**, 10 (1), 112-118.

14. T. Takayama; K. Tanabe; K. Saito; A. Iwase; A. Kudo, *Phys. Chem. Chem. Phys.* **2014**, 16 (44), 24417-24422.

15. O. K. Varghese; M. Paulose; T. J. LaTempa; C. A. Grimes, *Nano Lett.* **2009**, 9 (2), 731-737.

16. S. Xie; Y. Wang; Q. Zhang; W. Deng; Y. Wang, *ACS Catal.* **2014**, 4 (10), 3644-3653.

17. T. Yui; A. Kan; C. Saitoh; K. Koike; T. Ibusuki; O. Ishitani, *ACS Appl. Mater. Interfaces* **2011**, 3 (7), 2594-2600.

18. K. Sayama; H. Arakawa, *J. Phys. Chem.* **1993**, 97 (3), 531-533.

19. P.-W. Pan; Y.-W. Chen, *Catal. Commun.* **2007**, 8 (10), 1546-1549.

20. I.-H. Tseng; W.-C. Chang; J. C. Wu, *Appl. Catal. B* **2002**, 37 (1), 37-48.

21. R. Pang; K. Teramura; H. Tatsumi; H. Asakura; S. Hosokawa; T. Tanaka, *Chem. Commun.* **2018**, 54 (9), 1053-1056.

22. T.-f. Xie; D.-j. Wang; L.-j. Zhu; T.-j. Li; Y.-j. Xu, *Mater. chem. phys.* **2001**, 70 (1), 103-106.

23. X. Zhu; A. Yamamoto; S. Imai; A. Tanaka; H. Kominami; H. Yoshida, *Chem. Commun.* **2019**, 13514-13517.

24. S. t. Neaţu; J. A. Maciá-Agulló; P. Concepción; H. Garcia, *J. Am. Chem. Soc.* **2014**, 136 (45), 15969-15976.

25. Q. Kang; T. Wang; P. Li; L. Liu; K. Chang; M. Li; J. Ye, *Angew. Chem. Int. Ed.* **2015**, 54 (3), 841-845.

26. C.-W. Tsai; H. M. Chen; R.-S. Liu; K. Asakura; T.-S. Chan, *J. Phys. Chem. C* **2011**, 115 (20), 10180-10186.

27. R. Pang; K. Teramura; H. Asakura; S. Hosokawa; T. Tanaka, *ACS Sustainable Chem. Eng.* **2018**, 7 (2), 2083-2090.

28. Q. Zhai; S. Xie; W. Fan; Q. Zhang; Y. Wang; W. Deng; Y. Wang, *Angew. Chem. Int. Ed.* **2013**, 52 (22), 5776-5779.

29. J. Yu; J. Low; W. Xiao; P. Zhou; M. Jaroniec, *J. Am. Chem. Soc.* **2014**, 136, 8839-8842.

30. H. Kato; K. Asakura; A. Kudo, *J. Am. Chem. Soc.* **2003**, 125, 3082-3089.

31. T. Ohno; K. Sarukawa; M. Matsumura, *New J. Chem.* **2002**, 26 (9), 1167-1170.

32. N. Murakami; Y. Kurihara; T. Tsubota; T. Ohno, *J. Phys. Chem. C* **2009**, 113 (8), 3062-3069.

33. T. Tachikawa; T. Ochi; Y. Kobori, *ACS Catal.* **2016**, 6 (4), 2250-2256.

34. R. Li; F. Zhang; D. Wang; J. Yang; M. Li; J. Zhu; X. Zhou; H. Han; C. Li, *Nat. Commun.* **2013**, 4, 1432.

35. L. C. Mu; Y. Zhao; A. L. Li; S. Y. Wang; Z. L. Wang; J. X. Yang; Y. Wang; T. F. Liu; R. T. Chen; J. Zhu; F. T. Fan; R. G. Li; C. Li, *Energy Environ. Sci.* **2016**, 9, 2463-2469.

36. Y. Ham; T. Hisatomi; Y. Goto; Y. Moriya; Y. Sakata; A. Yamakata; J. Kubota; K. Domen, *J. Mater. Chem. A* **2016**, 4, 3027-3033.

37. T. Takata; J. Jiang; Y. Sakata; M. Nakabayashi; N. Shibata; V. Nandal; K. Seki; T. Hisatomi; K. Domen, *Nature* **2020**, 581 (7809), 411-414.

38. H. Zhang; C. Guo; J. Ren; J. Ning; Y. Zhong; Z. Zhang; Y. Hu, *Chem. Commun.* **2019**, 55 (93), 14050-14053.

39. D. Kong; J. Xie; Z. Guo; D. Yang; J. Tang, *ChemCatChem* **2020**, 2708-2712.

40. X. Zhu; A. Yamamoto; S. Imai; A. Tanaka; H. Kominami; H. Yoshida, *Appl. Catal. B* **2020**, 119085.

41. Y. Bai; L. Ye; L. Wang; X. Shi; P. Wang; W. Bai, *Environ. Sci.: Nano* **2016**, 3 (4), 902-909.

42. Q. Liu; Y. Zhou; J. Kou; X. Chen; Z. Tian; J. Gao; S. Yan; Z. Zou, *J. Am. Chem. Soc.* **2010**, 132 (41), 14385-14387.

43. S. Wang; K. Teramura; T. Hisatomi; K. Domen; H. Asakura; S. Hosokawa; T. Tanaka, *ACS Appl. Energy Mater.* **2020**, 3, 1468-1475.

44. S. Wang; K. Teramura; T. Hisatomi; K. Domen; H. Asakura; S. Hosokawa; T. Tanaka, *ChemistrySelect* **2020**, 5 (28), 8779-8786.

45. Z. Wang; K. Teramura; S. Hosokawa; T. Tanaka, *J. Mater. Chem. A* **2015**, 3, 11313-11319.

46. Z. Wang; K. Teramura; S. Hosokawa; T. Tanaka, *Appl. Catal. B* **2015**, 163, 241-247.

47. K. Iwashina; A. Kudo, *J. Am. Chem. Soc.* **2011**, 133 (34), 13272-13275.

48. K. Teramura; T. Tanaka, *Phys. Chem. Chem. Phys.* **2018**, 20 (13), 8423-8431.

49. S. Kikkawa; K. Teramura; H. Asakura; S. Hosokawa; T. Tanaka, *J. Phys. Chem. C* **2018**, 122, 21132-21139.

50. Z. Huang; K. Teramura; H. Asakura; S. Hosokawa; T. Tanaka, *Catal. Today* **2018**, 300, 173-182.

51. R. Pang; K. Teramura; H. Asakura; S. Hosokawa; T. Tanaka, *Appl. Catal. B* **2017**, 218, 770-778.

52. A. Anzai; N. Fukuo; A. Yamamoto; H. Yoshida, *Catal. Commun.* **2017**, 100, 134-138.

53. G. Amatucci; J. Tarascon; D. Larcher; L. Klein, *Solid State Ionics* **1996**, 84 (3-4), 169-180.

54. M. W. Kanan; J. Yano; Y. Surendranath; M. Dinca; V. K. Yachandra; D. G. Nocera, *J. Am. Chem. Soc.* **2010**, 132 (39), 13692-13701.

55. M. Yoshida; T. Mineo; Y. Mitsutomi; F. Yamamoto; H. Kurosu; S. Takakusagi; K. Asakura; H. Kondoh, *Chem. Lett.* **2016**, 45 (3), 277-279.

56. D. Bazin; D. Sayers; J. Rehr; C. Mottet, *J. Phys. Chem. B* **1997**, 101 (27), 5332-5336.

57. K. Beppu; S. Hosokawa; T. Shibano; A. Demizu; K. Kato; K. Wada; H. Asakura; K. Teramura; T. Tanaka, *Phys. Chem. Chem. Phys.* **2017**, 19 (21), 14107-14113.

58. R. Chen; S. Pang; H. An; J. Zhu; S. Ye; Y. Gao; F. Fan; C. Li, *Nature Energy* **2018**, 3 (8), 655-663.

59. R. Nazir; P. Fageria; M. Basu; S. Pande, *J. Phys. Chem. C* **2017**, 121 (36), 19548-19558.

60. S. Navaladian; B. Viswanathan; T. Varadarajan; R. Viswanath, *Nanotechnology* **2008**, 19 (4), 045603.

61. H. Sakai; T. Kanda; H. Shibata; T. Ohkubo; M. Abe, *J. Am. Chem. Soc.* **2006**, 128 (15), 4944-4945.

62. K.-C. Lee; S.-J. Lin; C.-H. Lin; C.-S. Tsai; Y.-J. Lu, *Surf. Coat.Technol.* **2008**, 202 (22-23), 5339-5342.

63. J. Menze; B. Mei; P. Weide; M. Muhler, *J. Mater. Chem. A* **2017**, 5 (33), 17248-17252.

Chapter 4

Highly Selective Photocatalytic Conversion of Carbon Dioxide by Water over Al-$SrTiO_3$ Photocatalyst Modified with Silver-Metal Dual Cocatalysts

Abstract

In this study, an anisotropic facet-exposed Al-$SrTiO_3$ photocatalyst modified with various Ag-metal (Fe, Co, Ni, and Pt) dual cocatalysts was investigated to elucidate the functions of the Ag and metals in the photocatalytic conversion of CO_2 by H_2O. The various dual cocatalysts were loaded on the surface of Al-$SrTiO_3$ using a simultaneous photodeposition method. In particular, the modification of the FeOOH and metallic Ag cocatalysts on the surface of the Al-$SrTiO_3$ photocatalyst markedly enhanced the CO formation rate (38.2 μmol h^{-1}), with extremely high selectivity toward CO evolution (99.3%), during the photocatalytic conversion of CO_2 by H_2O under a relatively long light wavelength ($\lambda \geq 300$ nm). In addition, the metallic Ag and FeOOH dual cocatalysts present on the surface of Al-$SrTiO_3$ were durable and stable during the photo-irradiated reaction, wherein the Ag and Fe deposited on the {100} and {110} facets functioned as active sites for the reduction of CO_2 and oxidation of H_2O, respectively.

Introduction

In artificial photosynthesis, which is inspired from plant photosynthesis, CO_2 and H_2O are converted into chemicals and O_2 over a photocatalyst under sunlight irradiation. Since the pioneering work of Hamann [1] and Inoue [2] in the 1970s, the photocatalytic conversion of CO_2 into organic compounds by H_2O over a semiconductor catalyst has attracted significant attention. However, the presence of H_2O introduces an invariable competitive reaction because the potential of the hydrogen evolution reaction from water (H^+/H_2; -0.41 V vs NHE, pH 7) is more positive than that of CO_2 reduction (CO_2/CO; -0.51 V vs NHE, at pH 7). [3-4] In 2011, Kudo et. al reported that the photocatalytic reduction of CO_2 into CO occurs in priority to that of H_2O to H_2 over $Ag/ALa_4Ti_4O_{15}$ (A = Ca, Sr, and Ba) in aqueous solution. [5] Following this study, various semiconductor materials (e.g., $NaTaO_3$:Ba, [6] SrO/Ta_2O_5, [7] $CaTiO_3$, [8] $ZnGa_2O_6$, [9] $La_2Ti_2O_7$, [10] $Sr_2KTa_5O_{15}$, [11] $ZnTa_2O_6$, [12] $Sr_2ReKTa_5O_{15}$, [13] $ZnGa_2O_6/Ga_2O_3$, [14] $MgAl/Ga_2O_3$, [15] $SrNb_2O_6$, [16-17] $Na_2Ti_6O_{13}$, [18] and Rh-Ga_2O_3 [19]) modified with Ag as cocatalyst were reported as effective and selective heterogenous photocatalysts for CO_2 reduction in the photocatalytic conversion of CO_2 by H_2O in the gas-solid-liquid reaction system. [20] However, further research on how to improve the photocatalytic performance of CO_2 reduction is necessary to reduce the gap for industrial application. Thus, the design and development of a novel, effective, and abundant cocatalyst are imperative to increase the photocatalytic performance of CO_2 reduction.

The activity and selectivity of the photocatalytic conversion of CO_2 by H_2O have also been significantly improved by the simultaneous loading of a dual cocatalyst [21-28] on the surface of the photocatalyst. This is because a dual cocatalyst can mitigate the shortage of the monometallic cocatalyst by improving CO_2 chemisorption, [22] suppressing the backward reaction, [27, 29] and enhancing consumption of the photo-induced holes. [30-31] In addition, the presence of reductive and oxidative dual cocatalysts on the photocatalyst surface not only offers reductive and oxidative sites, respectively, but also promotes motion of the photogenerated electrons and holes to different active sites on the photocatalyst surface. [31-34] Indeed, the synergistic effect between the dual cocatalysts plays an effective role in enhancing the photocatalytic performance of the photocatalytic conversion of CO_2 by H_2O over semiconductor photocatalysts.

Fe-based materials offer a new opportunity to develop efficient, economical, and eco-friendly photocatalysts for the photocatalytic conversion of CO_2 by H_2O because of the abundance, nontoxicity, and high photo and heat stabilities of this group VIII metal. Particularly, α-Fe_2O_3 has been reported as a photocatalyst for water oxidation under visible-light photoirradiation. [35-36] In addition, studies of iron oxyhydroxide (FeOOH) as a material for catalytic water splitting are on the rise, because of its capability in improving O_2 evolution. [37-38] Moreover, very recently, FeOOH was reported as an effective and durable cocatalyst for photocatalytic and electrocatalytic overall water splitting under visible light irradiation. [39-40] However, to date, this compound has rarely been studied in the photocatalytic conversion of CO_2. With this mind, in this study, we investigated the effect of the Fe cocatalyst on the photocatalytic properties of Ag-Fe/Al-$SrTiO_3$ for the photocatalytic conversion of CO_2 by H_2O under photoirradiation. To the best of our knowledge, this has not been investigated before.

Experimental

Preparing of Al-$SrTiO_3$

Al-$SrTiO_3$ were fabricated according to the method described in a previous report. [41] Briefly, $SrTiO_3$ was prepared by a solid-state reaction (SSR) with $SrCO_3$ and TiO_2 as the metal sources. Next, Al was doped into $SrTiO_3$ via a flux method by calcinating a mixture of $SrTiO_3$, Al_2O_3, and $SrCl_2$ flux reagent at 1423 K, under air, for 15 h in an alumina crucible.

Loading of the dual cocatalysts

Various cocatalysts were employed to modify the surface of the as-prepared Al-$SrTiO_3$ catalyst using simultaneous photodeposition (SPD). Thus, 0.75g Al-$SrTiO_3$ was dispersed in deionized ultra-pure water (1000 mL), and $AgNO_3$ (0.695 mL, 0.1 M aq) and 0.347 mL (0.1 M aq) second metal source [e.g., H_2PtCl_6, Fe $(NO_3)_3$, $Co(NO_3)_2$, and $Ni(NO_3)_2$] were then added into the suspension. Next, the suspension was irradiated under Ar gas, which was bubbled into the suspension at a flow rate of 30 mL min^{-1}. For the irradiation, a 400 W high-pressure Hg lamp with a Pyrex® jacket connected to a water-cooling system was employed to cut off light at λ <300 nm. Subsequently, the suspension was vacuum-filtered and the collected photocatalyst (Ag-metal/Al-$SrTiO_3$) was dried at

298 K, overnight, under air. In addition, Al-$SrTiO_3$ samples comprising various amounts of loaded Ag and Fe were fabricated using the SPD method. These were labeled as Ag(*x*)-Fe(*y*)/Al-$SrTiO_3$, where *x* and *y* represent the molar ratios of Ag (0.0, 0.5, 1.0, 1.5, 1.7, 2.0, and 2.5 mol%) and Fe (0.0, 0.5, 0.85, 1.0, 1.3, and 1.7 mol%) to Ti in Al-$SrTiO_3$, respectively.

Characterization

The crystalline properties of $SrTiO_3$ and Al-$SrTiO_3$ were characterized by X-ray diffractometry (XRD) using an X-ray powder diffractometer (Rigaku, Multiflex, Japan equipped with a Cu Kα (λ = 0.154056 nm) radiation source operating at 30 kV and 30 mA. The absorption edge of the cocatalyst-loaded Al-$SrTiO_3$ was measured by UV-vis diffuse reflectance spectroscopy (UV-vis DRS) using a JASCO V-670 spectrometer equipped with an integrating sphere (Japan). Spectralon®, which was supplied by Labsphere Inc. (USA), was used as the standard reflection sample. The photocatalyst microstructure was observed using a scanning electron microscope (SEM, SU-8220, Hitachi High-Technologies, Japan) equipped with an energy dispersive X-ray spectroscopy (EDX) unit at an acceleration voltage of 15.0 kV. The loading amount of the cocatalyst was obtained by X-ray fluorescence spectroscopy (XRF; EDX-8000, Shimadzu Corp, Japan). In addition, Ag 3d and Fe 2p X-ray photoelectron spectra for the Ag-Fe/Al-$SrTiO_3$ photocatalyst were acquired using an X-ray photoelectron spectrometer (ESCA 3400, Shimadzu Corp., Japan).

Photocatalytic reaction

The photocatalytic conversion of CO_2 into CO using H_2O as an electron donor was performed in a CO_2 flowing batch system with an inner-irradiation-type reaction vessel at 298 K, under ambient pressure (101 kPa). Al-$SrTiO_3$ loaded with various cocatalysts (0.5 g) was dispersed in a $NaHCO_3$ aqueous solution (1.0 L, 0.1 M) and CO_2 gas (30 mL min^{-1}, 99.999%) was then bubbled into the suspension. After the air was purged out from the reactor, the suspension was irradiated using a 400 W high-pressure Hg lamp with a Pyrex® jacket connected to a water-cooling system to cut off any irradiation with $\lambda < 300$ nm. The photocatalytic gaseous products generated from the photoreaction system (H_2, O_2, and CO) were detected by thermal conductivity detector-gas chromatography (TCD-GC) using a GC-8A chromatograph (Shimadzu Corp., Japan) equipped with a 5A molecular sieve column with Ar as the carrier gas and by flame ionization detector-gas chromatography (FID-GC) using a methanizer and ShinCarbon ST column, with N_2 as the carrier gas.

Results and Discussion

The photocatalytic conversion of CO_2 into CO by H_2O over Ag/Al-$SrTiO_3$ and Ag-metal/Al-$SrTiO_3$ (metal = Fe, Co, Ni, and Pt) photocatalyst were performed in $NaHCO_3$ aqueous solution (1.0 L, 0.1 M) under photoirradiation at $\lambda \geq 300$ nm. Table 1 shows the formation rate of the H_2, O_2, and CO products, consumed ratio of $\boldsymbol{e^-/h^+}$, and selectivity toward CO evolution during the photocatalytic conversion of CO_2 by H_2O. Table 1 suggests that Ag-Fe/Al-$SrTiO_3$ exhibited the most excellent photocatalytic performance for the photocatalytic conversion of CO_2 by H_2O, with a significant CO formation rate (32.3 μmol h^{-1}) and extemly good selectivity toward CO evolution. Indeed, the CO generation rate over Ag-Fe/Al-$SrTiO_3$ was much higher than that over Ag/Al-$SrTiO_3$. Furthermore, the stoichiometric amount of O_2 evolution (Table 1) suggested that H_2O acted as an electron donor for the photocatalytic conversion of CO_2 into CO over the Al-$SrTiO_3$ photocatalyst modified with Ag and Fe cocatalysts. In addition, we carried out photocatalytic conversions of CO_2 by H_2O over Ag-metal/Al-$SrTiO_3$ (metal = Co, Ni, and Pt). In this case, H_2 was mainly observed over the Ag-Pt/Al-$SrTiO_3$ and Ag-Ni/Al-$SrTiO_3$ photocatalysts. Ag-Co/Al-$SrTiO_3$, afforded a good CO formation rate (second highest); however, the selectivity toward CO evolution was only 68.7%. These results indicated that the addition of the Fe cocatalyst significantly enhanced the photocatalytic activity of Ag.

Table 1. Photocatalytic conversion of CO_2 into CO by H_2O over different dual cocatalyst-modified photocatalysts [a]

Photocatalyst	**Formation rates of products (μmol h^{-1})**			**Consumed e^-/h^+**	**Selec. to CO (%)**
	H_2	**O_2**	**CO**		
Ag/Al-$SrTiO_3$	0.3	1.3	2.6	1.03	89.7
Ag-Fe/Al-$SrTiO_3$	0.3	17.5	32.3	0.93	99.0
Ag-Co/Al-$SrTiO_3$	11.2	18.8	24.6	0.95	68.7
Ag-Ni/Al-$SrTiO_3$	10.4	5.30	2.20	1.19	17.4
Ag-Pt/Al-$SrTiO_3$	10.2	3.00	0.00	1.68	0.0

[a] Photocatalyst: 0.5 g; cocatalyst loading amount: 1.7 mol% Ag, amount of cocatalyst (Pt, Fe, Co, and Ni): 0.85 mol%; reaction solution: 1.0 L, 0.1 M $NaHCO_3$; CO_2 flow rate: 30 mL min^{-1}; light source: 400 W high-pressure Hg lamp with a Pyrex® jacket to cut off light at λ <300 nm.

Figure 1 shows the XRD patterns of Al-$SrTiO_3$ and Al-$SrTiO_3$ modified with the Ag-metal (metal = Fe, Co, Ni, and Pt) dual cocatalysts. The peaks in the Ag-metal/Al-$SrTiO_3$ photocatalysts were similar to those observed for Al-$SrTiO_3$, most of which were assigned to the $SrTiO_3$ perovskite structure according to a previous study. [41] However, the peak appearing at 38.1° was assigned to metallic Ag (Reference ICSD 64706), as shown in the enlarged area in the range 36–40°. The presence of the second cocatalyst (Fe, Co, and Ni) did not influence the crystal structure of the Al-$SrTiO_3$ and Ag cocatalyst. In addition, no signals for the Fe, Co, and Ni species were detected because of the low amount and poor crystallinity.

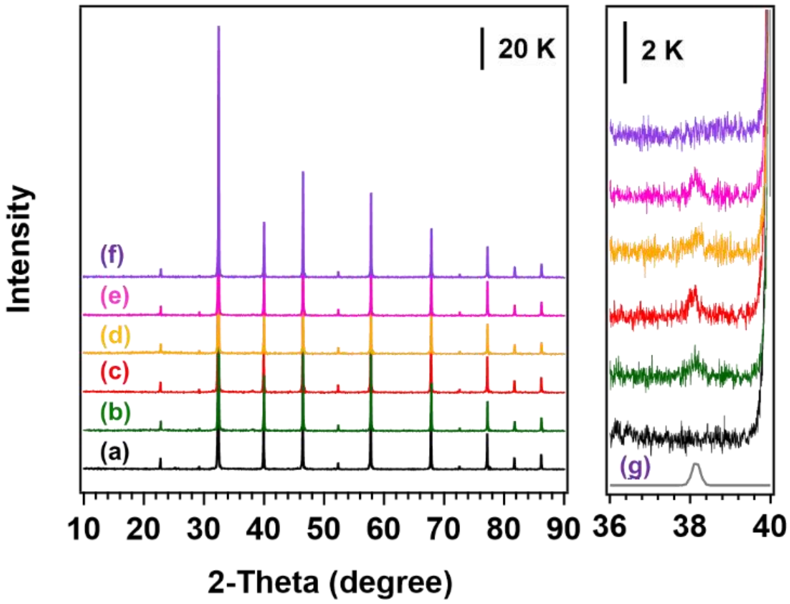

Figure 1. XRD patterns of (a) Al-$SrTiO_3$, (b) Ag/Al-$SrTiO_3$, (c) Ag-Fe/Al-$SrTiO_3$, (d) Ag-Co/Al-$SrTiO_3$, (e) Ag-Ni/Al-$SrTiO_3$, (f) Ag-Pt/Al-$SrTiO_3$, (g) Ag reference: ICSD 64706. Cocatalyst loading amount: 1.7 mol% Ag, cocatalyst (Pt, Fe, Co, and Ni) amount: 0.85 mol%.

The UV-vis DR spectra of Al-$SrTiO_3$ modified with Ag-metal cocatalysts are presented in

Figure 2. The absorption edge of Al-$SrTiO_3$ was acquired at approximately 390 nm, which corresponds to previously reported data [42-43] This did not change when Al-$SrTiO_3$ was modified with the different cocatalysts. Furthermore, broad absorption bands in the range 400–500 nm, which were assigned to the surface plasmon resonance (SPR) of the Ag nanoparticles, [44] were observed over the Ag and Ag-metal (metal: Fe, Co, and Ni) cocatalyst-modified Al-$SrTiO_3$, but not for Fe/Al-$SrTiO_3$ and Ag-Pt/Al-$SrTiO_3$.[45]

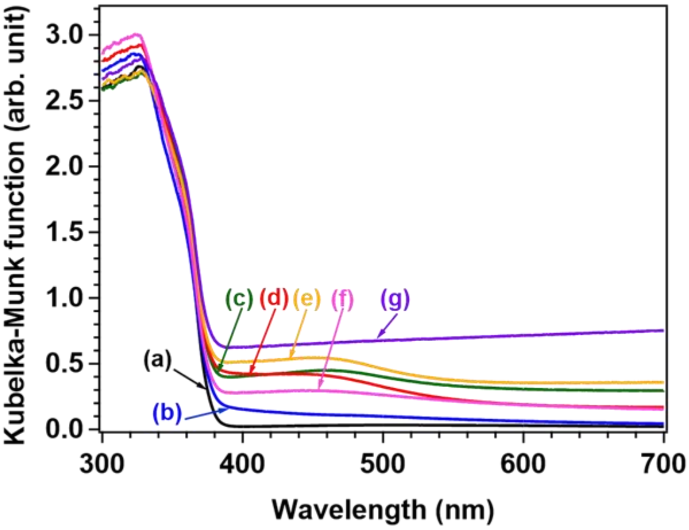

Figure 2. UV-Vis DR spectra of (a) Al-$SrTiO_3$, (b) Fe/Al-$SrTiO_3$, (c) Ag/Al-$SrTiO_3$, (d) Ag-Fe/Al-$SrTiO_3$, (e) Ag-Co/Al-$SrTiO_3$, (f) Ag-Ni/Al-$SrTiO_3$, (g) Ag-Pt/Al-$SrTiO_3$, Loading amount of the cocatalyst: 1.7 mol% Ag, the amount of cocatalyst Pt, Fe, Co, and Ni was 0.85 mol%.

The SEM images of Al-$SrTiO_3$ and Ag-metal/Al-$SrTiO_3$ were also acquired to investigate the microstructure of the as-synthesized photocatalysts (Figure 3). Cocatalyst nanoparticles were observed on the {100} facets of the Ag, Ag-Fe, Ag-Co, and Ag-Ni/Al-$SrTiO_3$ photocatalysts as shown in Figure 3(b, d–f), respectively. In addition, Ag-Fe, Ag-Co, and Ag-Ni/Al-$SrTiO_3$ displayed similar microstructures and morphologies. The EDX mappinng results in Figure S4 shows that the nanoparticles on the surface of Ag, Ag-Fe, Ag-Co, and Ag-Ni/Al-$SrTiO_3$ were assigned to elemental Ag. The second cocatalysts, such as Fe, Co, and Ni particles could not be clearly observed in the EDX mapping because of the low loading amount and high dispersion. The Ag-, Fe-, Co-, Ni-, and

Pt-to-Ti molar ratios at the different facets of the Ag-metal/Al-$SrTiO_3$ photocatalysts detected by EDX are summarized in Table 2. Interestingly, the Ag-to-second metal ratios (Ag/metal) in all the samples were approximately 2:1 over whole particles, indicating that stoichiometric ratios should be observed because the loading amounts of the Ag and metals were 1.7 and 0.85 mol%, respectively. On the other hand, the EDX data clearly indicated that the Ag/metal ratios were significantly changed on the different facets of Al-$SrTiO_3$. Thus, most of the Ag cocatalyst was located on the {100} facets, while the majority of the Fe, Co, and Ni elements were located on the {110} facet of Al-$SrTiO_3$. This is consistent with the results of our previous work, which suggested that the dual cocatalysts for the reduction and oxidation reactions were specifically loaded on the reductive and oxidative facets, respectively. [33-34, 41, 46] In addition, the nanoparticles on the {100} facets of Ag-Pt/Al-$SrTiO_3$ were assigned as Ag and Pt, which was confirmed by the EDX data (Table 2). The reduction of Ag^+ and Pt^{4+} occurred on the reduction sites under photoirradiation in aqueous solution.[47-48]

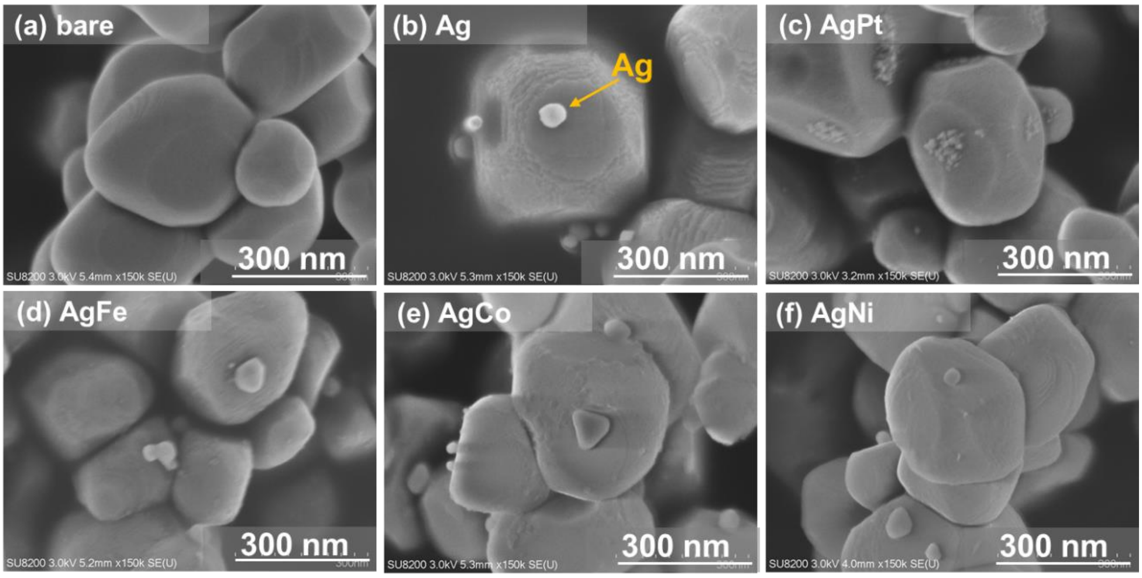

Figure 3. SEM images of Al-$SrTiO_3$ and various cocatalyst-modified Al-$SrTiO_3$ photocatalysts prepared by the PD method: (a) Al-SrTiO, (b) Fe/Al-$SrTiO_3$, (c) Ag-Pt/Al-$SrTiO_3$, (d) Ag-Fe/Al-$SrTiO_3$, (e) Ag-Co/Al-$SrTiO_3$, and (f) Ag-Ni/Al-$SrTiO_3$. Cocatalyst loading amount: 1.7 mol% Ag, amount of Pt, Fe, Co, and Ni cocatalyst: 0.85 mol%.

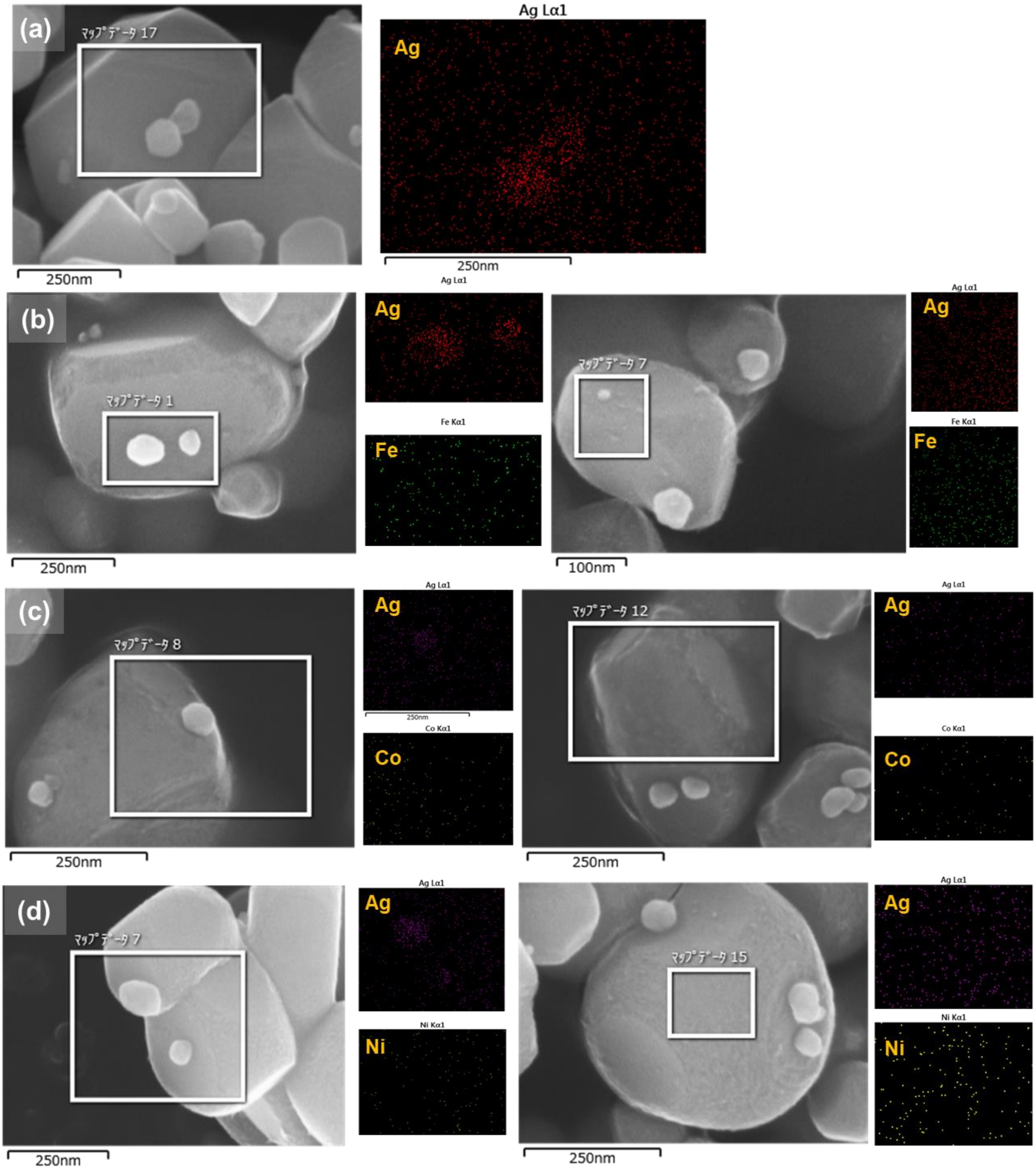

Figure 4. SEM images and EDX mapping of (a) Al-$SrTiO_3$, (b) Ag-Fe/Al-$SrTiO_3$, (c) Ag-Co/Al-$SrTiO_3$, (d) Ag-Ni/Al-$SrTiO_3$, Loading amount of the cocatalyst: 1.7 mol% Ag, the amount of cocatalyst Pt, Fe, Co, and Ni was 0.85 mol%.

Table 2. Cocatalyst-to-Ti molar ratios in the Ag-metal/Al-$SrTiO_3$ photocatalysts detected by EDX[b]

Samples	Ag/Ti	Metal[*]/Ti	Ag/Metal	Ag/Ti {100}	Metal/Ti {100}	Ag/Ti {110}	Metal/Ti {110}
Ag-Fe/Al-$SrTiO_3$	6.5	3.3	2.0 : 1.0	3.1	0.9	0.9	2.6
Ag-Co/Al-$SrTiO_3$	5.7	3.3	1.7 : 1.0	3.1	1.0	0.8	1.5
Ag-Ni/Al-$SrTiO_3$	4.8	2.4	2.0 : 1.0	3.4	1.7	0.0	0.7
Ag-Pt/Al-$SrTiO_3$	1.3	0.7	1.9 : 1.0	1.9	1.3	0.9	0

[b] Cocatalyst loading amount: 1.7 mol% Ag, Pt, Fe, Co, and Ni, cocatalyst amount: 0.85 mol%

[*] Fe, Co, Ni, and Pt

To determine the effect of the Ag and Fe cocatalysts on the photocatalytic conversion activity of CO_2 by H_2O, the photocatalytic performance over Al-$SrTiO_3$ modified with different amounts of Ag-Fe dual cocatalyst was next studied. Figure 5 shows the H_2, O_2, and CO formation rates and selectivity toward CO evolution for the photocatalytic conversion of CO_2 by H_2O under $\lambda \geq 300$ nm, over different loading amounts of Fe (Ag loading amount = 1.7 mol %) and Ag (Fe loading amount = 0.85 mol%). The formation rate of CO over Al-$SrTiO_3$ modified with a single Ag cocatalyst was only 2.6 μmol h^{-1} (Figure 5(a)). Importantly, the marginal loading amount of Fe significantly enhanced the activity of Al-$SrTiO_3$. The CO formation rate gradually increased as the Fe loading amount was increased from 0.0 to 0.85 mol%. However, with the further increase in the Fe loading amount (>0.85%), the formation rates of CO and O_2 were slightly decreased. Notably, very high and stable selectivity toward CO evolution (≥99.0%) was achieved in the Ag/Al-$SrTiO_3$ series with various amounts of Fe species. Thus, we supposed that the Ag cocatalyst is key to obtaining high selectivity toward CO evolution for the photocatalytic conversion of CO_2 by H_2O. On the other hand, Fe/Al-$SrTiO_3$, which was not modified with the Ag cocatalyst, only displayed activity for the overall water splitting process, with a low CO formation rate and poor selectivity toward CO evolution, even for the photocatalytic conversion of CO_2, at a saturated concentration, by H_2O (Figure 5(b)). The presence of the Ag cocatalyst significantly improved the CO formation rate, with very high selectivity (≥99.0%) toward CO evolution when the amount of Ag was increased from 0.0 to 2.0 mol%. Notably, the presence of excess Ag cocatalyst on the Al-$SrTiO_3$ surface negatively affected the photocatalytic activity, probably by blocking photocatalytic light absorption of the photocatalyst.

The best photocatalytic performance was obtained over Ag(2.0)-Fe(0.85)/Al-$SrTiO_3$, which was modified with 2.0 mol% Ag and 0.85 mol% Fe cocatalysts.

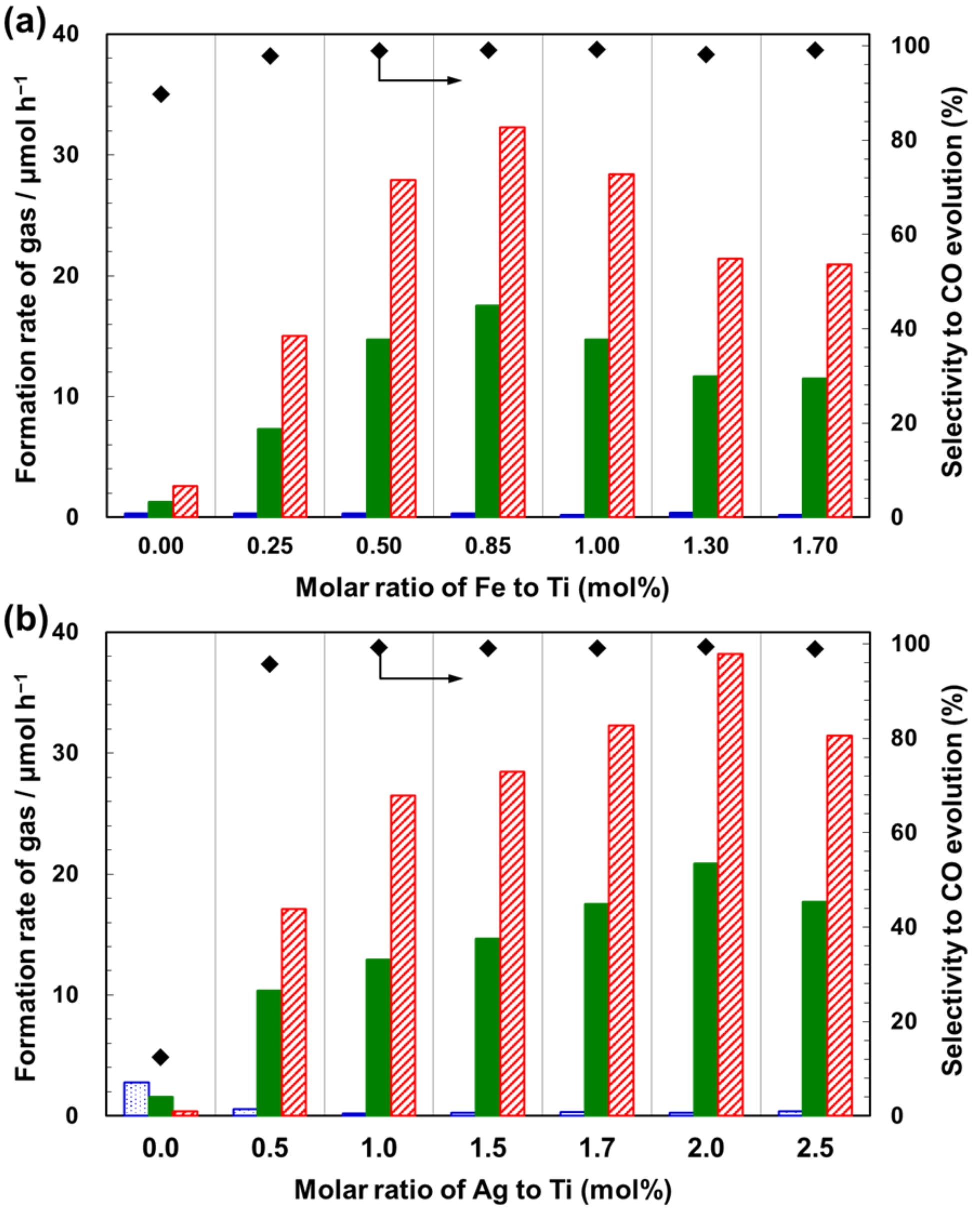

Figure 5. Formation rates of H_2 (blue), O_2 (green), and CO (red) and selectivity toward CO evolution (black diamonds) for the photocatalytic conversion of CO_2 by H_2O under irradiation over: (a) different loading amounts of Fe with a Ag loading amount of 1.7 mol% and (b) different loading amounts of Ag with an Fe loading amount of 0.85 mol%.

The durability is one of the main indicators used to evaluate the photocatalytic properties, as together with the conversion and selectivity, the lifetime of a catalyst is a key factor in the field of catalysis. Figure 6 shows the photocatalytic performance of Ag(2.0)-Fe(0.85)/Al-$SrTiO_3$ under photoirradiation (λ ≥300 nm) for three test recycles. The amounts of H_2, O_2, and CO increased linearly with photoirradiation time in every run, while the selectivity toward CO evolution ranged between 98.5 and 99.0% along the whole time course. Moreover, a stoichometric amount of O_2, the oxidation product of H_2O, was obseved during all three runs, indicating that the number of consumed electrons during reduction (H_2 and CO) was always equal to the number of holes consumed during oxidation (O_2).

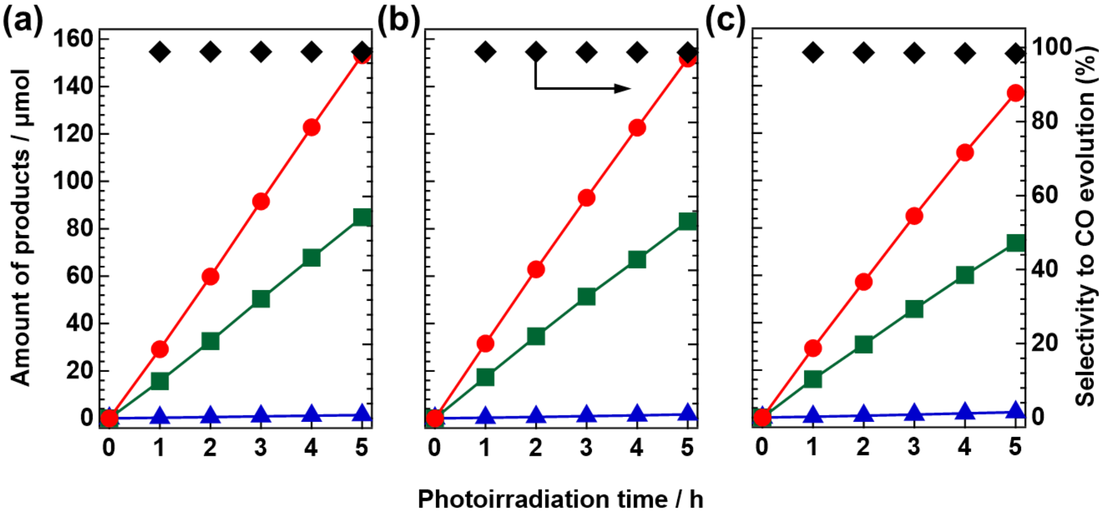

Figure 6. Time course of H_2 (blue triangles), O_2 (green squares), and CO (red circles) and selectivity toward CO evolution (black diamonds) during the photocatalytic conversion of CO_2 by H_2O over Ag(2.0)-Fe(0.85)/Al-$SrTiO_3$ during the: (a) first, (b) second, and (c) third runs.

As mentioned above, we observed that Ag(2.0)-Fe(0.85)/Al-$SrTiO_3$ displayed excellent photocatalytic activity and very good stability during the photocatalytic reaction. To verify the durability of the Ag(2.0)-Fe(0.85)/Al-$SrTiO_3$ photocatalyst, the cystalline structure and morphology of the used sample were elucidated from the XRD patterns and SEM image. Figure 7 shows the XRD partterns of the Ag(2.0)-Fe(0.85)/Al-$SrTiO_3$ photocatalyst before (a, red) and after (b, blue) photoirradiation, revealing that the crystal structure of Ag(2.0)-Fe(0.85)/Al-$SrTiO_3$ did not change after photoirradition. The peak at 38.1° was assigned to the Ag metal (ICSD 64706). The real loading amounts of the Ag and Fe cocatalysts estimated from the XRF data (Table S1), suggest that the charge amounts of Ag and Fe were totally loaded on the Al-$SrTiO_3$ surface. Figure 7 (c) presents the SEM image of Ag(2.0)-Fe(0.85)/Al-$SrTiO_3$ after photoirradiation for 15 h. It reveals that there were no significant changes in the microstructure and mophology of the photocatalyst after 15 h of photocatalytic reaction. Indeed, the Ag nanoparticles were still maintained on the {100} facet of Al-$SrTiO_3$, while the Fe species were well-dispersed on the {110} facet of Al-$SrTiO_3$. In addition, the Ag cocatalysts were slightly aggregated. The size of the Ag nanoparticles increased from 25–40 nm to 60–80 nm on the {100} facets of Al-$SrTiO_3$. In addition, the SPR absorption bands were slightly red-shifted after photocatalytic reaction (Figure 8), indicating that larger Ag nanoparticles were formed on the Al-$SrTiO_3$ surface. These results revealed that the photocatalytic performance was relatively stable, even though the crystal structure and mophology of the Ag-Fe cocatalyst slightly changed during the reaction.

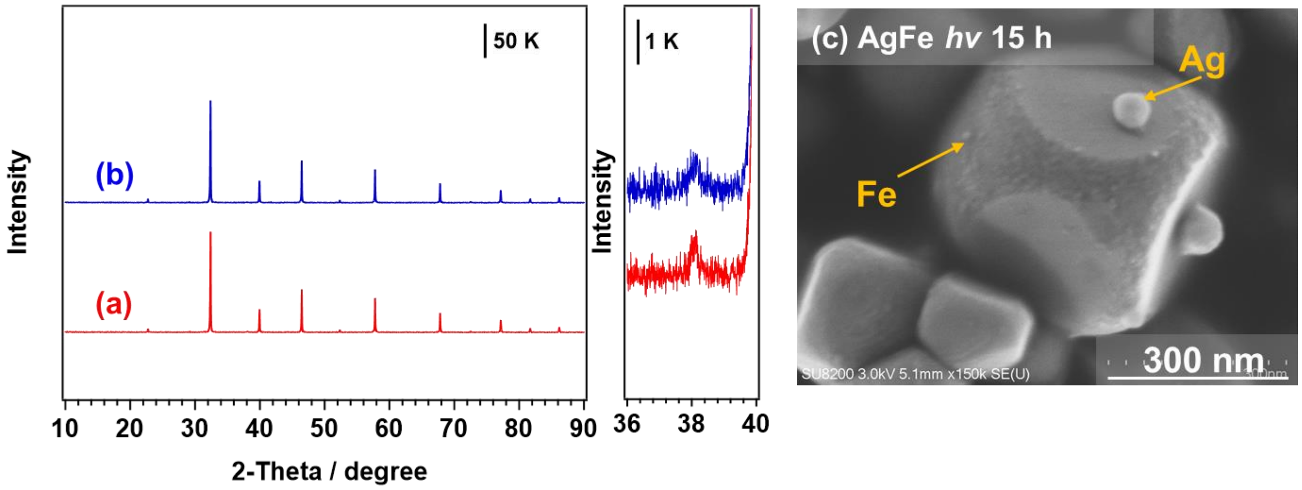

Figure 7. XRD partterns of the Ag(2.0)-Fe(0.85)/Al-$SrTiO_3$ photocatalyst (a) before (red) and (b) after (blue) photocatalytic reaction; (c) SEM image of the Ag(2.0)-Fe(0.85)/Al-$SrTiO_3$ photocatalyst after photocatalytic reaction

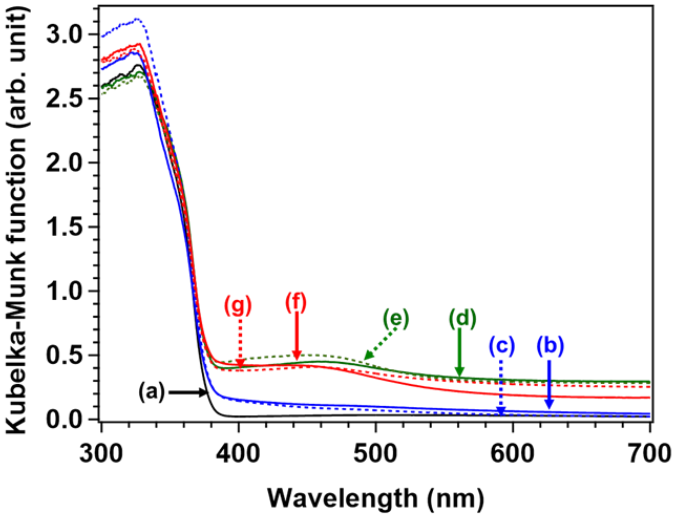

Figure 8. UV-Vis DR spectra of (a) Al-$SrTiO_3$, (b) and (c) Ag/Al-$SrTiO_3$, (d) and (e) Fe/Al-$SrTiO_3$, (f) and (g) Ag(2.0)-Fe(0.85)/Al-$SrTiO_3$, (c, e, g) after photocatalytic reaction.

To further investigate the chemical state of Ag and Fe in Ag(2.0)-Fe(0.85)/Al-$SrTiO_3$, the Ag 3d and Fe 2p X-ray photoelectron spectra were acquired, as shown in Figure 9(A) and (B), respectively. The binding energies in all the X-ray photoelectron spectraobtained in this study were normalized by the C 1s peak position (284.6 eV). The Ag 3d X-ray photoelectron spectra of Ag(2.0)-Fe(0.85)/Al-$SrTiO_3$ before and after 15 h photoirradiation were similar to that of Ag/Al-$SrTiO_3$ (Figure 9(A)). We previously reported that the Ag cocatalyst in Ag/Al-$SrTiO_3$, prepared by the PD method, was metallic Ag (Auger parameter). [49] In the current study, we concluded that the Ag cocatalyst in Ag(2.0)-Fe(0.85)/Al-$SrTiO_3$ before and after photocatalytic reaction was also metallic Ag. This corresponded to the previously discussed XRD patterns. The Fe 2p X-ray photoelectron spectra of Fe/Al-$SrTiO_3$ and Ag(2.0)-Fe(0.85)/Al-$SrTiO_3$ before and after 15 h photoirradiation are displayed in Figure 9(B). The Fe 2p spectrum after photoirradiation was near-identical to that before photoirradiation. Thus, both the Ag and Fe cocatalysts present on the surface of Al- $SrTiO_3$ were very stable during the photocatalytic conversion of CO_2 by H_2O and did not interact together. Figure 9(C) shows the Ag K-edge XANES spectra of Ag/Al-$SrTiO_3$ and Ag(2.0)-Fe(0.85)/Al-$SrTiO_3$ before and after 15 h photoirradiation together with those of Ag foil, AgO, and Ag_2O as references. Notably, the photon energies at the absorption edges and features of the Ag/Al-$SrTiO_3$, and Ag(2.0)-Fe(0.85)/Al-$SrTiO_3$ spectra were similar to those of Ag foil. [27, 31]

Therefore, we concluded that metallic Ag nanoparticles are highly dispersed on the {100} facet of Al-$SrTiO_3$ in Ag(2.0)-Fe(0.85)/Al-$SrTiO_3$. In addition, the Ag K-edge XANES spectrum of Ag(2.0)-Fe(0.85)/Al-$SrTiO_3$ after 15 h photoirradiation was consistent with those of the as-prepared Ag(2.0)-Fe(0.85)/Al-$SrTiO_3$ and Ag foil, indicating that the local structure around the Ag atom in Ag(2.0)-Fe(0.85)/Al-$SrTiO_3$ was stable during the photocatalytic reaction. Figure 9(D)–(F) shows the Fe K−edge XAFS spectra, including the XANES and EXAFS spectra, of Fe/Al-$SrTiO_3$ and Ag(2.0)-Fe(0.85)/Al-$SrTiO_3$ together with those of β-FeOOH, [50] α-FeOOH, [50] Fe_3O_4, α-Fe_2O_3, and FeO as references. The compounds α-FeOOH and β-FeOOH were synthesized according to a previous report, [50] and were confirmed using XRD patterns. The Fe K−edge XANES spectra of Fe/Al-$SrTiO_3$ and Ag(2.0)-Fe(0.85)/Al-$SrTiO_3$ were similar to those of β-FeOOH and α-FeOOH (Figure 9(D)). [51-52] Indeed, the XANES spectra of β-FeOOH, α-FeOOH, and Ag(2.0)-Fe(0.85)/Al-$SrTiO_3$ before and after 15 h photoirradiation overlapped (Figure 9(E)). Figure 9(F) indicates that the Fe K−edge EXAFS oscillation of Ag(2.0)-Fe(0.85)/Al-$SrTiO_3$ was approximately consistent with that of α-FeOOH rather than that of β-FeOOH. These results revealed that the metallic Ag and α-FeOOH on the surface of Al-$SrTiO_3$ were durable through the photocatalytic conversion of CO_2 under photoirradiation, as no significant changes were observed in the Ag(2.0)-Fe(0.85)/Al-$SrTiO_3$ photocatalyst before and after 15 h photoirradiation.

Ag was reported to serve as a good selective cocatalyst for CO evolution, and also acted as a reductive site during the photocatalytic reduction of CO_2.[5] Fe compounds such as FeOOH [39-40] have been reported to serve as cocatalysts for the oxidation of water under photoirradiation. As mentioned above, Fe/Al-$SrTiO_3$ only displayed activity for the overall water splitting reaction, while the CO formation rate was markedly increased in the presence of Ag. Moreover, all the Ag-Fe/$SrTiO_3$ photocatalysts exhibited a significantly higher CO formation rate than that observed with Ag/$SrTiO_3$, while maintaining the high selectivity toward CO evolution. Accordingly, we considered that the α-FeOOH in Ag-Fe/Al-$SrTiO_3$ promotes O_2 evolution. Moreover, the quick consumption of photogenerated holes by charge transfer not only reduced the recombination of the photoexcited electon/hole pair in the single photocatalyst particles, but also enhanced the utilization of the photoexcited electrons on the surface of the Ag cocatalyst. Thus, the presence of the Ag and α-FeOOH dual coatalyst significantly enhanced the photocatalytic activity of Al-$SrTiO_3$. In this case, Ag functioned as an active site for the CO evolution reaction, whereas α-FeOOH enhanced the O_2 evolution kinetics because it improved O_2 evolution from water.[37-38, 51]

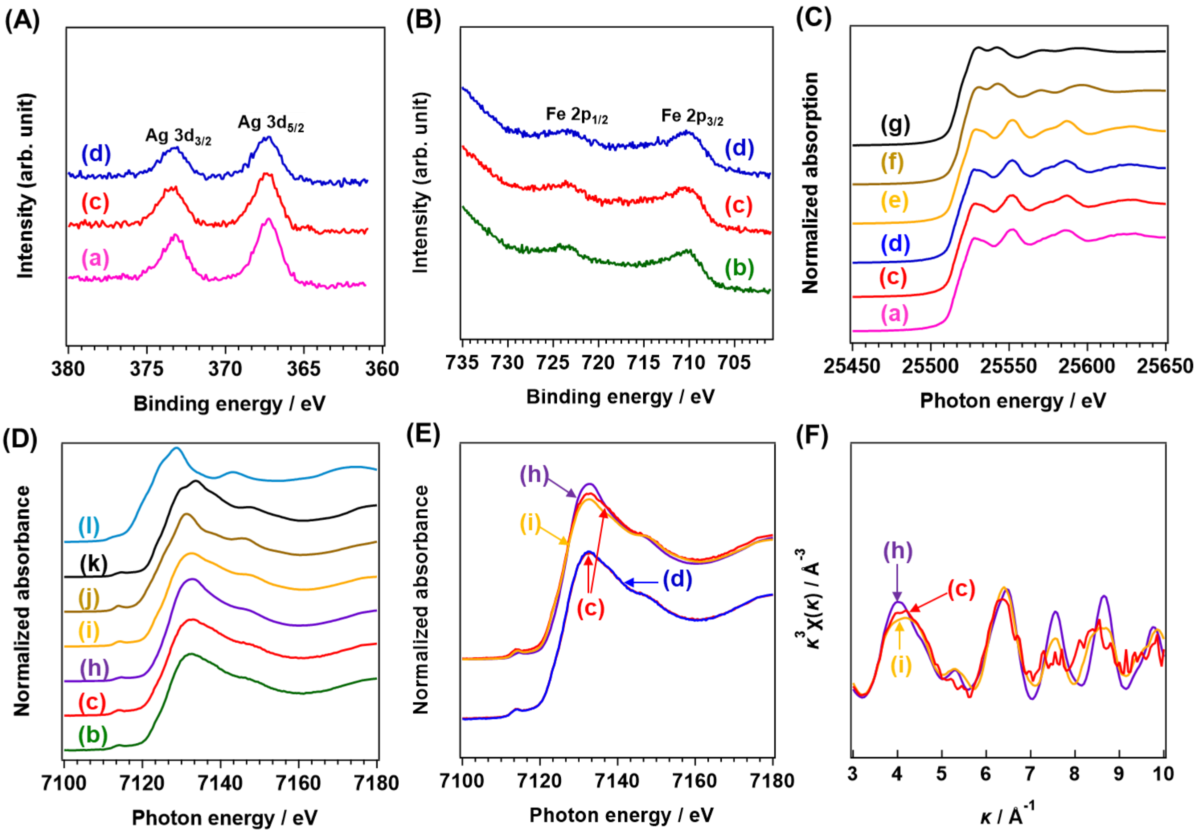

Figure 9. X-ray photoelectron spectra of (A) Ag 3d and (B) Fe 2p. (C) Ag K−edge XANES spectra, (D) and (E) Fe K-edge XANES spectra, and (F) Fe K−edge EXAFS oscillations. (a) Ag/Al-$SrTiO_3$, (b) Fe(0.85)/Al-$SrTiO_3$, (c) Ag(2.0)-Fe(0.85)/Al-$SrTiO_3$, (d) Ag(2.0)-Fe(0.85)/Al-$SrTiO_3$ after 15 h, (e) Ag foil, (f) AgO, (g) Ag_2O, (h) β-FeOOH, (i) α-FeOOH, (j) Fe_3O_4, (k) α-Fe_2O_3 , and (l) FeO

Conclusion

A second metal species (Fe, Co, or Ni) was deposited on the {110} facet of Al-$SrTiO_3$, which comprises unique {100} and {110} facets. Ag nanoparticles exhibiting activity for the reduction of CO_2 were selectively dispersed on the {100} facets. Among the second metal species, the addition of Fe species significantly improved the photocatalytic performance of Ag/Al-$SrTiO_3$ for the photocatalytic conversion of CO_2 by H_2O. Indeed, a CO formation rate of 38.2 μmol h^{-1} under light irradiation (λ ≥ 300 nm) with approximately 100% selectivity toward CO evolution over the optimized Ag(2.0)-Fe(0.85)/Al-$SrTiO_3$ was observed. The stoichiometric formation rate of O_2 was also observed in all reactions using an Ag-Fe dual cocatalyst, indicating that H_2O functions as an effective electron donor. The metallic Ag nanoparticles, which were unchanged before and after the reaction, stably functioned as CO_2 reduction sites. On the other hand, α-FeOOH, which was highly dispersed on the {110} facet accelerated the oxidation of H_2O into O_2. Active site separation for the reduction and oxidation reactions in Ag-Fe/Al-$SrTiO_3$ enhanced the photocatalytic activity of Al-$SrTiO_3$.

Reference

1. M. Halmann, *Nature* **1978**, 275 (5676), 115-116.
2. T. Inoue; A. Fujishima; S. Konishi; K. Honda, *Nature* **1979**, 277 (5698), 637-638.
3. P. S. Surdhar; S. P. Mezyk; D. A. Armstrong, *J. Phys. Chem.* **1989**, 93 (8), 3360-3363.
4. J. L. White; M. F. Baruch; J. E. Pander III; Y. Hu; I. C. Fortmeyer; J. E. Park; T. Zhang; K. Liao; J. Gu; Y. Yan, *Chem. Rev.* **2015**, 115, 12888-12935.
5. K. Iizuka; T. Wato; Y. Miseki; K. Saito; A. Kudo, *J. Am. Chem. Soc.* **2011**, 133 (51), 20863-20868.
6. H. Nakanishi; K. Iizuka; T. Takayama; A. Iwase; A. Kudo, *ChemSusChem* **2017**, 10 (1), 112-118.
7. K. Teramura; H. Tatsumi; Z. Wang; S. Hosokawa; T. Tanaka, *Bull. Chem. Soc. Jpn.* **2015**, 88, 431-437.
8. A. Anzai; N. Fukuo; A. Yamamoto; H. Yoshida, *Catal. Commun.* **2017**, 100, 134-138.
9. Z. Wang; K. Teramura; S. Hosokawa; T. Tanaka, *J. Mater. Chem. A* **2015**, 3, 11313-11319.
10. Z. Wang; K. Teramura; S. Hosokawa; T. Tanaka, *Appl. Catal. B* **2015**, 163, 241-247.
11. Z. Huang; K. Teramura; S. Hosokawa; T. Tanaka, *Appl. Catal. B* **2016**, 199, 272-281.
12. S. Iguchi; K. Teramura; S. Hosokawa; T. Tanaka, *Catal. Sci. Technol.* **2016**, 6 (13), 4978-4985.
13. Z. Huang; K. Teramura; H. Asakura; S. Hosokawa; T. Tanaka, *Catal. Today* **2018**, 300,

173-182.

14. Z. Wang; K. Teramura; Z. Huang; S. Hosokawa; Y. Sakata; T. Tanaka, *Catal. Sci. & Technol* **2016**, 6, 1025-1032.

15. S. Iguchi; Y. Hasegawa; K. Teramura; S. Kidera; S. Kikkawa; S. Hosokawa; H. Asakura; T. Tanaka, *Sustain. Energy Fuels* **2017**, 1 (8), 1740-1747.

16. R. Pang; K. Teramura; H. Asakura; S. Hosokawa; T. Tanaka, *Appl. Catal. B* **2017**, 218, 770-778.

17. R. Pang; K. Teramura; H. Asakura; S. Hosokawa; T. Tanaka, *ACS Appl. Energy Mater.* **2019**, 2 (8), 5397-5405.

18. X. Zhu; A. Anzai; A. Yamamoto; H. Yoshida, *Appl. Catal. B* **2019**, 243, 47-56.

19. S. Kikkawa; K. Teramura; H. Asakura; S. Hosokawa; T. Tanaka, *J. Phys. Chem. C* **2018**, 122, 21132-21139.

20. K. Teramura; T. Tanaka, *Phys. Chem. Chem. Phys.* **2018**, 20 (13), 8423-8431.

21. O. K. Varghese; M. Paulose; T. J. LaTempa; C. A. Grimes, *Nano Lett.* **2009**, 9 (2), 731-737.

22. S. Xie; Y. Wang; Q. Zhang; W. Deng; Y. Wang, *ACS Catal.* **2014**, 4 (10), 3644-3653.

23. S. t. Neaţu; J. A. Maciá-Agulló; P. Concepción; H. Garcia, *J. Am. Chem. Soc.* **2014**, 136 (45), 15969-15976.

24. Q. Kang; T. Wang; P. Li; L. Liu; K. Chang; M. Li; J. Ye, *Angew. Chem. Int. Ed.* **2015**, 54 (3), 841-845.

25. C.-W. Tsai; H. M. Chen; R.-S. Liu; K. Asakura; T.-S. Chan, *J. Phys. Chem. C* **2011**, 115 (20), 10180-10186.

26. Q. Zhai; S. Xie; W. Fan; Q. Zhang; Y. Wang; W. Deng; Y. Wang, *Angew. Chem. Int. Ed.* **2013**, 52 (22), 5776-5779.

27. R. Pang; K. Teramura; H. Tatsumi; H. Asakura; S. Hosokawa; T. Tanaka, *Chem. Commun.* **2018**, 54 (9), 1053-1056.

28. X. Yu; V. V. Ordomsky; A. Y. Khodakov, *ChemCatChem* **2020**, 12 (3), 740-749.

29. R. Pang; K. Teramura; H. Asakura; S. Hosokawa; T. Tanaka, *ACS Sustainable Chem. Eng.* **2018**, 7 (2), 2083-2090.

30. T.-f. Xie; D.-j. Wang; L.-j. Zhu; T.-j. Li; Y.-j. Xu, *Mater. chem. phys.* **2001**, 70 (1), 103-106.

31. X. Zhu; A. Yamamoto; S. Imai; A. Tanaka; H. Kominami; H. Yoshida, *Chem. Commun.* **2019**, 13514-13517.

32. X. Zhu; A. Yamamoto; S. Imai; A. Tanaka; H. Kominami; H. Yoshida, *Appl. Catal. B* **2020**, 119085.

33. J. Zhu; S. Pang; T. Dittrich; Y. Gao; W. Nie; J. Cui; R. Chen; H. An; F. Fan; C. Li, *Nano Lett.* **2017**, 17 (11), 6735-6741.

34. T. Takata; J. Jiang; Y. Sakata; M. Nakabayashi; N. Shibata; V. Nandal; K. Seki; T. Hisatomi; K. Domen, *Nature* **2020**, 581 (7809), 411-414.

35. T. K. Townsend; E. M. Sabio; N. D. Browning; F. E. Osterloh, *Energy Environ. Sci.* **2011**, 4 (10), 4270-4275.

36. J. Zhu; Z. Yin; D. Yang; T. Sun; H. Yu; H. E. Hoster; H. H. Hng; H. Zhang; Q. Yan, *Energy Environ. Sci.* **2013**, 6 (3), 987-993.

37. G. Elizarova; L. Matvienko; V. Kuznetsov; D. Kochubey; V. Parmon, *Journal of Molecular Catalysis A: Chemical* **1995**, 103 (1), 43-50.

38. T. Wang; Z. Jiang; K. H. Chu; D. Wu; B. Wang; H. Sun; H. Y. Yip; T. An; H. Zhao; P. K. Wong, *ChemSusChem* **2018**, 11 (8), 1365-1373.

39. G. Liu; J. Shi; F. Zhang; Z. Chen; J. Han; C. Ding; S. Chen; Z. Wang; H. Han; C. Li, *Angew. Chem. Int. Ed.* **2014**, 53 (28), 7295-7299.

40. J. A. Seabold; K.-S. Choi, *J. Am. Chem. Soc.* **2012**, 134 (4), 2186-2192.

41. S. Wang; K. Teramura; T. Hisatomi; K. Domen; H. Asakura; S. Hosokawa; T. Tanaka, *Chem. Sci.* **2021**, DOI: 10.1039/d1sc00206f.

42. Y. Ham; T. Hisatomi; Y. Goto; Y. Moriya; Y. Sakata; A. Yamakata; J. Kubota; K. Domen, *J. Mater. Chem. A* **2016**, 4, 3027-3033.

43. S. Wang; K. Teramura; T. Hisatomi; K. Domen; H. Asakura; S. Hosokawa; T. Tanaka, *ACS Appl. Energy Mater.* **2020**, 3, 1468-1475.

44. H. Sakai; T. Kanda; H. Shibata; T. Ohkubo; M. Abe, *J. Am. Chem. Soc.* **2006**, 128 (15), 4944-4945.

45. K.-C. Lee; S.-J. Lin; C.-H. Lin; C.-S. Tsai; Y.-J. Lu, *Surf. Coat.Technol.* **2008**, 202 (22-23), 5339-5342.

46. R. Li; H. Han; F. Zhang; D. Wang; C. Li, *Energy Environ. Sci.* **2014**, 7 (4), 1369-1376.

47. R. Li; F. Zhang; D. Wang; J. Yang; M. Li; J. Zhu; X. Zhou; H. Han; C. Li, *Nat. Commun.* **2013**, 4, 1432.

48. L. C. Mu; Y. Zhao; A. L. Li; S. Y. Wang; Z. L. Wang; J. X. Yang; Y. Wang; T. F. Liu; R. T. Chen; J. Zhu; F. T. Fan; R. G. Li; C. Li, *Energy Environ. Sci.* **2016**, 9, 2463-2469.

49. S. Wang; K. Teramura; T. Hisatomi; K. Domen; H. Asakura; S. Hosokawa; T. Tanaka, *ChemistrySelect* **2020**, 5 (28), 8779-8786.

50. M. Yang; Y. X. Li; M. Jiang; P. H. Li; S. H. Chen; J. H. Liu; C. H. Lin; X. J. Huang; W. Q. Liu, *Small* **2020**, 16 (7), 1906830.

51. M. Fracchia; A. Visibile; E. Ahlberg; A. Vertova; A. Minguzzi; P. Ghigna; S. Rondinini, *ACS Appl. Energy Mater.* **2018**, 1 (4), 1716-1725.

52. S. Wang; H. Lan; H. Liu; J. Qu, *Phys. Chem. Chem. Phys.* **2016**, 18 (14), 9437-9445.

Chapter 5

Effect of Zn in Ag-Loaded Zn-Modified $ZnTa_2O_6$ for Photocatalytic Conversion of CO_2 by H_2O

Abstract

Current environmental issues, such as global warming and the exhaustion of fossil fuels, call for innovative technologies. In this context, efficient photocatalysts that enable the selective reduction of CO_2 to CO in aqueous media are highly sought after. Although the beneficial use of Ag cocatalysts in $ZnTa_2O_6$-based photocatalytic systems has been previously studied, the CO evolution selectivity has remained moderate owing to the competing formation of H_2. Herein, the author reports that the modification of 3.0 wt% Ag-loaded $ZnTa_2O_6$ with 10 mol% Zn leads to a significant increase in the CO evolution selectivity to 90.0% while maintaining the rate of CO formation at 25.7 μmol h^{-1}. Thus, the modified Zn species play an important role in the suppression of the H_2 evolution. Although an Ag-less, Zn-modified photocatalyst performed relatively well, the combination of a Ag cocatalyst and Zn modifier is required to ensure CO evolution at a high selectivity and rate. Furthermore, full characterization of the Zn-modified photocatalysts allowed the proposal of two putative structures. In addition to serving as $ZnTa_2O_6$ surface modifiers, the Zn species may be incorporated in the $Zn/ZnTa_2O_6$ bulk. Finally, the author proposed that three types of active sites exist for (1) the reduction of CO_2 to CO, (2) the reduction of H^+ to H_2, and (3) the oxidation of H_2O to O_2.

Introduction

The conversion of sunlight into chemical energy is among the technologies with the potential to prevent the depletion of fossil fuels and the problem of global warming worldwide.[1-6] The photocatalytic conversion of CO_2 into useful chemicals has great potential to accomplish energy recycling and the fixation of superfluous atmospheric CO_2.[1, 7-10] Gas flowing reaction systems that contain a heterogeneous photocatalyst, H_2O as an adequate electron donor, and a CO_2 source have become favorable reaction systems for the photocatalytic conversion of CO_2 into useful chemicals using H_2O as a reductant under photoirradiation.[3, 9, 11-16] Moreover, CO is one of the most useful and convenient products of photocatalytic CO_2 reduction because it is easily separated from the reaction system and finds wide industrial application, for example in syngas. However, the development of reaction systems in which the reduction of CO_2 to CO competes with the production of H_2 in the presence of H_2O as an electron donor remains challenging because the H^+/H_2 reduction potential is more positive than that of CO_2/CO (−0.41 and −0.52 V vs NHE, respectively, at pH 7).[5, 17-18] Hence, the formation of H_2, which is often the major product, must be suppressed during the photocatalytic reduction of CO_2 by H_2O to enhance the selectivity toward CO evolution. In this context, Kudo et al.[12] reported that Ag-loaded $ALa_4Ti_4O_{15}$ (A represents Ca, Sr, and Ba) exhibited good selectivity in the conversion of CO_2 to CO using H_2O as the electron donor under photoirradiation. Subsequently, Ag nanoparticles were widely used as cocatalysts to improve the conversion and selectivity of the CO_2 reduction in similar reaction systems.[7, 14, 16, 19-28] The selectivity of CO generation ($\boldsymbol{S}_{\mathrm{CO}}$ (%)) and the balance of the consumed electron-hole pairs ($\boldsymbol{e^-/h^+}$) are calculated using eqs. (1) and (2), respectively:

$$\boldsymbol{S}_{\mathrm{CO}}\ (\%) = 2\boldsymbol{R}_{\mathrm{CO}}/(2\boldsymbol{R}_{\mathrm{CO}} + 2\boldsymbol{R}_{\mathrm{H2}}) \times 100 \qquad (1)$$

$$\boldsymbol{e^-/h^+} = (2\boldsymbol{R}_{\mathrm{CO}} + 2\boldsymbol{R}_{\mathrm{H2}}) / 4\boldsymbol{R}_{\mathrm{O2}} \qquad (2)$$

where $\boldsymbol{R}_{\mathrm{CO}}$, $\boldsymbol{R}_{\mathrm{H2}}$, and $\boldsymbol{R}_{\mathrm{O2}}$ represent the rates of CO, H_2, and O_2 formation during the photocatalytic reaction, respectively.

Previously, Iguchi et al. demonstrated the satisfactory performance of Ag-loaded $ZnTa_2O_6$ ($Ag/ZnTa_2O_6$) in the photoreduction of CO_2 by H_2O as the electron donor,[19] with 45.8% selectivity toward CO evolution. However, the main reduction product was H_2. To enhance the CO evolution selectivity to over 50%, thus rendering CO the major product, the modification of the photocatalyst's surface by Zn species is an attractive method. Zn-based materials, such as $ZnGa_2O_4$,[22, 29-30] Zn_2GeO_4,[31] and Cu_2O@$Zn_{1.8}Cr$ layered double hydroxide (LDH),[32] have been applied as photocatalysts for the reduction of CO_2 using H_2O as the electron donor. Regarding this process, the group of Kyoto University found that the performance of Zn-modified Ga_2O_3 with a Ag cocatalyst was superior to that of the bare Ga_2O_3 and that the Zn modification led to a remarkable improvement in CO selectivity.[14, 33] Presumably, the Zn species suppressed H_2 formation upon the overall water splitting during the photocatalytic conversion of CO_2 by H_2O.[14, 33] In addition, the author believes that the use of Zn to suppress the evolution of H_2 is advantageous because Zn has several attractive properties and is earth-abundant and inexpensive. Although the efficiency of the CO_2 photoreduction has been significantly enhanced over the last few decades, the industrial implementation of CO_2 fixation and reuse remains challenging. Hence, the design and development of novel and highly efficient catalysts for the photocatalytic conversion of CO_2 by H_2O is imperative. Inspired by the discussed prior findings, the author investigated the modification of 3.0Ag/$ZnTa_2O_6$ by Zn to improve its photocatalytic CO_2 reduction performance in this study.

Experimental section

Preparation of Zn/$ZnTa_2O_6$

$ZnTa_2O_6$ photocatalysts were fabricated using the method previously reported by us.[19] Additionally, $Zn_3Ta_2O_8$ was fabricated by adjusting the Zn:Ta molar ratio to 3:2 using the precursors $Zn(NO_3)_2$ and Ta_2O_5. The surface of the fabricated $ZnTa_2O_6$ was modified by Zn species using an impregnation (IMP) method. To this end, $ZnTa_2O_6$ powder (1 eq.) was dispersed into aqueous $Zn(NO_3)_2$ solutions (0.0, 2.5, 5, 10, 15, 20, and 40 mol% with respect to $ZnTa_2O_6$). The resulting suspensions were evaporated at 353 K with stirring. The obtained mixtures were thoroughly ground in an agate mortar and calcined at 1273 K for 2 h on air. Hereafter, the Zn-modified $ZnTa_2O_6$ is described as xZn/$ZnTa_2O_6$ (where x is the Zn molar ratio used in the procedure).

Ag cocatalyst loading

The Ag cocatalyst was loaded on the prepared Zn/$ZnTa_2O_6$ photocatalysts by the IMP, chemical reduction (CR), and photodeposition (PD) methods. Hereafter, Ag-loaded Zn/$ZnTa_2O_6$ is referred to as *y*Ag/Zn/$ZnTa_2O_6$, where *y* is the Ag cocatalyst loading (0.0, 0.5, 1.0, 1.5, 2.0, 3.0, and 4.0 wt%).

IMP method: Zn/$ZnTa_2O_6$ (0.7 g) and aqueous $AgNO_3$ (0.1 M, 2.0 mL) were added to deionized water (20 mL). The suspension was stirred at 353 K for 0.5 h. After evaporation (353 K), the powder was calcined at 725 K for 2 h on air.

CR method: Zn/$ZnTa_2O_6$ (0.7 g) was dispersed in deionized water (50 mL). Aqueous $AgNO_3$ (0.1 M, 2.0 mL) and NaH_2PO_2 (0.4 M, 2.0 mL) solutions were added to the suspension stepwise. The resulting mixture was stirred at 325 K for 1.5 h. The solid Ag-modified Zn/$ZnTa_2O_6$ was collected by filtration and washed with deionized water.

PD method: Zn/$ZnTa_2O_6$ (0.7 g) and aqueous $AgNO_3$ (0.1 M, 2.0 mL) were added to deionized water (1.0 L). The resulting mixture was purged with Ar gas for 1 h to remove the air from the system. Subsequently, the suspension was irradiated for 1 h using a high-pressure Hg lamp (400 W) with a quartz jacket connected to a water-cooling system under Ar bubbling.

Characterization

The obtained Ag/Zn/$ZnTa_2O_6$ samples were characterized by X-ray diffraction (XRD) using a Rigaku Ultima IV powder diffractometer equipped with a Cu Kα (λ = 0.154056 nm) radiation source at a 30-kV voltage and 30-mA current. Furthermore, the samples were analyzed by UV-vis diffuse reflectance spectroscopy (UV-vis DRS) on a JASCO V-670 spectrometer equipped with an integrating sphere. Spectralon® (Labsphere Inc.) was used as a standard reflection sample. Scanning electron microscopy (SEM) images were acquired using a field-emission scanning electron microscope (SU8220, Hitachi High-Technologies) equipped with an energy dispersive X-ray spectroscopy (EDS) unit (15.0 kV). Additionally, X-ray photoelectron spectroscopy (XPS) was performed using an X-ray photoelectron spectrometer (ESCA 3400, Shimadzu Corp.). Additionally, the X-ray absorption fine structure (XAFS) for the Zn K−edge and Ta L_{III}−edge was analyzed using the beamline BL01B1 of SPring-8.

Typical conditions for the photocatalytic reaction

The photoreduction of CO_2 by H_2O was performed in a CO_2 flowing batch system (As shown in Scheme S1 of Chapter 1) with an inner-irradiation-type reaction vessel at approximately 298 K and 100 kPa. The photocatalyst (0.5 g) was dispersed in an aqueous solution (0.1 M $NaHCO_3$, 1.0 L).

CO_2 gas (99.999%, 30 mL min^{-1}) was continuously bubbled through the mixture, which was irradiated using a high-pressure Hg lamp (400 W) with a quartz jacket connected to a water-cooling system. The gaseous products—H_2, O_2, and CO—generated in the photoreaction system were detected by gas chromatography with thermal conductivity detection (TCD-GC) on a GC-8A chromatograph (Molecular Sieve 5A column, Ar carrier gas, Shimadzu Corp.) and by gas chromatography with flame ionization detection (FID-GC; methanizer, ShinCarbon ST column, N_2 carrier gas, Shimadzu Corp.).

Results and discussion

Figure 1 shows the formation rate of the photocatalytic products H_2, O_2, and CO and the CO evolution selectivity of 3.0Ag/$ZnTa_2O_6$ modified with different amounts of Zn. The ratio $(2\boldsymbol{R}_{\mathbf{CO}} + 2\boldsymbol{R}_{\mathbf{H2}}) / 4\boldsymbol{R}_{\mathbf{O2}} = e^{-}/h^{+}$ was 1. In addition, no liquid products, such as HCOOH, HCHO, and CH_3OH, were detected by high-performance liquid chromatography (HPLC) analysis of the reaction solution after the photocatalytic processes. The CO evolution selectivity increased from 64% (Figure 1(a)) to approximately 90% upon modification with Zn (Figure 1(b-g)). Moreover, the observed formation of stoichiometric amounts of O_2 suggests that H_2O serves as an electron donor during the photocatalytic reaction. Furthermore, the CO formation rate of 3.0Ag/5.0Zn/$ZnTa_2O_6$ and 3.0Ag/10Zn/$ZnTa_2O_6$ was excellent (25.6 μmol h^{-1}, Figure 1(c-d)). However, modification with higher amounts of Zn (above 10%) led to a gradual decrease in the photocatalytic CO_2 reduction activity whereas the CO evolution selectivity was stable at 90%.

To investigate the structural changes resulting from the modification with Zn and their role in the consistently high selectivity for CO formation, the Ag/Zn/$ZnTa_2O_6$ catalysts were thoroughly characterized. Figure 2 shows the XRD patterns of the prepared catalysts. Regarding $ZnTa_2O_6$ (Figure 2(A)(a)), the observed Pnab (60) space group (ICSD no. 36289) was in accordance with previous reports.[19, 34] Further, most of the XRD peaks of the modified Zn/$ZnTa_2O_6$ catalysts were attributed to the $ZnTa_2O_6$ phase. The increase in the amount of Zn from 2.5 to 40 mol% did not cause the peaks to shift (Figure 2(B)), indicating that the Zn modification did not influence the crystal structure of $ZnTa_2O_6$. Thus, the Zn ion (0.074 nm) did not dope the $ZnTa_2O_6$ (Ta^{5+} 0.062 nm) crystal as predicted by Bragg's Law.[35] In contrast, the Zn species covered the surface of $ZnTa_2O_6$. Additionally, the XRD pattern for $Zn_3Ta_2O_8$ was also obtained as a reference. The peaks corresponding to the latter were observed in the patterns of the catalysts modified with at least 20 mol% Zn (Figure 2(A)(e-f)). Additionally, the unknown peak at 23.2°, which is visible in the patterns of catalysts with over 15 mol% Zn, was tentatively assigned to an unknown type of zinc tantalum oxide. Given the poor performance of $3.0Ag/Zn_3Ta_2O_8$ as a CO_2 conversion photocatalyst (8.2 μmol h^{-1} CO formation rate and 56.4% CO evolution selectivity, Figure 3), the author concluded that the lower photocatalytic CO_2 reduction activity of catalysts modified with over 15 mol% Zn was due to formation of a $Zn_3Ta_2O_8$ layer on the surface of $ZnTa_2O_6$.

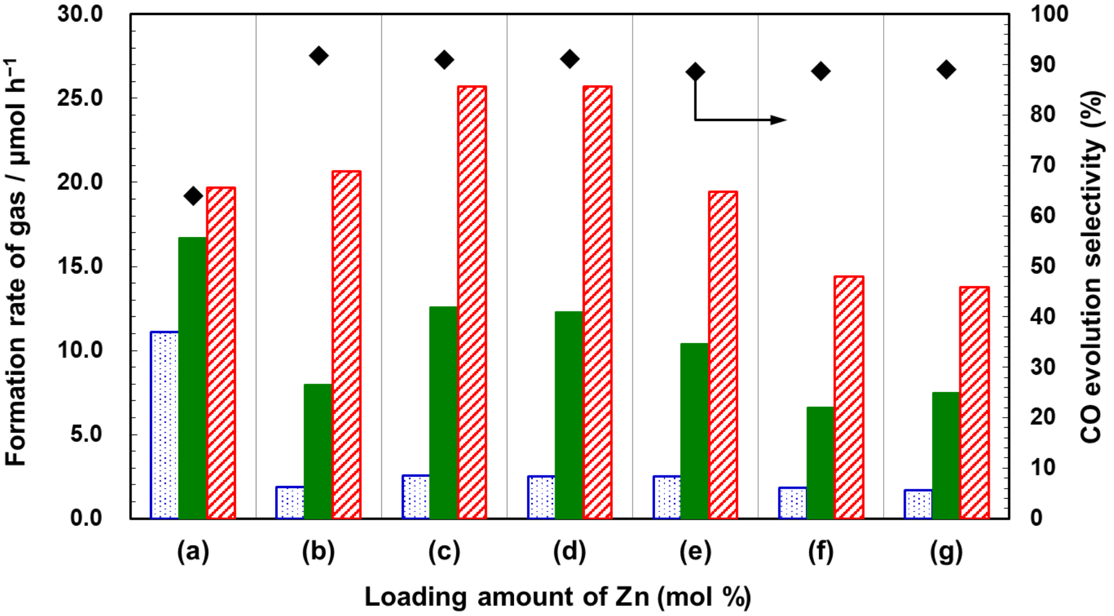

Figure 1. Formation of the photocatalytic products H_2 (blue dotted), O_2 (green filled), and CO (red slashed) and CO evolution selectivities (black ♦) over 3.0Ag-loaded (a) $ZnTa_2O_6$; (b) $2.5Zn/ZnTa_2O_6$; (c) $5Zn/ZnTa_2O_6$; (d) $10Zn/ZnTa_2O_6$; (e) $15Zn/ZnTa_2O_6$; (f) $20Zn/ZnTa_2O_6$; and (g) $40Zn/ZnTa_2O_6$.

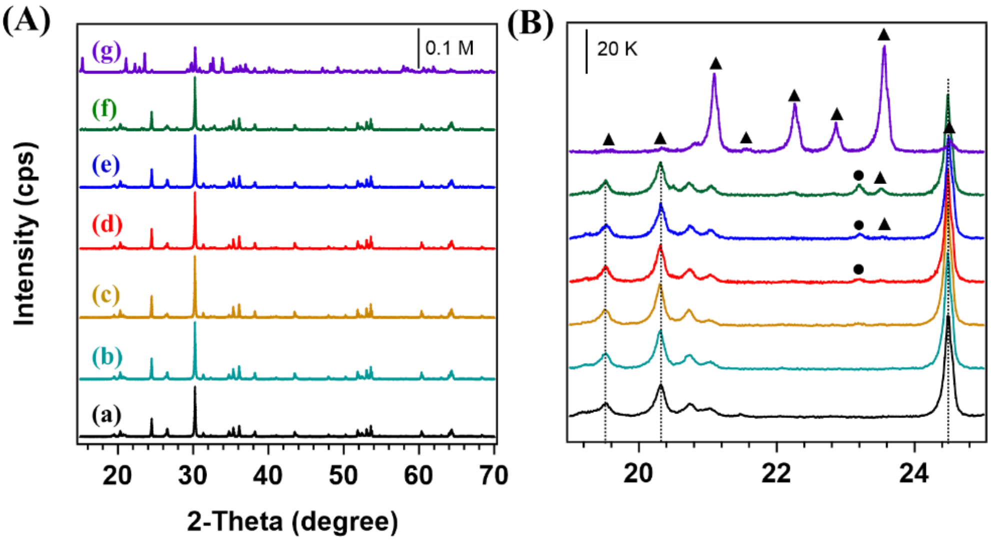

Figure 2. (A) XRD patterns of (a) $ZnTa_2O_6$; (b) 2.5Zn/$ZnTa_2O_6$; (c) 10Zn/$ZnTa_2O_6$; (d) 15Zn/$ZnTa_2O_6$; (e) 20Zn/$ZnTa_2O_6$; (f) 40Zn/$ZnTa_2O_6$; and (g) $Zn_3Ta_2O_8$. (B) Expansion of the 19–25° region (▲ $Zn_3Ta_2O_8$ phase, ● unknown).

The UV-vis spectra of the $ZnTa_2O_6$-based catalysts are shown in Figure 4. The absorption edge of $ZnTa_2O_6$ was located at approximately 270 nm in accordance with previous reports.[19, 34] Additionally, the absorption edge wavelengths of the Zn-modified $ZnTa_2O_6$ catalysts were similar to that of $ZnTa_2O_6$. Furthermore, the catalysts modified with more than 10% Zn exhibited a broad absorption peak at approximately 370 nm (Figure 4(c-f)), which is similar to that observed in the spectrum of $Zn_3Ta_2O_8$ (Figure 4(g)). Moreover, the UV-vis spectra of 10Zn/$ZnTa_2O_6$ and 3.0Ag/10Zn/$ZnTa_2O_6$ (Figure 5) feature a broad absorption at a long wavelength, which presumably stems from the plasmonic absorption of the Ag nanoparticles on the surface of the catalysts.[36-38] Further, the SEM images of the various Zn/$ZnTa_2O_6$ catalysts revealed that their morphology and microstructure did not change significantly upon modification with Zn (Figure 6).

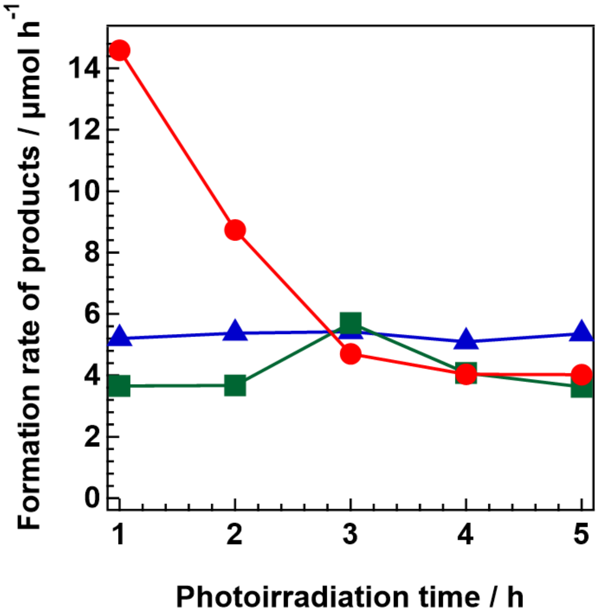

Figure 3. Time-dependent evolution of H_2 (triangle), O_2 (square), and CO (circle) 3.0Ag/ $Zn_3Ta_2O_8$

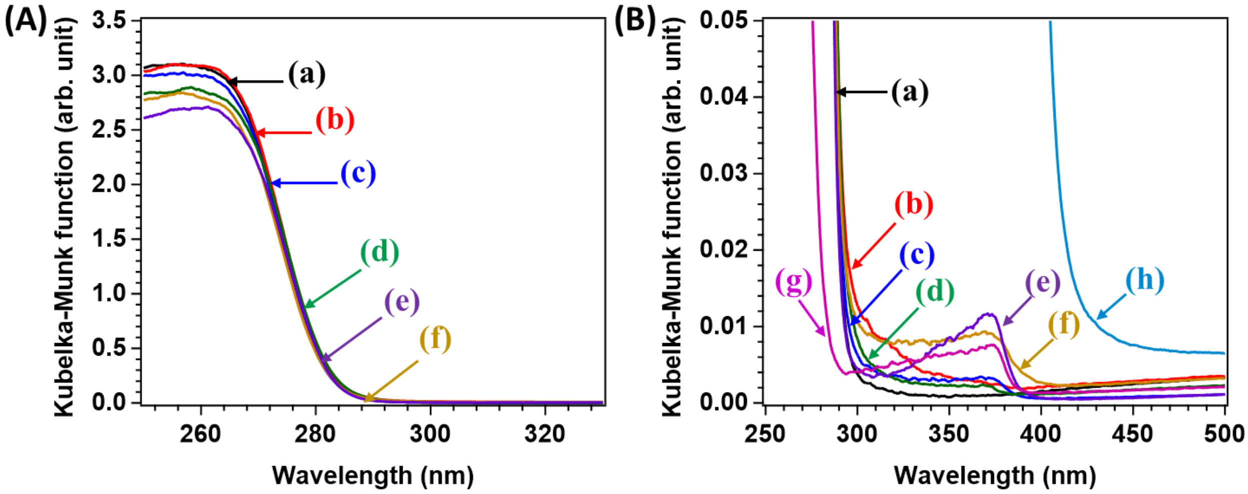

Figure 4. UV-vis spectra of (a) $ZnTa_2O_6$, (b) 2.5Zn/$ZnTa_2O_6$, (c) 10Zn/$ZnTa_2O_6$, (d) 15Zn/$ZnTa_2O_6$, (e) 20Zn/$ZnTa_2O_6$, (f) 40Zn/$ZnTa_2O_6$, (g) $Zn_3Ta_2O_8$, (h) ZnO

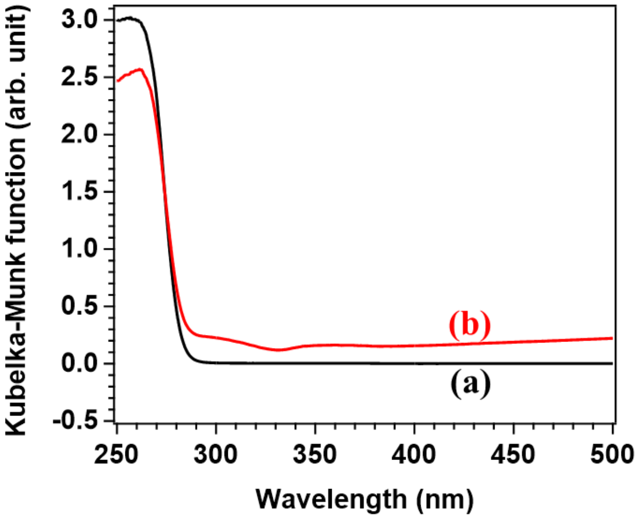

Figure 5. UV-vis spectra of (a) $10Zn/ZnTa_2O_6$; (b) $Ag/10Zn/ZnTa_2O_6$

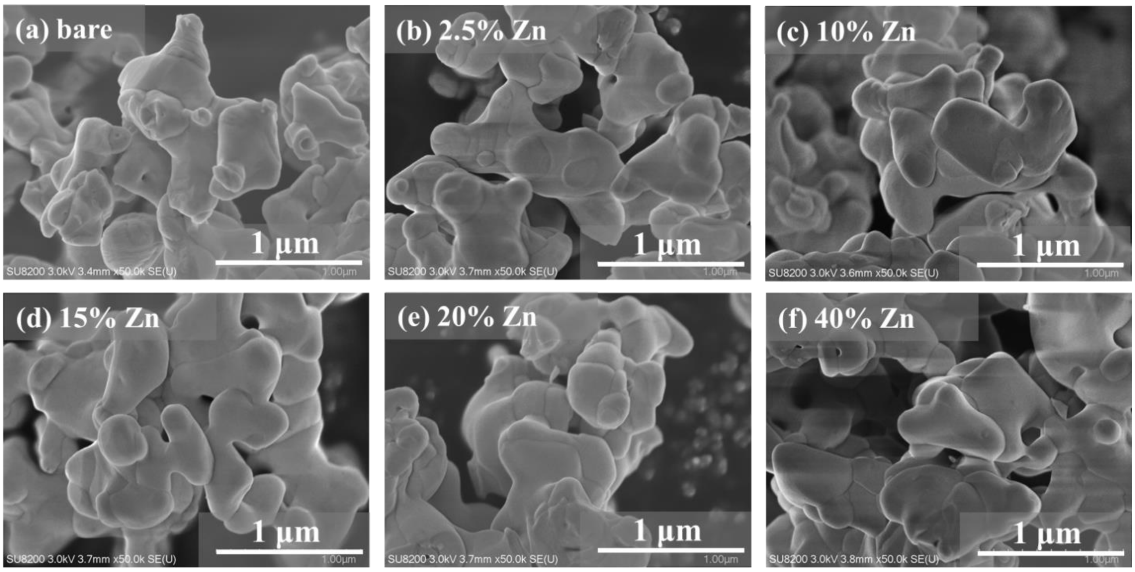

Figure 6. SEM images of the (a) $ZnTa_2O_6$, (b) $2.5Zn/ZnTa_2O_6$, (c) $10Zn/ZnTa_2O_6$, (d) $15Zn/ZnTa_2O_6$, (e) $20Zn/ZnTa_2O_6$, (f) $40Zn/ZnTa_2O_6$,

The X-ray photoelectron spectra of Zn 2p and Ta 4f, depicted in Figure 7, were calibrated using the C 1s peak (284.6 eV, Figure 8). The Zn $2p_{3/2}$ and Zn $2p_{1/2}$ peaks of ZnO were observed at 1021.8 and 1045.0 eV, respectively (Figure 7(A)) and were similarly located in the spectra of $ZnTa_2O_6$, $10Zn/ZnTa_2O_6$ (before and after calcination), $Zn_{1.1}Ta_2O_6$, and $Zn_3Ta_2O_6$. Thus, the Zn species of

10Zn/$ZnTa_2O_6$ are divalent cations (Zn^{2+}). In Figure 7(B), the peaks of the $ZnTa_2O_6$ catalyst located at 26.1 and 27.9 eV were attributed to Ta $4f_{7/2}$ and Ta $4f_{5/2}$, respectively. The Ta 4f peaks of noncalcinated 10Zn/$ZnTa_2O_6$ were detected at similar binding energies as those of $ZnTa_2O_6$. However, the corresponding 10Zn/$ZnTa_2O_6$ peaks shifted to slightly lower energy values, whereas those of $Zn_3Ta_2O_8$ underwent a larger shift. Previous reports state that the increase in the average electronegativity of the ligand leads to an increase in the binding energy of the ion.[39-40] Figure 8 shows that the O 1s peaks of 10Zn/$ZnTa_2O_6$ and $Zn_3Ta_2O_8$ are red-shifted relative to those of $ZnTa_2O_6$. Such a shift of the O 1s binding energy indicates a change in the oxide bonds as the binding energy reflects the electron cloud density of the O orbital.[40-41] Thus, the observed changes in the Ta and O ion binding energies presumably correlate to the incorporation of Zn into the $ZnTa_2O_6$. The Zn:Ta ratios of $ZnTa_2O_6$, 10Zn/$ZnTa_2O_6$, 3.0Ag/10Zn/$ZnTa_2O_6$, and $Zn_3Ta_2O_8$ are listed in Table 1. The Zn:Ta ratio of Zn/$ZnTa_2O_6$ determined by XPS is significantly higher than that obtained by EDS mapping; therefore, the author conclude that most of the modified Zn species exists on the surface of the photocatalyst.[42]

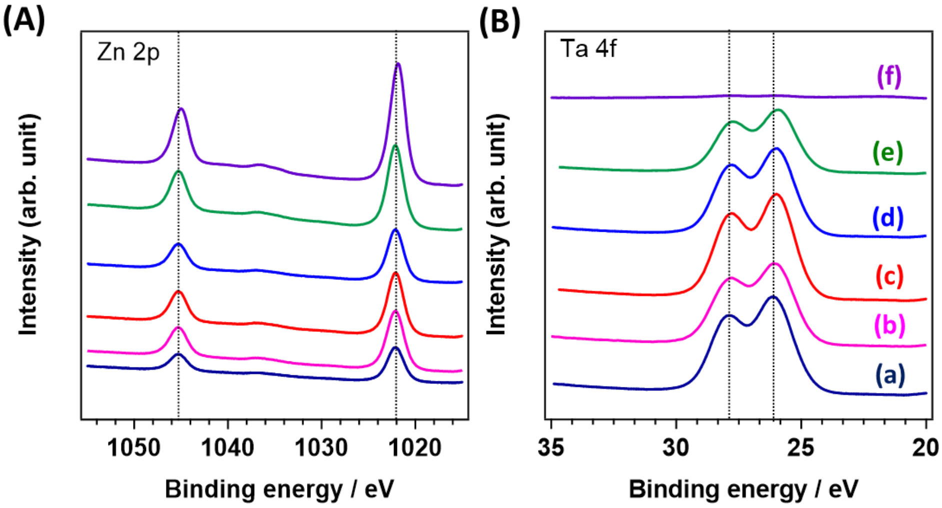

Figure 7. (A) Zn 2p and (B) Ta 4f binding energies of (a) $ZnTa_2O_6$; (b) noncalcinated 10Zn/$ZnTa_2O_6$; (c) calcinated 10Zn/$ZnTa_2O_6$; (d) $Zn_3Ta_2O_8$; and (e) ZnO, as determined by XPS analysis.

Additionally, the local structure of the Zn species in the Zn/$ZnTa_2O_6$ catalysts was examined by XAFS measurements. The Zn K−edge X-ray absorption near edge structure (XANES) data of different zinc compounds, including the reference samples Zn foil, ZnO, $ZnTa_2O_6$, and $Zn_3Ta_2O_6$, are presented in Figure 9. The Zn K−edge XANES spectra of $Zn/ZnTa_2O_6$ were similar to that of $ZnTa_2O_6$, regardless of the amount of modified Zn (2.5–40 mol% range). Furthermore, the Ta L_{III}−edge XANES data of the $Zn/ZnTa_2O_6$ catalysts were also consistent with that of $ZnTa_2O_6$ (Figure 9(B)). However, the increase in the amount of modified Zn from 2.5 to 40 mol% led to a decrease in the intensity of the Zn K−edge XANES spectra feature peak and in the adsorption edge energy (Figures 9(C) and 9(D), respectively). Importantly, the adsorption edge energy correlates with the valence state of the detected elements. Hence, the regular shift of the adsorption edge energy of catalysts modified with different amounts of Zn indicates changes in the local structure surrounding the Zn ions.[43-44]

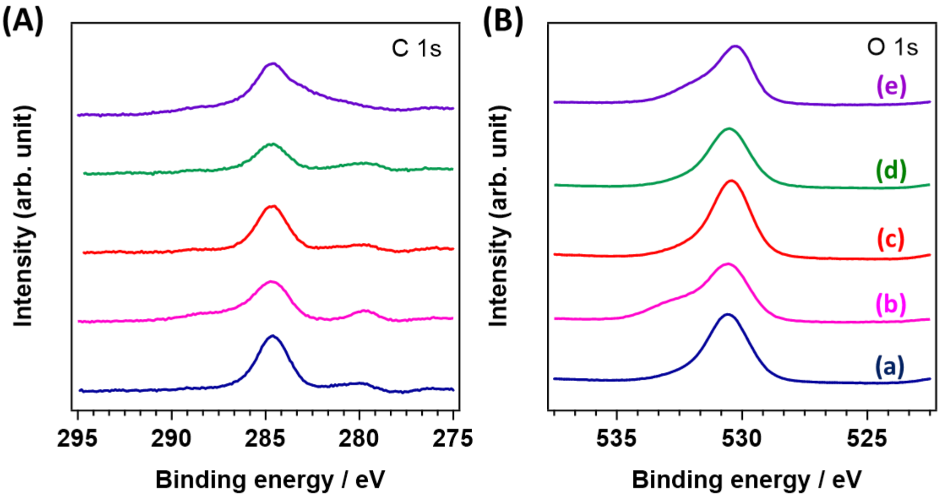

Figure 8. XPS spectra of (A) C 1s and (B) O 1s for (a)$ZnTa_2O_6$, (b) $10Zn/ZnTa_2O_6$ without calcination; (c) $10Zn/ZnTa_2O_6$, (d) $Zn_3Ta_2O_8$, and (e) ZnO

Table 1. The ratio of Zn to Ta detected by EDS and XPS

	Zn/Ta in theory	Zn/Ta by EDS	Zn/Ta by XPS	BET / m^2g^{-1}
$ZnTa_2O_6$	0.50	0.50	0.63	2.5
$10Zn/ZnTa_2O_6$	0.55	0.57	1.24	2.2
$3.0Ag/10Zn/ZnTa_2O_6$	0.55	0.57	1.01	/
$Zn_3Ta_2O_8$	1.50	1.54	2.61	/

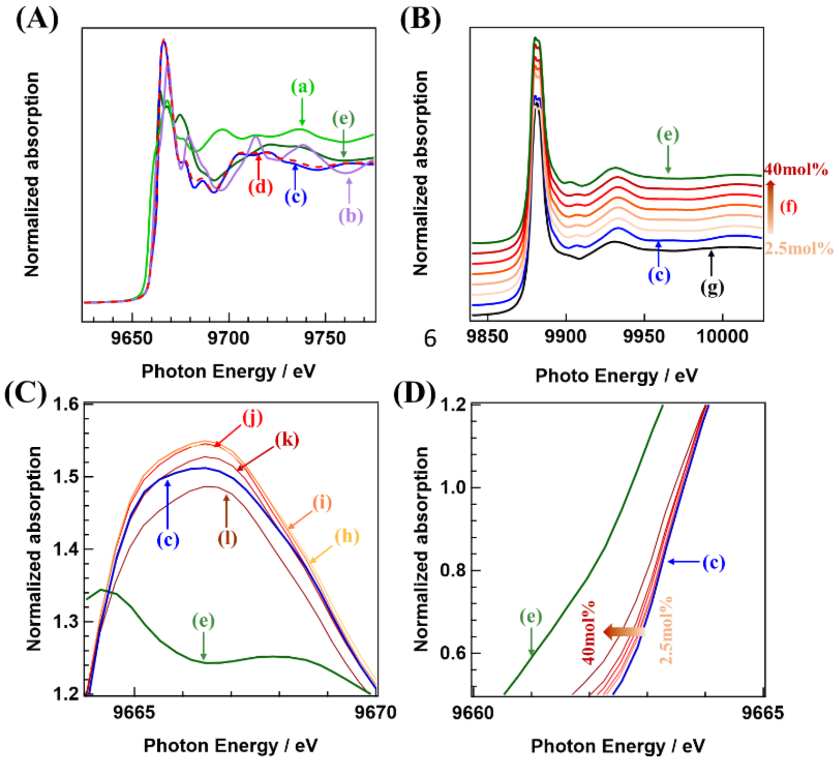

Figure 9. (A) Zn K−edge XANES spectra; (B) Ta L_{III}−edge XANES spectra; and (C, D) enlarged areas of the Zn K−edge XANES spectra of (a) Zn foil, (b) ZnO, (c) $ZnTa_2O_6$, (d) 10 mol% $Zn/ZnTa_2O_6$, (e) $Zn_3Ta_2O_8$, (f) $ZnTa_2O_6$ modified with different amounts of Zn, (g) Ta_2O_5, (h) $2.5Zn/ZnTa_2O_6$, (i) $5Zn/ZnTa_2O_6$, (j) $10Zn/ZnTa_2O_6$, (k) $20Zn/ZnTa_2O_6$, and (l) $40Zn/ZnTa_2O_6$.

Figure 10 shows the influence of the Ag cocatalyst loading method on the photocatalytic CO_2 conversion performance of $1.5Ag/10Zn/ZnTa_2O_6$. The catalyst fabricated by the CR and PD methods exhibited similar initial CO formation rates (16.9 μmol h^{-1}) and CO evolution selectivities (83.0–86.0%). In contrast, the initial CO formation rate and CO evolution selectivity of the catalyst prepared by the IMP method were 20.0 μmol h^{-1} and approximately 90%, respectively. The SEM images of the differently fabricated $1.5Ag/10Zn/ZnTa_2O_6$, shown in Figures 11 and 12, reveal that the Ag nanoparticles obtained by the CR and PD methods were large, whereas those resulting from IMP were small and well-dispersed on the $ZnTa_2O_6$ surface, as confirmed by the corresponding EDS mapping (Figure 12(c)). Moreover, several nanoparticles (40–80 nm) appeared on the surface of $10Zn/ZnTa_2O_6$ upon photoirradiation for 5 h (Figures 11(a,d)). In addition, Figures 11(e,f) show a slight increase in the size of the Ag nanoparticles prepared by the CR and PD methods after 5 h of photocatalytic reaction. Importantly, the Ag nanoparticles, which act as cocatalysts, were aggregated on the surface of the $ZnTa_2O_6$, and did not interfere with the $ZnTa_2O_6$ structure.

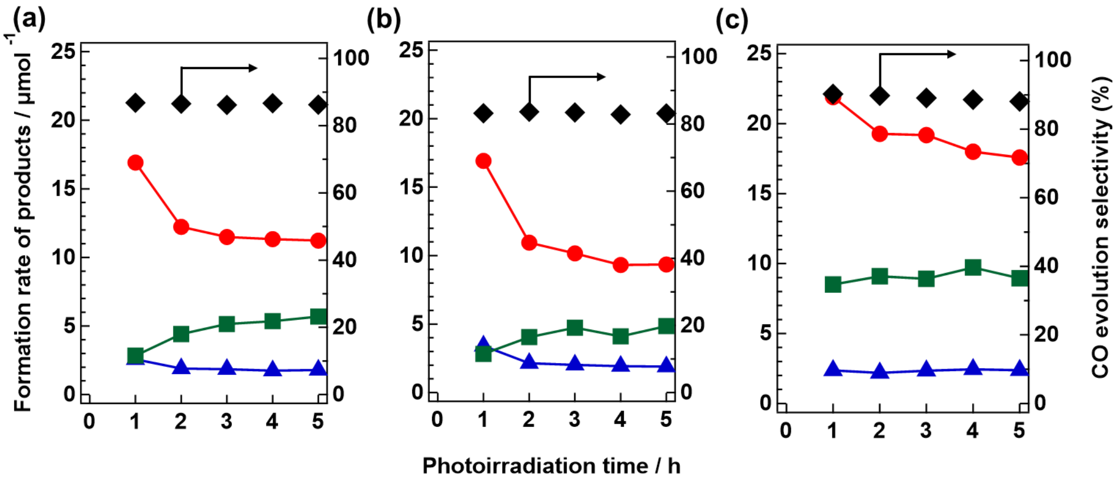

Figure 10. Formation rates of H_2 (green ▲), O_2 (blue ■), and CO (red ●) and CO evolution selectivities (black ♦) of $1.5Ag/10Zn/ZnTa_2O_6$ catalysts prepared by the (a) CR, (b) PD, and (c) IMP methods.

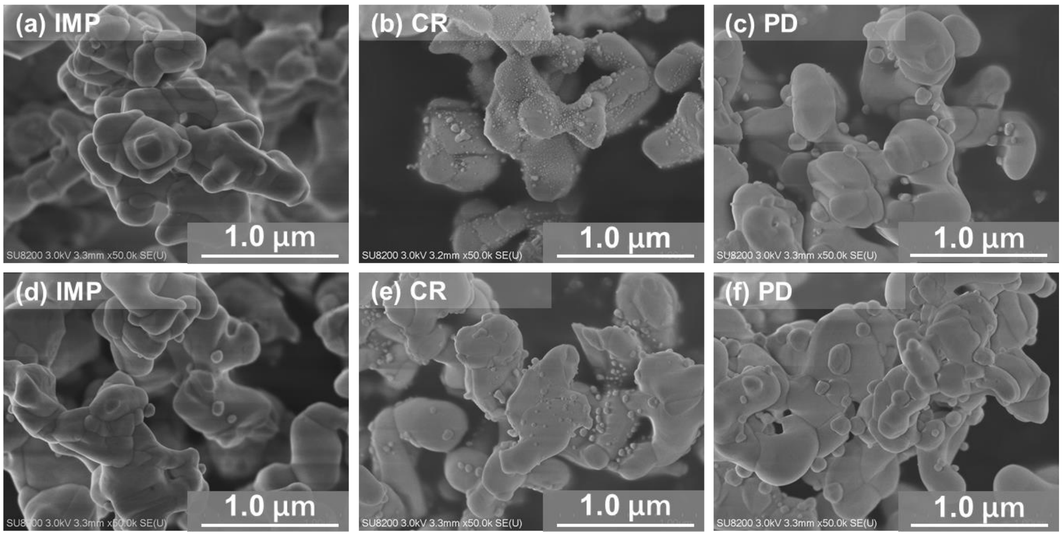

Figure 11. SEM images of (a), (d) $1.5Ag/10Zn/ZnTa_2O_6$ (IMP method); (b), (e) $1.5Ag/10Zn/ZnTa_2O_6$ (CR method); and (c), (f) $1.5Ag/10Zn/ZnTa_2O_6$ (PD method). (a–c) before reaction, and (d–f) after reaction.

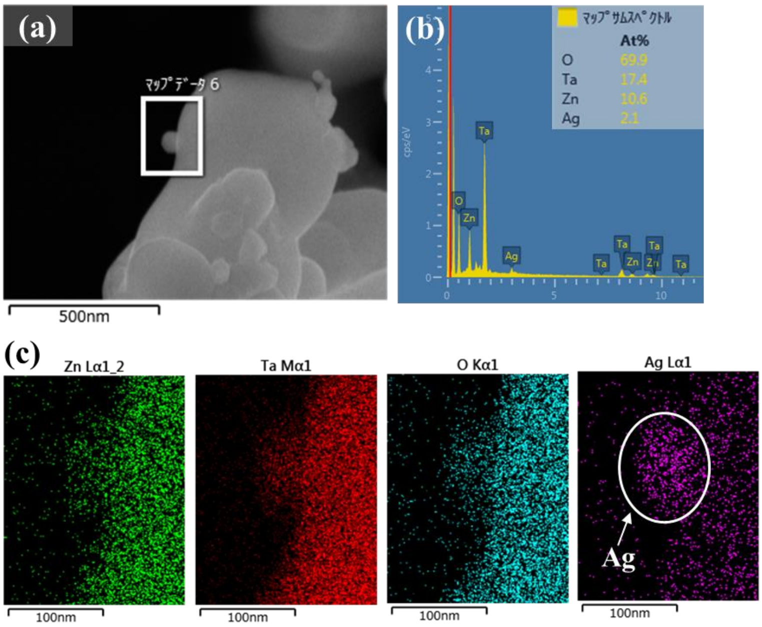

Figure 12. (a) 3.0Ag/10Zn/$ZnTa_2O_6$: Zn prepared by IMP method, after reaction; (b) EDS mapping of the Ag-loaded$ZnTa_2O_6$: Zn after photocatalytic reactions; (c) EDS mapping of the Zn, Ta, O, and Ag element

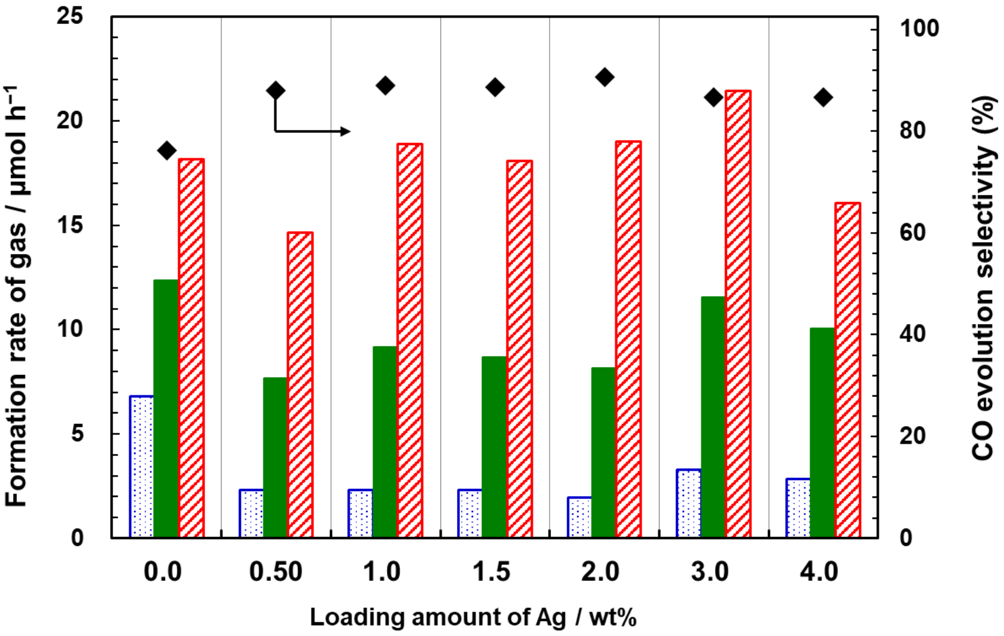

Figure 13. Formation of the photocatalytic products H_2 (blue dotted), O_2 (green filled), and CO (red slashed) and CO evolution selectivities (black ♦) over 10Zn/$ZnTa_2O_6$ catalysts with 0.0, 0.5, 1.0, 2.0, 3.0, and 4.0 wt% Ag loading.

Figure 13 shows the dependence of the product formation rates on the Ag cocatalyst loading. The CO evolution selectivity of the 10Zn/$ZnTa_2O_6$ catalyst (without Ag) was relatively high (71.8%). The loading of minute Ag amounts (0.50 wt%) suppressed the H_2 evolution and boosted the CO evolution selectivity to 88%. While the CO formation rate initially increased with the increase in the amount of Ag, it stalled in the range of 1.0–3.0 wt% and slightly decreased for loadings above 4.0 wt%. Further, the increase in the Ag loading was accompanied by an increase in the size of the Ag particles (Figure 14). As the Ag cocatalyst effects the photocatalytic conversion of CO_2 by H_2O, the CO formation rate increased over the range of 0.0–1.0 wt% Ag cocatalyst. However, the increase in the amount of Ag cocatalyst negatively impacted the photocatalytic performance of the material, as the excess amount of Ag aggregated on the surface of the photocatalyst (Figure 14).

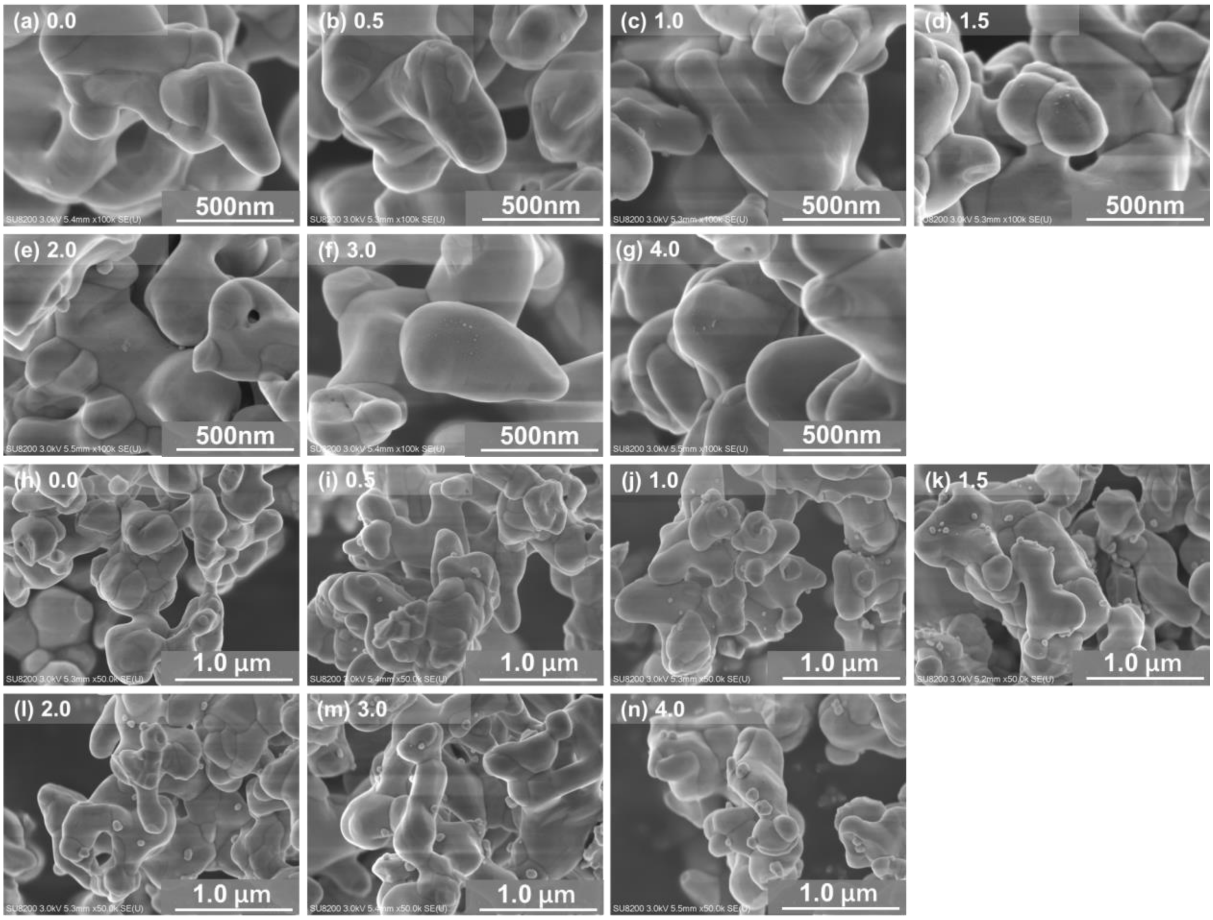

Figure 14. SEM image of the 10Zn/$ZnTa_2O_6$ loaded with various amount of Ag cocatalyst (a-g) before rection; (h-n) After 5-h photocatalytic reaction. (a) and (h) 0.0Ag; (b) and (i) 0.5Ag; (c) and (j) 1.0Ag; (d) and (k) 1.5Ag; (e) and (l) 2.0Ag; (f) and (m) 3.0Ag; (g) and (n) 4.0Ag.

The photocatalytic conversion of CO_2 by H_2O over 3.0Ag/10Zn/$ZnTa_2O_6$ was further investigated by control experiments (Figure 15). Minute H_2 and O_2 amounts were detected in the absence of the photocatalyst or photoirradiation, highlighting their importance to the photocatalytic activity. The absence of the buffer ($NaHCO_3$) or the use of Ar gas instead of CO_2 led to preferential formation of H_2 over 3.0Ag/10Zn/$ZnTa_2O_6$. When the reaction was conducted under Ar gas flow (instead of CO_2), the observed CO evolution stemmed from $NaHCO_3$ (Figure 15d). Moreover, the role of CO_2 gas as the carbon source of CO generated under the typical reaction conditions was confirmed by the isotopic experiment.[19-20, 28]

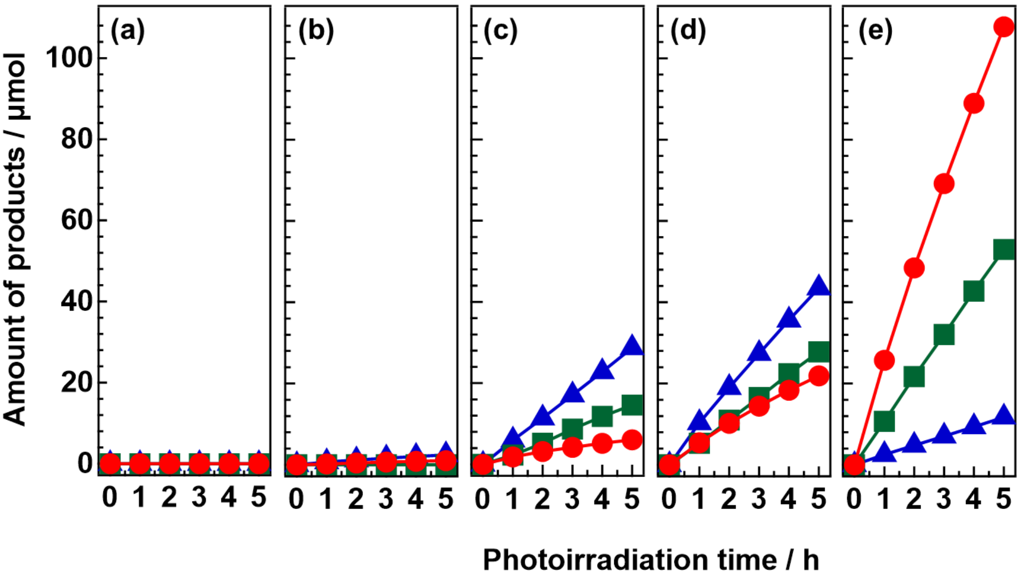

Figure 15. Control experiments on the 3.0Ag/10Zn/$ZnTa_2O_6$-catalyzed formation of H_2 (blue ▲), O_2 (green ■), and CO (red ●) over time. Deviation from the typical conditions: (a) in the dark; (b) without photocatalyst; (c) without $NaHCO_3$; (d) with Ar instead of CO_2 gas; (e) none.

In addition to the catalyst's activity, its durability is among the most important factors in the evaluation of the photocatalyst's properties. Figure 16 shows the H_2, O_2, and CO formation rates during the 3.0Ag/10Zn/$ZnTa_2O_6$-catalyzed conversion of CO_2 by H_2O over 15 h. After every 5 h, the photoirradiation was interrupted for 15 h while maintaining the flow of CO_2. While the CO formation rate decreased much more rapidly during the first run than during the second one (1–5 h and 6–10 h photoirradiation time, respectively), it remained stable during the third run (11–15 h photoirradiation time). The XRD patterns and the SEM images of 3.0Ag/10Zn/$ZnTa_2O_6$ were recorded before and after the experiment (Figures 17 and 18). While the XRD patterns remained practically unchanged, indicating that the crystalline structure was preserved during the reaction, a significant increase in the Ag nanoparticle size was revealed by the SEM images. Thus, the author concluded that Ag nanoparticle aggregation occurred during the photocatalytic reaction.

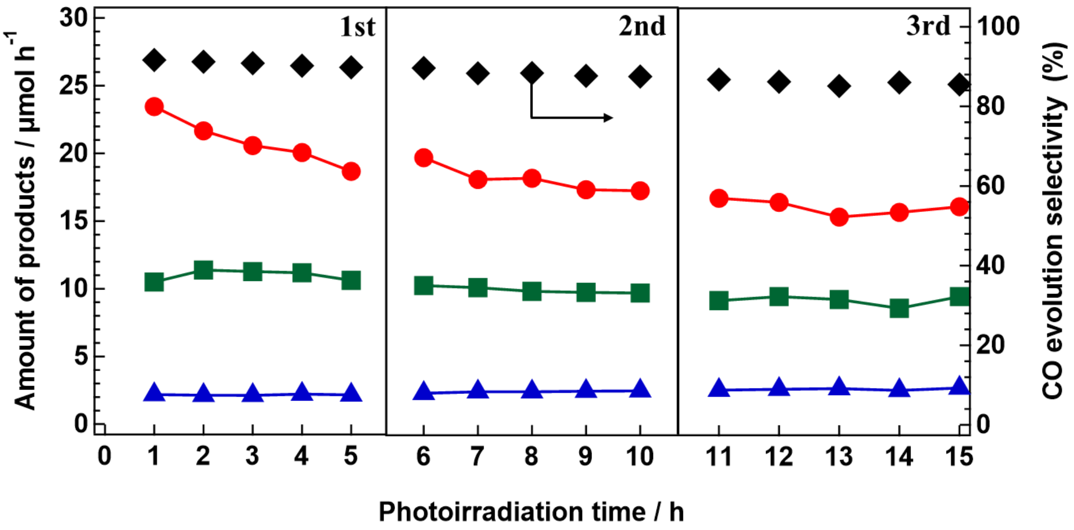

Figure 16. Time-dependent evolution of H_2 (blue ▲), O_2 (green ■), and CO (red ●) and CO evolution selectivities (black ♦) over 3.0Ag/10Zn/$ZnTa_2O_6$ over 15 h with photoirradiation interruption every 5h.

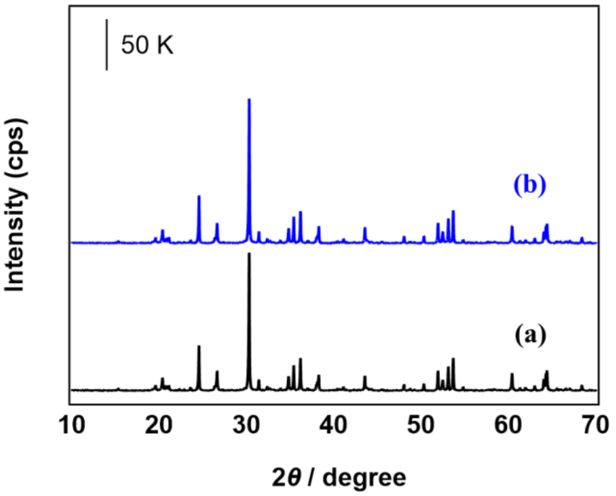

Figure 17. XRD patterns of 3.0Ag/10Zn/$ZnTa_2O_6$ (a) before and (b) after 15 h photocatalytic reaction.

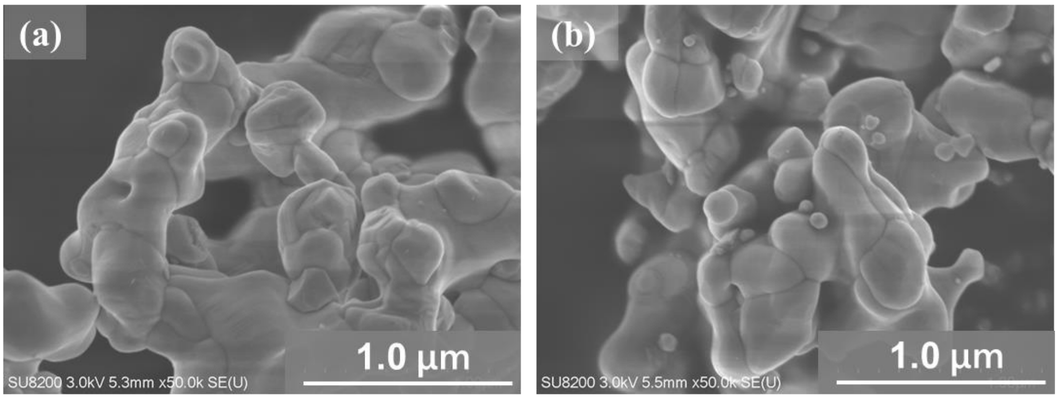

Figure 18. SEM images of $3.0Ag/10Zn/ZnTa_2O_6$ (a) before and (b) after 15 h photocatalytic reaction.

To confirm the effect of the Zn modification on the activity of $ZnTa_2O_6$ photocatalysts during the reduction of CO_2 to CO in an aqueous solution, the water splitting activity of the $ZnTa_2O_6$, $10Zn/ZnTa_2O_6$, $3.0Ag/ZnTa_2O_6$, and $3.0Ag/10Zn/ZnTa_2O_6$ photocatalysts was evaluated in deionized water and under a flow of Ar gas. Stoichiometric amounts of H_2 and O_2 were generated over all photocatalysts (Figure 19(A)). The highest H_2 and O_2 formation rates were observed over the bare $ZnTa_2O_6$, whereas $3.0Ag/10Zn/ZnTa_2O_6$ exhibited the poorest overall water splitting activity. In addition, the water splitting photocatalytic performance of $Ag/ZnTa_2O_6$ and $10Zn/ZnTa_2O_6$ were lower than that of $ZnTa_2O_6$. Moreover, Figure 19(B) allows a direct comparison of the photocatalytic CO_2 reduction performance of $ZnTa_2O_6$, $10Zn/ZnTa_2O_6$, $3.0Ag/ZnTa_2O_6$, and $3.0Ag/10Zn/ZnTa_2O_6$. Furthermore, additives play an important role in the photocatalytic water splitting[45] and CO_2 reduction reactions.[46] The overall catalyst activities were significantly higher when the reaction was conducted in aqueous 0.1 M $NaHCO_3$ and under CO_2 gas bubbling (Figure 19). In the field of CO_2 photoreduction, the low CO evolution selectivity of bare photocatalysts is generally improved by Ag loading. For example, H_2 was mainly formed over $ZnTa_2O_6$, which exhibited a CO evolution selectivity and CO formation rate of 22.9% and 8.9 µmol h^{-1}, respectively (Figure 19(B)(a)). In comparison, these values were significantly higher for $Zn/ZnTa_2O_6$ (71.8%, 19.2 µmol h^{-1}) and $Ag/ZnTa_2O_6$ (63.9%, 25.6 µmol h^{-1}), whereas the H_2 evolution decreased markedly (Figure 19(B)(b-c)). Hence, catalyst modification by Zn and use of Ag as a cocatalyst not only suppress the production of H_2 from H_2O, which competes with the reduction of CO_2 to CO, but also improve the

CO formation rate. Moreover, the H_2 formation rate of 3.0Ag/10Zn/$ZnTa_2O_6$, which contains both Zn species and Ag cocatalyst, was further decreased. As a result, the highest CO formation rate and CO evolution selectivity were achieved. Interestingly, H_2 generation over the 10Zn/$ZnTa_2O_6$, 3.0Ag/$ZnTa_2O_6$, and 3.0Ag/10Zn/$ZnTa_2O_6$ photocatalysts during the photocatalytic conversion of CO_2 (typical conditions, Figure 19(B)(b–d)) was nearly the same as under the water splitting conditions (Figure 19(A)(b–d)). Hence, the author postulates that the reduction of CO_2 to CO and the production of H_2 occur at distinct active sites on the $ZnTa_2O_6$ surface. In contrast, while the CO formation rates of 3.0Ag/10Zn/$ZnTa_2O_6$ and 10Ag/$ZnTa_2O_6$ were similar, the H_2 formation rate of the former was lower (Figure 19(B)(c-d)). Therefore, CO evolution presumably occurs on the surface of the Ag cocatalyst (active sites of CO generation), whereas the Zn species simply suppresses the formation of H_2 in Ag-containing $ZnTa_2O_6$-based photocatalysts by blocking the active sites in which H_2 evolution occurs. Thus, the overall water splitting activity was suppressed and the CO evolution selectivity of the photocatalytic conversion of CO_2 using H_2O as electron donor was enhanced. Furthermore, the Zn species might be a potential cocatalyst candidate to further improve the CO_2 reduction performance.

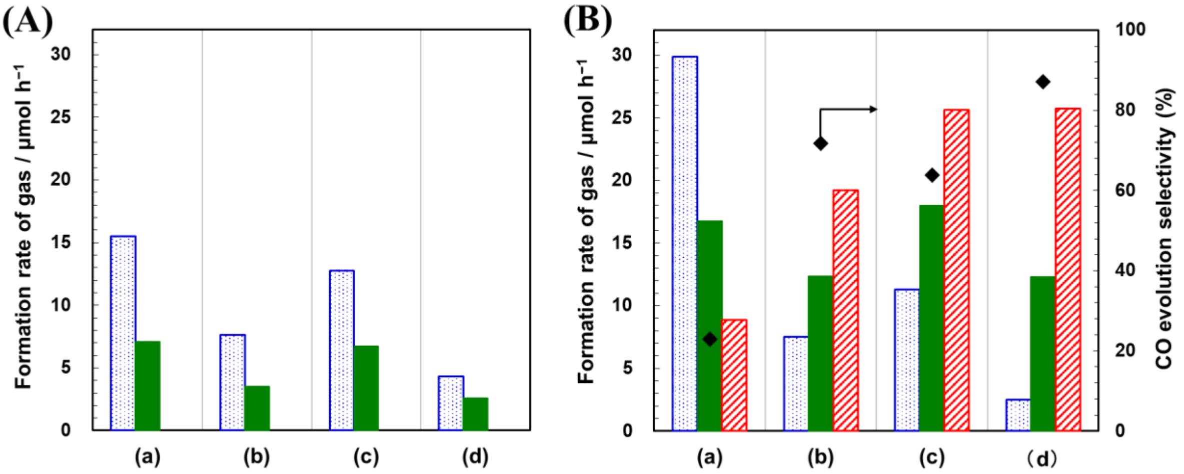

Figure 19. (A) Photocatalytic water splitting (deviations from the typical conditions: H_2O instead of 0.1 M aqueous $NaHCO_3$; Ar gas instead of CO_2) and (B) CO_2 reduction performance of the photocatalysts (a) $ZnTa_2O_6$, (b) 10Zn/$ZnTa_2O_6$, (c) 3.0Ag/$ZnTa_2O_6$, and (d) 3.0Ag/10Zn/$ZnTa_2O_6$ under typical conditions. The formation rates of H_2, O_2, and CO are indicated in blue dotted, green filled, and red slashed columns, respectively. The CO evolution selectivities are indicated by black ♦.

Schematic depictions of the potential Zn/$ZnTa_2O_6$-based photocatalyst structures and of a plausible reaction mechanism for the Ag/Zn/$ZnTa_2O_6$-photocatalyzed conversion of CO_2 using H_2O as an electron donor are displayed in Scheme 1. Two Zn/$ZnTa_2O_6$ potential structures are proposed based on the experimental data. The first one features modification by Zn species exclusively on the $ZnTa_2O_6$ surface (Scheme 1(a)). This is in accordance with the lack of changes in the XRD and XANES data upon Zn modification (see Figures 2 and 9), which suggests that the $ZnTa_2O_6$ crystal structure remained intact and that Zn modification led to formation of a thin amorphous ZnO or crystalline $Zn_3Ta_2O_8$ layer on the $ZnTa_2O_6$ surface. In contrast, the second proposed structure features Zn atoms interstitially doped in the bulk of $ZnTa_2O_6$ with a possible Zn concentration gradient (Scheme 1(b)). This model is in agreement with the shift of the XPS Ta 4f and O 1s peaks to lower binding energies upon Zn modification (see Figure 7), as such shifts are generally regarded as relaxations and reflect changes in the final system state during the measurement.[41, 47] Hence, they possibly indicate changes in the electronic structure resulting from Zn incorporation. In addition, the slight shift of the adsorption edge in the Zn K−edge XANES spectra of Zn/$ZnTa_2O_6$ to lower energy values when the amount of modified Zn increased from 2.5 to 40% suggested that the Zn modification affected the local structure of Zn (Figure 9),[43-44] in similar fashion as described for the $SrFe_{1-x}Zn_xO_{3-\delta}$ system.[43] Furthermore, Grosvenor and Gaultois suggested that XANES adsorption energy edge shifts are related to changes in the coordination number.[43] Hence, the gradual decrease in the adsorption energy edge of the Zn K-edge XANES of Zn/$ZnTa_2O_6$, which correlates with the increase in the amount of Zn modification, is due to a decrease in the Zn coordination number, suggesting the partial incorporation of Zn species into the $ZnTa_2O_6$ crystal structure. In this case, the $ZnTa_2O_6$ and Zn species function as the solvent and solute, respectively, and the system can be regarded as an interstitial solid solution.[48]

Further, on the basis of the experimental data presented and discussed herein, a model for the proposed distinct active reaction sites for CO evolution (CO_2 reduction) and H_2 evolution (water splitting) is displayed in Scheme 1(c). Upon Zn modification, the H_2 formation rate significantly decreased because the active H_2 evolution sites were blocked, whereas the active CO_2 reduction sites remained largely accessible (Scheme 1(d)). Hence, in addition to the previously reported activity of Ag in the selective photocatalytic conversion of CO_2 in an aqueous solution,[12] the experimental data obtained in this study demonstrate that the presence of Ag as a cocatalyst also leads to a significant decrease in the H_2 evolution. Finally, the experimental evidence suggests that the Zn species also function as CO_2 reduction cocatalysts, albeit with a lower activity than the Ag cocatalyst.

Scheme 1. (a) Zn modification exclusively on the surface of $ZnTa_2O_6$, (b) additional Zn incorporation into $ZnTa_2O_6$, putative mechanism of the photocatalytic reaction over (c) $ZnTa_2O_6$ and (d) $3.0Ag/10Zn/ZnTa_2O_6$.

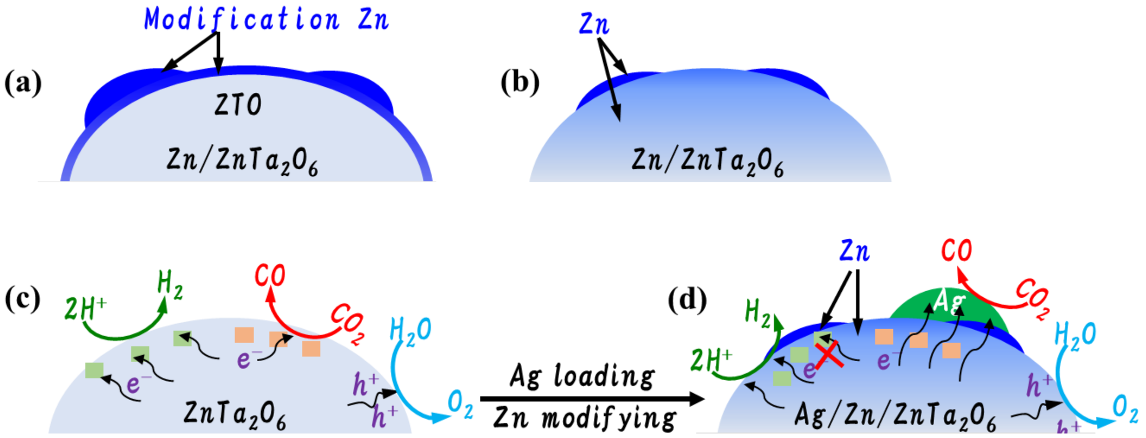

[a] The active sites for H_2 and CO evolution are indicated by light green and apricot squares, respectively. The Zn modifications and Ag cocatalyst are indicated in blue and green, respectively.

Conclusion

The modification of the $ZnTa_2O_6$ surface by Zn species significantly improved the CO evolution selectivity in the photocatalytic conversion of CO_2 using H_2O as an electron donor. In the case of low Zn concentration, the modification consists of a thin layer of amorphous ZnO or incorporation of Zn atoms as interstitial dopant into the bulk of the $ZnTa_2O_6$ photocatalyst. The author speculated that the surface of $ZnTa_2O_6$ features separate active sites for H_2 and CO evolution. In addition, the modified Zn species introduced on the surface of $Zn/ZnTa_2O_6$ influence the H_2 evolution sites. In the modified catalysts, the Zn species suppresses the evolution of H_2, enhancing the CO evolution selectivity, and as well contributes to the CO formation. Therefore, the Zn species is likely a novel cocatalyst, in addition to the previously known Ag nanoparticle-based cocatalysts. A reasonable structure model and the role of the modified Zn should be addressed in future studies.

Reference

1. N. N. Vu; S. Kaliaguine; T. O. Do, *Adv. Funct. Mater.* **2019**, 29 (31), 1901825.
2. M. Halmann, *Nature* **1978**, 275 (5676), 115-116.
3. T. Inoue; A. Fujishima; S. Konishi; K. Honda, *Nature* **1979**, 277 (5698), 637-638.
4. T. Zhang; W. Lin, *Chem. Soc. Rev.* **2014**, 43 (16), 5982-5993.
5. J. L. White; M. F. Baruch; J. E. Pander III; Y. Hu; I. C. Fortmeyer; J. E. Park; T. Zhang; K. Liao; J. Gu; Y. Yan, *Chem. Rev.* **2015**, 115, 12888-12935.
6. L. Tan; S. M. Xu; Z. Wang; Y. Xu; X. Wang; X. Hao; S. Bai; C. Ning; Y. Wang; W. Zhang, *Angewandte Chemie* **2019**, 131 (34), 11986-11993.
7. J. Yang; D. Wang; H. Han; C. Li, *Acc. Chem. Res.* **2013**, 46 (8), 1900-1909.
8. S. N. Habisreutinger; L. Schmidt-Mende; J. K. Stolarczyk, *Angew. Chem. Int. Ed.* **2013**, 52, 7372-7408.
9. K. Teramura; T. Tanaka, *Phys. Chem. Chem. Phys.* **2018**, 20 (13), 8423-8431.
10. L. Tan; Z. Wang; Y. Zhao; Y.-F. Song, *Chemistry–An Asian Journal* **2020**.
11. K. Ikeue; H. Yamashita; M. Anpo; T. Takewaki, *J. Phys. Chem. B* **2001**, 105 (35), 8350-8355.
12. K. Iizuka; T. Wato; Y. Miseki; K. Saito; A. Kudo, *J. Am. Chem. Soc.* **2011**, 133 (51), 20863-20868.
13. H. Yoshida; L. Zhang; M. Sato; T. Morikawa; T. Kajino; T. Sekito; S. Matsumoto; H. Hirata, *Catal. Today* **2015**, 251, 132-139.
14. Z. Wang; K. Teramura; Z. Huang; S. Hosokawa; Y. Sakata; T. Tanaka, *Catal. Sci. & Technol* **2016**, 6, 1025-1032.
15. Z. Huang; K. Teramura; H. Asakura; S. Hosokawa; T. Tanaka, *Catal. Today* **2018**, 300, 173-182.
16. R. Pang; K. Teramura; H. Tatsumi; H. Asakura; S. Hosokawa; T. Tanaka, *Chem. Commun.* **2018**, 54 (9), 1053-1056.

17. P. S. Surdhar; S. P. Mezyk; D. A. Armstrong, *J. Phys. Chem.* **1989**, 93 (8), 3360-3363.

18. J. Qiao; Y. Liu; F. Hong; J. Zhang, *Chem. Soc. Rev.* **2014**, 43 (2), 631-675.

19. S. Iguchi; K. Teramura; S. Hosokawa; T. Tanaka, *Catal. Sci. Technol.* **2016**, 6 (13), 4978-4985.

20. Z. Wang; K. Teramura; S. Hosokawa; T. Tanaka, *Appl. Catal. B* **2015**, 163, 241-247.

21. K. Teramura; H. Tatsumi; Z. Wang; S. Hosokawa; T. Tanaka, *Bull. Chem. Soc. Jpn.* **2015**, 88, 431-437.

22. Z. Wang; K. Teramura; S. Hosokawa; T. Tanaka, *J. Mater. Chem. A* **2015**, 3, 11313-11319.

23. R. Pang; K. Teramura; H. Asakura; S. Hosokawa; T. Tanaka, *Appl. Catal. B* **2017**, 218, 770-778.

24. A. Anzai; N. Fukuo; A. Yamamoto; H. Yoshida, *Catal. Commun.* **2017**, 100, 134-138.

25. H. Nakanishi; K. Iizuka; T. Takayama; A. Iwase; A. Kudo, *ChemSusChem* **2017**, 10 (1), 112-118.

26. S. Kikkawa; K. Teramura; H. Asakura; S. Hosokawa; T. Tanaka, *J. Phys. Chem. C* **2018**, 122, 21132-21139.

27. X. Zhu; A. Yamamoto; S. Imai; A. Tanaka; H. Kominami; H. Yoshida, *Chem. Commun.* **2019**, 13514-13517.

28. S. Wang; K. Teramura; T. Hisatomi; K. Domen; H. Asakura; S. Hosokawa; T. Tanaka, *ACS Appl. Energy Mater.* **2020**, 3, 1468-1475.

29. S. Yan; J. Wang; H. Gao; N. Wang; H. Yu; Z. Li; Y. Zhou; Z. Zou, *Adv. Funct. Mater.* **2013**, 23 (14), 1839-1845.

30. S. C. Yan; S. X. Ouyang; J. Gao; M. Yang; J. Y. Feng; X. X. Fan; L. J. Wan; Z. S. Li; J. H. Ye; Y. Zhou, *Angew. Chem. Int. Ed.* **2010**, 49 (36), 6400-6404.

31. Q. Liu; Y. Zhou; J. Kou; X. Chen; Z. Tian; J. Gao; S. Yan; Z. Zou, *J. Am. Chem. Soc.* **2010**, 132 (41), 14385-14387.

32. H. Jiang; K.-i. Katsumata; J. Hong; A. Yamaguchi; K. Nakata; C. Terashima; N. Matsushita; M. Miyauchi; A. Fujishima, *Appl. Catal. B* **2018**, 224, 783-790.

33. K. Teramura; Z. Wang; S. Hosokawa; Y. Sakata; T. Tanaka, *Chem. Eur. J.* **2014**, 20 (32), 9906-9909.

34. Z. Ding; W. Wu; S. Liang; H. Zheng; L. Wu, *Mater. Lett.* **2011**, 65 (11), 1598-1600.

35. B. R. D. Shannon, *Acta Cryst* **1976**, A32, 751-767.

36. K.-C. Lee; S.-J. Lin; C.-H. Lin; C.-S. Tsai; Y.-J. Lu, *Surf. Coat.Technol.* **2008**, 202 (22-23), 5339-5342.

37. K.-H. Chen; Y.-C. Pu; K.-D. Chang; Y.-F. Liang; C.-M. Liu; J.-W. Yeh; H.-C. Shih; Y.-J. Hsu, *J. Phys. Chem. C.* **2012**, 116 (35), 19039-19045.

38. J.-P. Lee; D. Chen; X. Li; S. Yoo; L. A. Bottomley; M. A. El-Sayed; S. Park; M. Liu, *Nanoscale* **2013**, 5 (23), 11620-11624.

39. Y. Su; B. Zhu; K. Guan; S. Gao; L. Lv; C. Du; L. Peng; L. Hou; X. Wang, *J. Phys. Chem. C* **2012**, 116 (34), 18508-18517.

40. M. C. Biesinger; L. W. Lau; A. R. Gerson; R. S. C. Smart, *Phys. Chem. Chem. Phys.* **2012**, 14 (7), 2434-2442.

41. T. L. Barr, *Journal of Vacuum Science & Technology A: Vacuum, Surfaces, and Films* **1991**, 9 (3), 1793-1805.

42. D. Mandrino; M. Godec; M. Torkar; M. Jenko, *Surface and Interface Analysis: An International Journal devoted to the development and application of techniques for the analysis of surfaces, interfaces and thin films* **2008**, 40 (3-4), 285-289.

43. M. W. Gaultois; A. P. Grosvenor, *J. Phy. Chem. C* **2010**, 114 (46), 19822-19829.

44. A. Sharma; M. Varshney; H. J. Shin; B.-H. Lee; K. H. Chae; S. O. Won, *Mater. Chem. Phys.* **2017**, 191, 129-144.

45. K. Sayama; K. Yase; H. Arakawa; K. Asakura; A. Tanaka; K. Domen; T. Onishi, *J. Photochem. Photobiol. A* **1998**, 114 (2), 125-135.

46. R. Pang; K. Teramura; H. Asakura; S. Hosokawa; T. Tanaka, *ACS Appl. Energy Mater.* **2019**, 2 (8), 5397-5405.

47. K. Kim; S. W. Gaarenstroom; N. Winograd, *Chem. Phys. Lett.* **1976**, 41 (3), 503-506.

48. I. Voznyak; Y. Tokaychuk; V. Hlukhyy; T. Fässler; R. Gladyshevskii, *J. Alloys Compd.* **2012**, 512 (1), 246-251.

Summary

In this thesis, the photocatalytically conversion of CO_2 and H_2O into (hydro)carbons and O_2 over a heterogenous photocatalyst in a quasi-flow batch system with an internal-irradiation-type reaction vessel at 298 K under 101.3 kPa was studied. Surface modification, cation doping, and dual cocatalysts played important roles in fabricating highly efficient and selective heterogenous photocatalysts for the photoreduction of CO_2 to CO. The general conclusions of the thesis are as follows.

Chapter 1. Well-shaped Al-$SrTiO_3$ was fabricated using a facile flux method. The photocatalytic activity of CO_2 over the fabricated Al-$SrTiO_3$ catalyst depended on the Al doping content, which was affected by the calcination conditions (e.g., calcination temperature and time). Ag/Al-$SrTiO_3$, which was fabricated at 1423 K for 15 h, exhibited high catalytic activity and CO evolution selectivity during the photocatalytic conversion of CO_2 using H_2O as the electron donor under photoirradiation at $\lambda \geq 300$ nm. Compared with impregnation (IMP) and photodeposition (PD), CR loading resulted in a Ag-loaded catalyst with an excellent CO formation rate and high CO evolution selectivity (98.8%). Furthermore, the Ag cocatalyst particle size and dispersion and chemical state of Ag affected the activity of the Ag/Al-$SrTiO_3$ photocatalyst.

Chapter 2. Al doping into perovskite-structured $SrTiO_3$ catalyst enhanced CO_2 photoreduction. In addition, except for small quantities of Al_2O_3 on the $SrTiO_3$ surface, most Al was doped on the layered edges of the perovskite structure. After doping, numerous stepwise edge structures were observed on the surface of the Al-doped $SrTiO_3$ photocatalyst. These results are important as the development of novel catalysts for the photoreduction of CO_2, which is the primary GHG, is critical. Isotope-labeling experiments using $^{13}CO_2$ indicated that the CO evolved over the Ag/Al-$SrTiO_3$ catalyst was derived from the CO_2 bubbled into an aqueous solution of $NaHCO_3$ and not from the residual carbon species on the catalyst surface.

Chapter 3. Loading Ag and Co onto Al-$SrTiO_3$ significantly improved its activity for the photocatalytic conversion of CO_2 using H_2O as the electron donor. Ag and Co facilitated CO_2 reduction and H_2O oxidation, respectively, on the Al-$SrTiO_3$ surface, and the AgCo/Al-$SrTiO_3$ catalyst presented an extremely high CO evolution selectivity (99.8%). Furthermore, the CO evolution apparent quantum efficiency over AgCo/Al-$SrTiO_3$ was approximately 0.03% when the reaction system was photoirradiated at $\lambda = 365$ nm, and the CO evolution selectivity was 98.6% (7.4 μmol h^{-1}). In addition, it was revealed that the reduction (Ag cocatalyst) and oxidation (Co cocatalyst) sites were distributed on the {100} and {110} facets of Al-$SrTiO_3$, respectively, and promoted CO and O_2 formation, respectively. The synergism between the Ag and Co dual cocatalysts effectively enhanced the photocatalytic conversion of CO_2 over the Al-$SrTiO_3$ catalyst using H_2O as the electron donor.

Chapter 4. Various Ag–M (M = Fe, Co, Ni, and Pt) dual cocatalysts were deposited on the surface of Al-$SrTiO_3$ using a PD method. Ag–Fe dual cocatalyst modification of the Al-$SrTiO_3$ photocatalyst surface significantly increased CO formation rate and presented high selectivity toward CO evolution during the photocatalytic conversion of CO_2 using H_2O as the electron donor under light illumination at $\lambda \geq 300$ nm. The Ag and Fe cocatalysts served as CO_2 reduction and H_2O oxidization promotors, respectively.

Chapter 5. The modification of the $ZnTa_2O_6$ surface using Zn species significantly improved CO evolution selectivity during the photocatalytic conversion of CO_2 using H_2O as the electron donor. At a low Zn concentration, the modification consisted of a thin layer of amorphous ZnO or incorporation of Zn atoms as interstitial dopants into the bulk of the $ZnTa_2O_6$ photocatalyst. The active sites for H_2 and CO evolution on the surface of $ZnTa_2O_6$ were speculated to be distinct. In addition, the modified Zn species introduced on the surface of Zn/$ZnTa_2O_6$ affected the H_2 evolution sites. For the modified catalysts, the Zn species suppressed H_2 evolution, increased CO evolution selectivity, and boosted CO formation. Therefore, the Zn species were likely a novel cocatalyst in addition to the previously reported Ag nanoparticle-based cocatalysts.

In summary, crystal facet exposure, photocatalyst surface composition, and cocatalyst loading were extremely important factors that affected photocatalyst activity for CO_2 reduction. The Al-doped $SrTiO_3$ (Chapters 1 and 2) and Zn species-modified $ZnTa_2O_6$ photocatalysts (Chapter 5) presented good photocatalytic activity and CO evolution selectivity for CO_2 reduction using H_2O as the electron donor. In addition, the dual cocatalysts (e.g., Ag-Co and Ag-Fe) on the Al-$SrTiO_3$ surface (Chapters 3 and 4) significantly increased CO formation rate and conferred the catalysts extremely high CO evolution selectivity. These results are expected to contribute to the development and application of the photocatalytic conversion of CO_2 and H_2O into (hydro)carbons and O_2 over heterogenous photocatalysts in the near future.

List of publications

Chapter 1

This is the peer reviewed version which has been published in final form at DOI: 10.1002/slct.202001693

1. Optimized Synthesis of Ag-Modified Al-Doped $SrTiO_3$ Photocatalyst for the Conversion of CO_2 Using H_2O as an Electron Donor

   Shuying Wang, Kentaro Teramura, Takashi Hisatomi, Kazunari Domen, Hiroyuki Asakura, Saburo Hosokawa, Tsunehiro Tanaka

   Chemistry Select **2020**, 5, 8779–8786

Chapter 2

This is the peer reviewed version which has been published in final form at DOI: 10.1021/acsaem.9b01927

2. Effective Driving of Ag-Loaded and Al-Doped $SrTiO_3$ under Irradiation at $\lambda > 300$ nm for the Photocatalytic Conversion of CO_2 by H_2O,

   Shuying Wang, Kentaro Teramura, Takashi Hisatomi, Kazunari Domen, Hiroyuki Asakura, Saburo Hosokawa, Tsunehiro Tanaka

   ACS Applied Energy Materials., **2020**, 3, 1468−1475

Chapter 3

This is the peer reviewed version which has been accepted in final form at DOI: 10.1039/D1SC00206F

3. Dual Ag/Co Cocatalyst Synergism for the Highly Effective Photocatalytic Conversion of CO_2 by H_2O over Al-$SrTiO_3$

   Shuying Wang, Kentaro Teramura, Takashi Hisatomi, Kazunari Domen, Hiroyuki Asakura, Saburo Hosokawa, Tsunehiro Tanaka

   Chemical Science, **2021,** accepted

Chapter 4

4. Highly Selective Photocatalytic Conversion of Carbon Dioxide by Water over Al-$SrTiO_3$ Photocatalyst Modified with Silver-Metal Dual Cocatalysts

   Shuying Wang, Kentaro Teramura, Takashi Hisatomi, Kazunari Domen, Hiroyuki Asakura, Saburo Hosokawa, Tsunehiro Tanaka

   ACS Sustainable Chemistry & Engineering, submitted

Chapter 5

This is the peer reviewed version which has been published in final form at DOI: 10.1021/acs.jpcc.0c08464

5. Effect of Zn in Ag-Loaded Zn-Modified $ZnTa_2O_6$ for Photocatalytic Conversion of CO_2 by H_2O,

   Shuying Wang, Kentaro Teramura, Hiroyuki Asakura, Saburo Hosokawa, and Tsunehiro Tanaka.

   Journal of Physical Chemistry C, **2021**, 125, 1304−1312